Article

Single-cell and spatial atlases of spinal cord injury in the *Tabulae Paralytica*

https://doi.org/10.1038/s41586-024-07504-y

Received: 23 June 2023

Accepted: 1 May 2024

Published online: 19 June 2024

Check for updates

Michael A. Skinnider[1,2,3,4,10], Matthieu Gautier[1,2,10], Alan Yue Yang Teo[1,2], Claudia Kathe[1,2], Thomas H. Hutson[1,2,5], Achilleas Laskaratos[1,2], Alexandra de Coucy[1,2], Nicola Regazzi[1,2], Viviana Aureli[1,2,6,7], Nicholas D. James[1,2], Bernard Schneider[1,8], Michael V. Sofroniew[9], Quentin Barraud[1,2], Jocelyne Bloch[1,2,6,7], Mark A. Anderson[1,2,5,7,11] ✉, Jordan W. Squair[1,2,6,11] ✉ & Grégoire Courtine[1,2,6,7,11] ✉

Here, we introduce the *Tabulae Paralytica*—a compilation of four atlases of spinal cord injury (SCI) comprising a single-nucleus transcriptome atlas of half a million cells, a multiome atlas pairing transcriptomic and epigenomic measurements within the same nuclei, and two spatial transcriptomic atlases of the injured spinal cord spanning four spatial and temporal dimensions. We integrated these atlases into a common framework to dissect the molecular logic that governs the responses to injury within the spinal cord[1]. The *Tabulae Paralytica* uncovered new biological principles that dictate the consequences of SCI, including conserved and divergent neuronal responses to injury; the priming of specific neuronal subpopulations to upregulate circuit-reorganizing programs after injury; an inverse relationship between neuronal stress responses and the activation of circuit reorganization programs; the necessity of re-establishing a tripartite neuroprotective barrier between immune-privileged and extra-neural environments after SCI and a failure to form this barrier in old mice. We leveraged the *Tabulae Paralytica* to develop a rejuvenative gene therapy that re-established this tripartite barrier, and restored the natural recovery of walking after paralysis in old mice. The *Tabulae Paralytica* provides a window into the pathobiology of SCI, while establishing a framework for integrating multimodal, genome-scale measurements in four dimensions to study biology and medicine.

Spinal cord injury (SCI) irreversibly damages neural tissues, leading to permanent and devastating loss of neurological functions[2,3]. Advances in management[4] and neurotechnologies[5–8] have improved survival and allow clinicians to address many aspects of neurological dysfunction after SCI. However, decades of investigations culminating in large-scale clinical trials have yet to identify safe and effective therapies to repair the injured spinal cord[1,3].

A SCI triggers a cascade of molecular and cellular responses involving inflammatory cell infiltration and cytokine release, apoptosis, demyelination, excitotoxicity, ischaemia and the formation of a fibrotic scar surrounded by an astrocyte border[1,2,9–11]. Altering the course of this cascade to repair the injured spinal cord will require a complete understanding of how neural and non-neural cells coordinate the response to SCI over time and throughout the lesion microenvironment.

Here we leveraged single-nucleus transcriptomics, multiomics and spatial transcriptomics in mice to establish the *Tabulae Paralytica*, or 'atlases of spinal cord injury' (Fig. 1a and Supplementary Video 1). Together, these atlases, comprising 482,825 individual cells spanning 18 experimental conditions and 71,499 spatial barcodes mapped onto the three-dimensional (3D) architecture of the injured spinal cord, provide a window into the pathobiology of SCI. We provide an interactive web application to explore these atlases at http://tabulaeparalytica.com.

Design of the snRNA-seq atlas

We optimized single-nucleus RNA sequencing (snRNA-seq) protocols for the injured spinal cord (Supplementary Fig. 1), and leveraged these protocols to conduct snRNA-seq profiling across a comprehensive set of experimental conditions and injury models that aimed to capture the multifaceted responses to SCI and how pharmacological interventions may alter these responses (Fig. 1b, Supplementary Figs. 2 and 3 and Supplementary Table 1).

The pathobiological responses activated in the injured spinal cord depend on the severity and mechanism of the initial insult, and evolve over the following days, weeks and months[3,4]. To capture these responses, we profiled the spinal cords of uninjured mice and mice

[1]NeuroX Institute, School of Life Sciences, Swiss Federal Institute of Technology (EPFL), Lausanne, Switzerland. [2]Defitech Center for Interventional Neurotherapies (.NeuroRestore), CHUV/UNIL/EPFL, Lausanne, Switzerland. [3]Lewis-Sigler Institute for Integrative Genomics, Princeton University, Princeton, NJ, USA. [4]Ludwig Institute for Cancer Research, Princeton University, Princeton, NJ, USA. [5]Wyss Center for Bio and Neuroengineering, Geneva, Switzerland. [6]Department of Neurosurgery, Lausanne University Hospital (CHUV) and University of Lausanne (UNIL), Lausanne, Switzerland. [7]Department of Clinical Neuroscience, Lausanne University Hospital (CHUV) and University of Lausanne (UNIL), Lausanne, Switzerland. [8]Bertarelli Platform for Gene Therapy, Swiss Federal Institute of Technology (EPFL), Lausanne, Switzerland. [9]Department of Neurobiology, David Geffen School of Medicine, University of California Los Angeles, Los Angeles, CA, USA. [10]These authors contributed equally: Michael A. Skinnider, Matthieu Gautier. [11]These authors jointly supervised this work: Mark A. Anderson, Jordan W. Squair, Grégoire Courtine. ✉e-mail: mark.anderson@epfl.ch; jordan.squair@epfl.ch; gregoire.courtine@epfl.ch

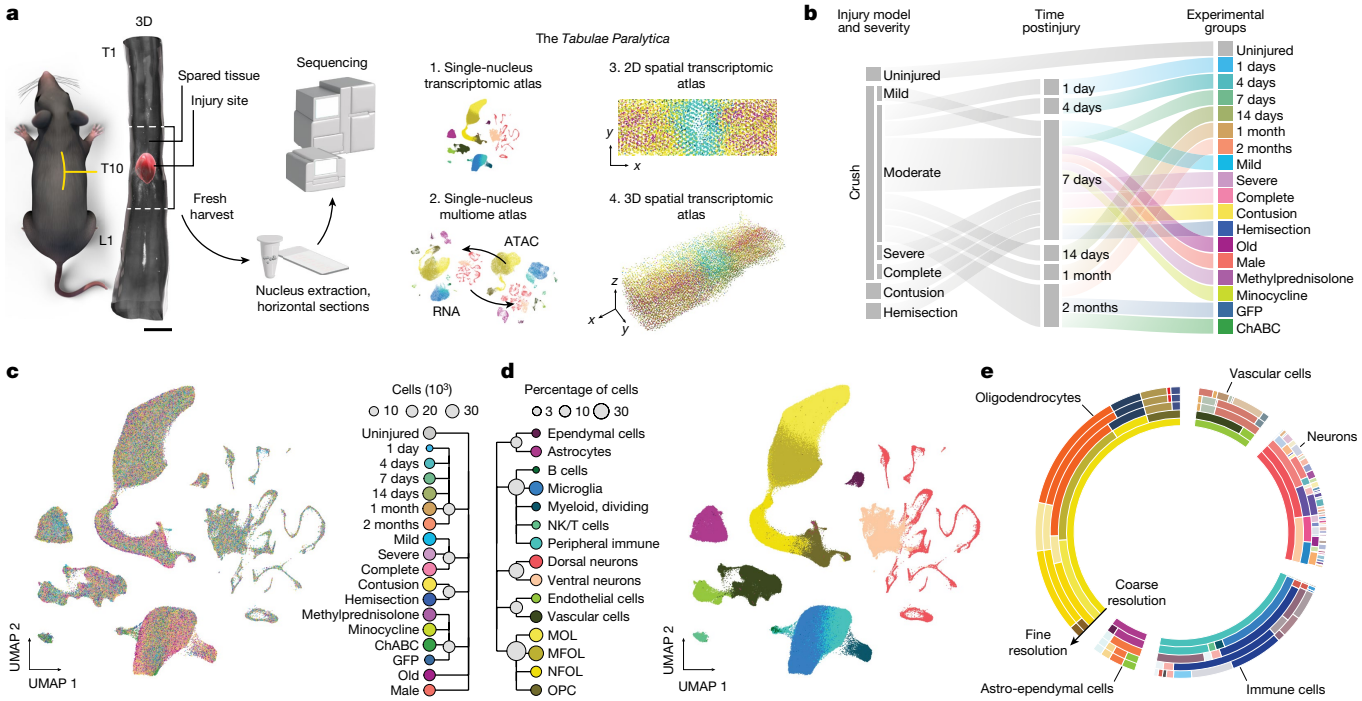

Fig. 1 | Overview of the *Tabulae Paralytica* and the snRNA-seq atlas. **a**, Schematic overview of the *Tabulae Paralytica*. Scale bar, 1 mm. **b**, Schematic overview of the snRNA-seq atlas ($n = 3$ mice per condition). **c**, UMAP visualizations of the 435,099 cells in the snRNA-seq atlas, coloured by experimental condition. Dendrogram shows major groups of experimental conditions. **d**, As in **c**, but coloured by experimental condition. Dendrogram shows the first two levels of the clustering tree of spinal cord cell types. **e**, Sunburst plot showing cell-type proportions in the snRNA-seq atlas at each level of the clustering tree, from broadest (innermost ring) to most granular (outermost ring).

at 1, 4, 7, 14, 30 and 60 days after mid-thoracic (T10) crush SCI. Next, we devised a progression of crush injury severities that led to mild, moderate, severe and complete functional impairments. Finally, we profiled the spinal cord following SCI induced by different mechanisms of injury, including contusion[12,13] and dorsal hemisection[14].

In humans, immune responses differ across the lifespan and between male and female individuals, with broad implications for disease initiation and progression. To evaluate the effect of sex and age on the cell-type-specific molecular programs activated by SCI, we profiled injured spinal cords from male and female mice, and from young and old mice.

Finally, we asked whether single-cell techniques could provide insights into the molecular mechanisms of pharmacotherapies for SCI. To address this question, we profiled the spinal cords of mice treated with three of the most extensively investigated clinical and experimental interventions: methylprednisolone, minocycline and chondroitinase ABC (ChABC).

Single-nucleus transcriptome atlas of SCI

We exploited this progression of 18 experimental conditions to establish a single-nucleus atlas of SCI, profiling the spinal cords of mice from each condition in biological triplicate by snRNA-seq. After stringent quality control, we obtained high-quality transcriptomes for a total of 435,099 nuclei from 52 mice (Fig. 1c,d and Supplementary Fig. 4).

To identify both coarse cell types and more granular subtypes, we subjected the entire dataset to several rounds of clustering at increasingly fine-grained resolutions. This procedure identified all the major cell types of the spinal cord and allowed us to establish a comprehensive catalogue of 175 more granular subpopulations. We organized these subpopulations into a clustering tree[15] that recapitulated the known cellular hierarchy of the spinal cord (Fig. 1e and Extended Data Fig. 1).

Coarse clustering identified cells originating from immune, astroependymal, vascular, oligodendrocyte and neuronal lineages (Supplementary Fig. 5). Subclustering further refined this taxonomy (Supplementary Note 1 and Supplementary Figs. 6–11). Within each of these lineages, we first explored the evolution of each subpopulation over time and with increasing injury severity.

Our snRNA-seq atlas recapitulated the known evolution of the immune response over the first 2 months following SCI[9]. Extensive infiltration of peripheral immune cells peaked between 7 and 14 days, paralleling the initiation and slow stabilization of microglial activation (Fig. 2b). The relative proportion of homeostatic microglia decreased gradually with injury severity, whereas the proportions of chemotaxis-inducing and inflammatory macrophages expanded (Supplementary Fig. 6d). These findings complement and extend previous single-cell studies of the immune response to SCI over the first week postinjury[16] (Supplementary Fig. 6e–g).

When an SCI occurs, astrocytes form a barrier that surrounds the fibrotic lesion core to protect viable neural tissue from infiltrating immune cells[10,17–20]. The proportion of protoplasmic astrocytes declined gradually over the first few days after injury (Supplementary Fig. 7h). The extent of this loss correlated with the severity of the injury (Supplementary Fig. 7i,j). By contrast, the reactive astrocyte compartment expanded immediately after injury, and persisted into the chronic stage (Supplementary Fig. 7k). To further study astrocyte responses, we applied tricycle[21] to estimate cell-cycle positions and identify actively proliferating cells within the astroependymal compartment (Fig. 2d). This analysis indicated that astrocytes entered the cell cycle starting at 1 day, with peak proliferation observed at 4 days (Fig. 2d). By 7 days, astrocytes had largely returned to G1/G0.

The cerebrovasculature comprises an arteriovenous axis of arteries, arterioles, capillaries, venules and veins. Together, these vessels form the blood–spinal cord barrier that separates the immune-privileged spinal cord parenchyma from the extra-neural environment. Our snRNA-seq atlas revealed an immediate and severity-dependent disruption of the cells that form the blood–spinal cord barrier following SCI. This disruption encompassed a contraction of the endothelial and

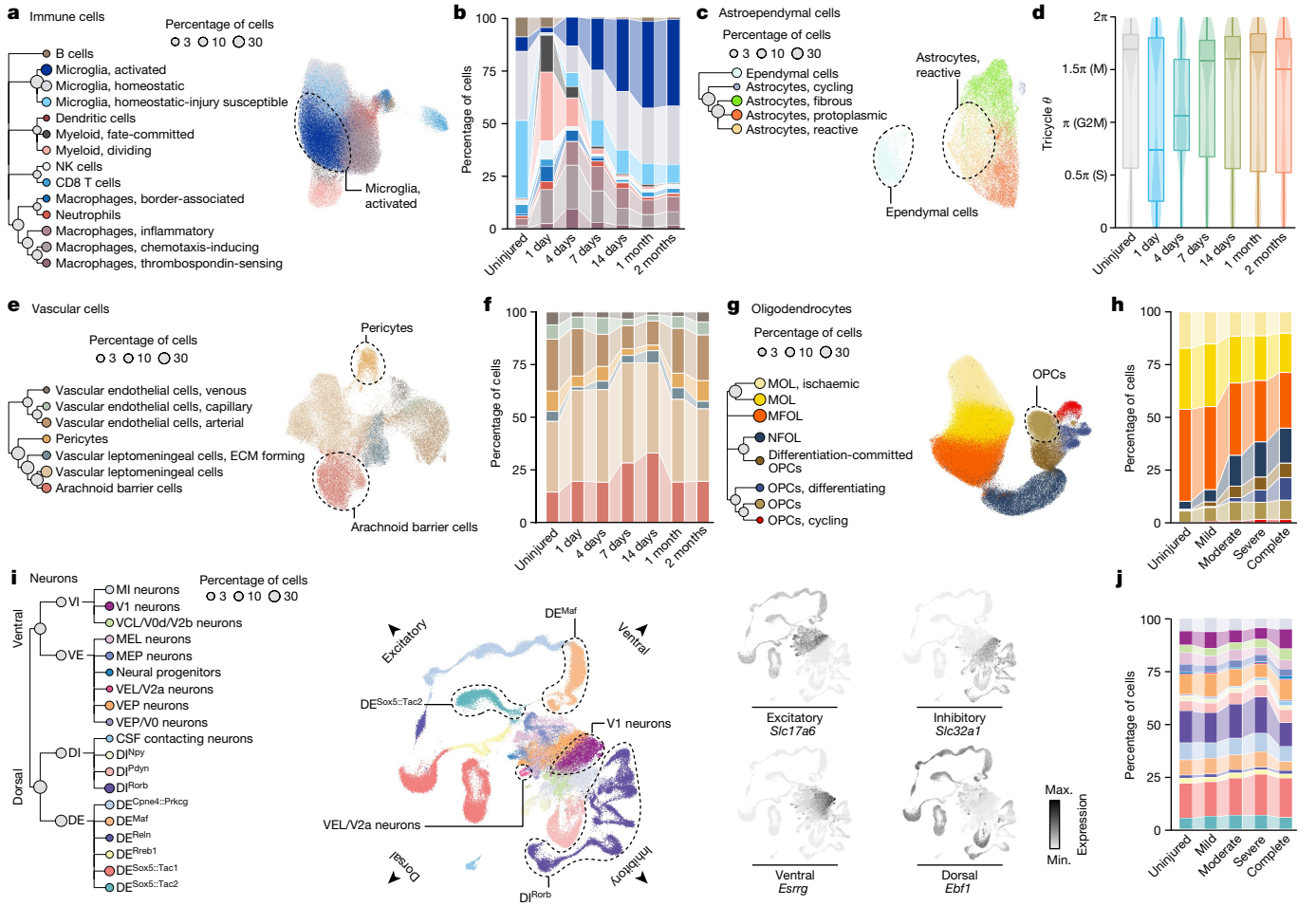

Fig. 2 | Cell types and subtypes of the uninjured and injured mouse spinal cord. a, UMAP visualization of 106,619 immune cells across 18 experimental conditions in the snRNA-seq atlas, coloured by cell type. Dendrogram shows the bottom four levels of the clustering tree, subset to show immune cell subtypes only. **b**, Proportions of each immune cell subtype across time points. **c**, As in **a**, but for 25,211 astroependymal cells. **d**, Cell-cycle stages assigned to astrocytes at each time point postinjury (n = 9,301). **e**, As in **a**, but for 40,620 vascular cells. **f**, Proportions of each vascular cell subtype across time points. **g**, As in **a**, but for 182,334 oligodendrocytes. **h**, Proportions of each oligodendrocyte subtype across injury severities. **i**, Left, as in **a**, but for 80,315 neurons. Right, UMAP visualization showing expression of canonical dorsal–ventral and inhibitory–excitatory marker genes. **j**, Proportions of each neuron subtype across injury severities. VI, ventral inhibitory; VE, ventral excitatory; DI, dorsal inhibitory; DE, dorsal excitatory.

pericyte compartments and a concomitant expansion in the proportion of vascular lepotomeningeal cells (VLMCs) (Fig. 2f and Supplementary Fig. 8d). Moreover, vascular cells showed a severity-dependent increase in the expression of genes associated with blood–brain barrier (BBB) dysfunction that increased over the first 4 days[22] (Supplementary Fig. 8e,f). By 7 days, we observed an expanded proportion of arachnoid barrier cells that are known to establish the cerebrospinal fluid (CSF) barrier[23,24] (Fig. 2f), and the downregulation of gene programs associated with BBB dysfunction[22]. Immunohistochemical analysis of albumin leakage within the spinal cord parenchyma recapitulated the early disruption followed by re-establishment of the blood–spinal cord barrier inferred from our snRNA-seq data (Supplementary Fig. 9).

The proportion of oligodendrocytes decreased at 1 day, consistent with the notion that they are sensitive to the ischaemic environment that develops after SCI[25]. By 4 days, we observed a severity-dependent expansion in the proportion of oligodendrocyte precursor cells (OPCs), which preceded the reinstatement of a near-normal oligodendrocyte compartment by 7 days (Fig. 2h and Supplementary Fig. 10d).

The spinal cord encompasses dozens of anatomically, functionally and transcriptionally distinct neuronal subpopulations. The scale of our snRNA-seq atlas, which comprised 80,315 single-neuron transcriptomes, allowed us to identify 60 distinct subpopulations of neurons (Fig. 2i and Supplementary Fig. 11), which are described in detail in Supplementary Note 1. Together, this atlas establishes a single-cell taxonomy of the mouse spinal cord, and delineates the effect of injury severity and time on the repertoire of cell types within the injured spinal cord.

Conserved and divergent neuron responses

A common feature of many insults to the nervous system is that specific neuronal subpopulations demonstrate disproportionate susceptibility or resilience to the insult. However, whether different neuronal subtypes within the spinal cord respond differentially to injury remains unknown.

To address this possibility, we compared the proportions of neurons from each subpopulation between injured and uninjured spinal cords. Our snRNA-seq atlas confirmed the expected severity-dependent loss of neurons after injury (Fig. 3a and Extended Data Fig. 2a). However, there were minimal changes in the relative proportions of each neuronal subpopulation, suggesting that spinal cord neurons are, in general, equally vulnerable to SCI (Fig. 2j).

The sole exception arose from CSF-contacting neurons[23,26,27], which showed a unique resilience to SCI (Fig. 3b and Extended Data Fig. 2b). This resilience was consistent across every comparison of injured and uninjured spinal cords, and became more pronounced with increasingly

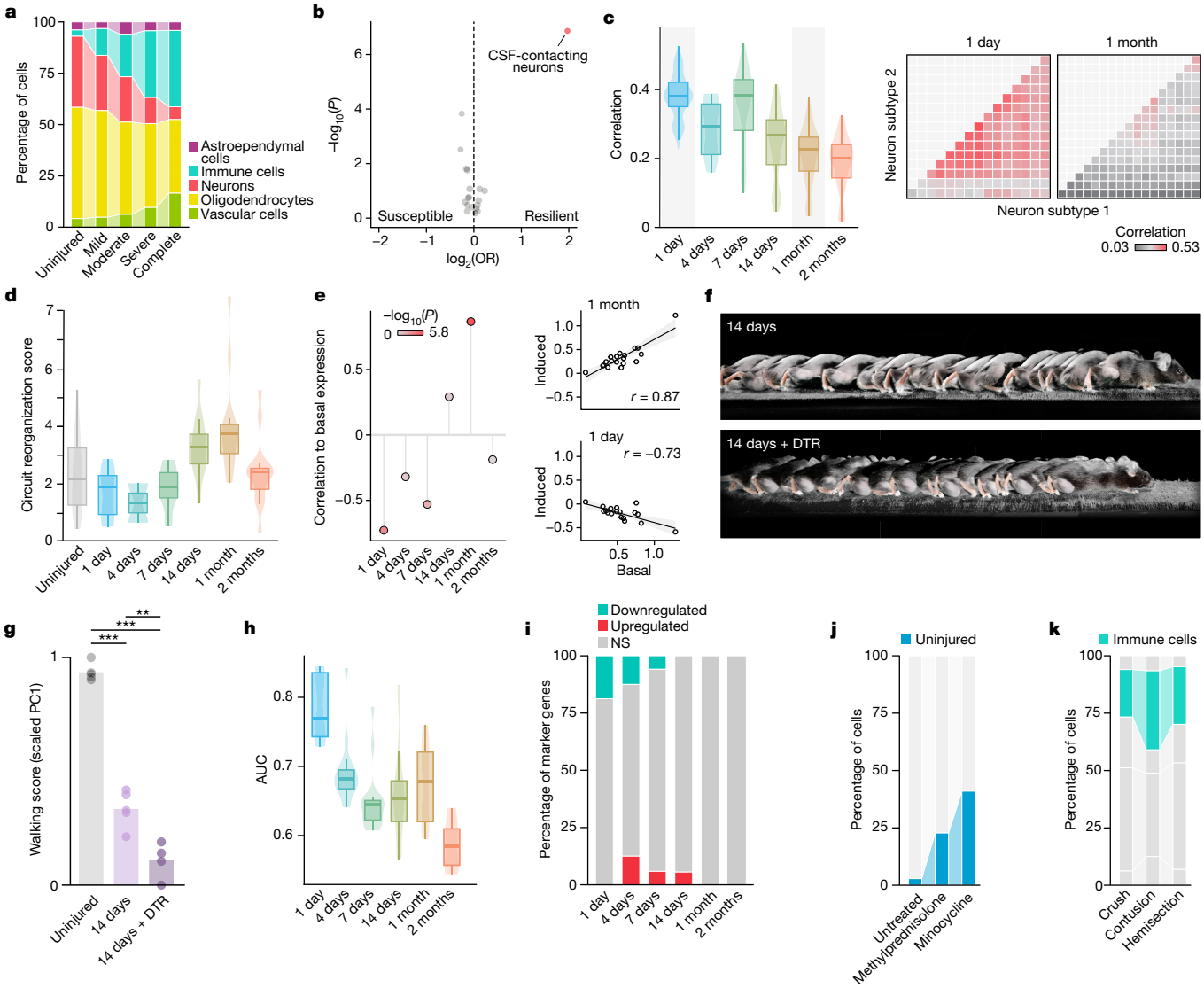

Fig. 3 | Biological principles governing the response to SCI. a, Proportions of each major spinal cord cell type across injury severities. **b**, Susceptible and resilient subtypes of spinal cord neurons. Volcano plot shows $\log_2$ odds ratios comparing neuron proportions between the uninjured spinal cord and each injured condition at 7 days postinjury (*x* axis) versus statistical significance (*t*-test, *y* axis). **c**, Left, transcriptome-wide correlations of DE signatures between each pair of neuron subtypes, across time points. Right, correlation matrices highlighting conserved DE at 1 day and divergent DE at 1 month. **d**, Expression of the circuit reorganization module in local Vsx2-expressing neurons at each time point postinjury. **e**, Left, correlations between basal and injury-induced expression of the circuit reorganization module across neuron subtypes, at each time point postinjury. Right, scatterplots showing the correlation between basal and induced expression across neuron subtypes at 1 day and 1 month. **f**, Chronophotography of walking in Vsx2^{Cre} mice after spontaneous recovery and in mice that received viral injections of AAV5-CAG-FLEX-DTR to induce cell-type-specific neuronal ablation before SCI. **g**, Walking performance of uninjured mice ($n = 5$), mice after spontaneous recovery ($n = 5$), and in mice with Vsx2^{ON} neuron ablation in the lower thoracic spinal cord ($n = 4$). **h**, Intensity of the transcriptional perturbation within each neuronal subtype, as quantified by Augur, across time points. **i**, Proportion of neuronal marker genes that are up- and downregulated at each time point. **j**, Proportion of neurons assigned an uninjured transcriptional phenotype in mice treated with methylprednisolone or minocycline, as compared to neurons from the untreated spinal cord. **k**, Proportions of immune cells in the spinal cord across injury models. NS, not significant; PC, principal component.

severe injuries (Extended Data Fig. 2c,d). Immunohistochemistry validated this resilience of CSF-contacting neurons (Extended Data Fig. 2e,f).

To characterize the transcriptional programs activated in response to injury within CSF-contacting neurons, we performed differential expression (DE) analysis (Extended Data Fig. 2g). Relative to other neuronal subpopulations, these neurons upregulated genes associated with cell adhesion (*Cntnap5c*), angiogenesis (*Rhoj*) and acute tissue remodelling (*Timp3*).

By contrast, other neuronal subpopulations showed a homogenous degree of vulnerability to SCI. We hypothesized that this homogeneity may coincide with the activation of shared transcriptional programs in response to injury. Indeed, we found that SCI initially triggered molecular responses that were broadly conserved across all neuronal subpopulations (Fig. 3c and Extended Data Fig. 3a). These responses gradually diverged over the following 2 months, as individual neuronal subpopulations activated increasingly distinct transcriptional programs (Fig. 3c).

This homogeneity compelled us to characterize this conserved early response of neurons to SCI (Extended Data Fig. 3b–d). We found that upregulation of immune response pathways, apoptotic programs and mitochondrial membrane disruption were the hallmarks of this response. Conversely, neurons downregulated core neuronal functions, including neurotransmitter release, ion channel expression and cell adhesion.

We next explored the gradual divergence of neuronal responses at later time points. This divergence coincided with the known timescale at which circuit reorganization mediates the natural recovery of neurological functions after SCI[2]. We therefore reasoned that this divergence might reflect subpopulation-specific circuit reorganization. Consistent with this possibility, we identified variable upregulation of genes associated with projection growth and morphogenesis across neuronal subpopulations, with maximal upregulation occurring between 14 days and 2 months after injury (Fig. 3d, Extended Data Fig. 3e and Supplementary Table 2).

Neurons expressing both *Vsx2* and *Nfib* (local Vsx2^{ON} neurons) showed the greatest upregulation of genes associated with circuit reorganization (Extended Data Fig. 3e,f). We found that Vsx2^{ON} neurons also showed the highest expression of genes associated with circuit reorganization in the uninjured spinal cord (Extended Data Fig. 3g,h). This observation raised the possibility that specific neuronal subpopulations may be intrinsically primed to serve as circuit-reorganizing cells after injury[2]. To study this possibility, we correlated the expression of circuit reorganization programs in each subpopulation of uninjured neurons with the upregulation of the same programs after injury. We identified a striking correlation between basal and injury-induced circuit reorganization programs between 14 days and 1 month postinjury, when these programs were maximally upregulated (Fig. 3e and Extended Data Fig. 3i). This time course coincides precisely with the temporal window of opportunity for the circuit reorganization that mediates natural recovery after SCI[2]. Together, these findings suggest that specific neuronal subpopulations are endowed with the inherent potential to upregulate genes associated with circuit reorganization after injury.

In view of the established roles of Vsx2^{ON} neurons located in the thoracic[28,29] and lumbar[8] spinal cords in the recovery of walking after SCI in response to regenerative or neuroprosthetic therapies, we asked whether these neurons were necessary for the natural recovery of walking after incomplete SCI. Consequently, we ablated Vsx2^{ON} neurons in the thoracic spinal cord (including both local and projecting neurons) 2 weeks before a moderate SCI. Whereas ablating Vsx2^{ON} neurons had no effect on walking before injury, this ablation prevented the natural recovery of walking after moderate SCI in these mice (Fig. 3f,g, Extended Data Fig. 3j–l and Supplementary Video 2).

Our analyses thus far exposed a temporal continuum between early-conserved and late-diverging neuronal responses following SCI. We sought to quantify the relative intensity of these time-dependent responses. To enable this quantification, we assessed the relative degree of transcriptional perturbation within each neuronal subpopulation over the course of recovery after SCI using Augur[30,31]. Augur is a machine-learning framework that quantifies the relative magnitude of the transcriptional response within any given cell type to an arbitrary perturbation, a procedure we refer to as cell-type prioritization. This prioritization revealed a pronounced neuronal response at 1 day that decreased in intensity over the subsequent days, and thereafter remained constant (Fig. 3h).

On the basis of these observations, we propose a model in which all neurons undergo a profound and broadly conserved transcriptional response immediately after injury that coincides with a dichotomous outcome of survival versus cell death. Over the subsequent weeks, the surviving neurons show gradually divergent transcriptional responses to injury, whereby only specific subpopulations upregulate genes associated with circuit reorganization. The degree of this injury-induced upregulation is encoded in the basal transcriptional state of each neuronal subpopulation, suggesting that specific subpopulations are primed to upregulate circuit-reorganizing genes following injury[2].

Surviving neurons remain differentiated

Single-cell studies have shown that neurons in the injured peripheral nervous system undergo dedifferentiation and loss of transcriptional identity following axonal injury[32,33]. We asked whether similar biological principles dictate neuronal responses in the injured central nervous system (CNS).

Contrary to single-cell analyses of peripheral neurons, we failed to identify a separate cluster of dedifferentiated neurons within the injured spinal cord at any time point (Fig. 2i). We reasoned that DE of neuronal marker genes could identify more subtle loss of transcriptional identity. However, we found that the vast majority of subpopulation-specific marker genes were neither up- nor downregulated across the entire time course of SCI (Fig. 3i and Extended Data Fig. 4a,b). This observation was robust to the statistical threshold used to identify neuronal marker genes (Extended Data Fig. 4c,d).

Collectively, these observations raise the possibility that transient loss of neuron transcriptional identity after injury may be a mechanism by which the peripheral nervous system maintains the distinct capacity to regrow severed nerves[34–36]. However, the CNS fails to recruit this mechanism after injury.

Growth-facilitating molecule expression

Following SCI, neural and non-neural cells express several families of molecules that can facilitate or inhibit axon growth and circuit reorganization[10,37–40]. These molecular pathways have historically been the main targets for interventions that aim to promote spinal cord repair[1], but the identities of the cells that produce these molecules are not well characterized. In Supplementary Note 2, we discuss how our snRNA-seq atlas can be used as a resource to identify the cell types that produce growth-promoting or inhibitory molecules following SCI, and dissect cell-type-specific responses to potential therapies, such as ChABC, that aim to target these molecules (Supplementary Fig. 12).

Molecular logic of immunomodulation

The earliest therapeutic approaches to SCI sought to inhibit immune responses to injury, with the aim of conferring neuroprotection. Preclinical studies suggested neuroprotective actions of methylprednisolone and minocycline, which led to large-scale clinical trials. However, these trials failed to demonstrate the effectiveness of these treatments to mediate functional recovery[41–43].

We asked whether our snRNA-seq atlas could address the disconnect between the established immunomodulatory activity of these drugs and their failure to ameliorate neurological function. Cell-type prioritization[30,31] confirmed that both methylprednisolone and minocycline triggered a profound transcriptional perturbation of the entire immune lineage (Supplementary Fig. 13a,b). However, this immunomodulation did not coincide with an increase in the survival of neurons (Supplementary Fig. 13c–e). This failure to protect neurons from cell death coincided with the lack of detectable neurological recovery.

Although these agents failed to improve the survival of neurons after SCI, we reasoned that they might induce more subtle transcriptional changes in the surviving neurons. Specifically, we hypothesized that these agents might repress the molecular programs activated by injury within neurons, thus promoting a shift towards an uninjured transcriptional phenotype. To test this hypothesis, we trained a machine-learning model to classify individual neurons as originating from injured versus uninjured spinal cords (Supplementary Fig. 13f–h). Applying this model to cells from mice treated with methylprednisolone or minocycline revealed a marked increase in the proportion of neurons that were classified as uninjured (Fig. 3j). Consistent with this prediction, surviving neurons treated with methylprednisolone downregulated transcriptional programs associated with innate and adaptive immune responses and cellular stress (Supplementary Fig. 13i,j).

Together, these findings indicate that methylprednisolone and minocycline modulate the immune responses to SCI, which in turn shifts the surviving neurons towards their basal transcriptional states.

However, these agents fail to alter the early, dichotomous outcome of survival versus cell death, and therefore fail to prevent neuronal death or improve neurological recovery.

Sexual dimorphism in the response to SCI

Sexual dimorphism in immune responses underlies differences in the prevalence of autoimmune disease between males and females[44,45]. Consequently, we hypothesized that transcriptional programs activated by SCI may also be sexually dimorphic. However, we identified few differences in cell-type proportions, cell-type-autonomous transcriptional programs or neurological outcomes between male and female mice (Supplementary Note 3 and Supplementary Fig. 14).

Cellular divergence between injury models

Preclinical studies of SCI require the selection of a relevant paradigm from a large repertoire of potential injury models. One important difference between these models is whether they explicitly open the meninges, which is thought to promote excessive immune cell infiltration. However, we found that the degree of peripheral immune invasion was broadly conserved across the injury models included in our snRNA-seq atlas (Fig. 3k and Supplementary Fig. 15a–c). We validated this finding by morphometrically quantifying Cd45-expressing cells, finding the number of these to be similar across injury models (Supplementary Fig. 15d,e). These observations suggest that crush and contusion injuries dismantle the blood–spinal cord barrier and cause extensive peripheral immune invasion that is not contingent on explicit meningeal disruption.

A second potential difference between preclinical paradigms is their relevance to human injuries. The most common mechanism of spinal cord damage in humans occurs through burst fractures and distraction injuries that impact the ventral spinal cord[46]. To understand whether our profiled injury models lead to differential perturbations of neurons along the dorsoventral axis, we used cell-type prioritization to quantify transcriptional responses in each neuronal subpopulation. Compared to crush injury, we found that dorsal hemisection and contusion injuries preferentially perturbed neurons in the dorsal spinal cord (Supplementary Fig. 15f), consistent with the direct application of force to the dorsal aspect of the spinal cord. Conversely, increasingly severe crush injuries induced balanced perturbations in dorsal versus ventral neurons (Supplementary Fig. 15g). These differences between rodent models of SCI must be considered when selecting an injury model for preclinical studies.

Failure of barrier formation in old mice

Ageing causes multifaceted changes in gene expression that culminate in dysregulated transcriptional responses to disease and biological perturbations, but whose cellular and functional consequences after SCI remain poorly understood. We found that the transcriptional differences between young and old mice after SCI were nearly as profound as those between injured and uninjured mice (Fig. 4a). The magnitude of this transcriptional perturbation was mirrored by extensive functional impairments in old mice compared to young mice (Fig. 4b,c, Supplementary Fig. 3e, Supplementary Video 3 and Supplementary Table 1). We sought to elucidate the mechanisms underlying these transcriptional and functional differences.

We first compared the proportions of cell types in the injured spinal cords of young and old mice. This comparison identified a markedly lower proportion of neurons in the spinal cords of old mice after injury compared to young mice, which was counterbalanced by an increase in the proportion of immune cells (Fig. 4d and Extended Data Fig. 5a,b). These pronounced differences in the cellular composition of the spinal cord were not observed in anatomical comparisons of uninjured young and old mice (Supplementary Fig. 16a). Anatomical assessments confirmed that old mice demonstrated more profound disruption of the blood–spinal cord barrier, with increased invasion of peripheral immune cells, and ultimately developed larger lesions compared to young mice, despite identical mechanisms of injury (Fig. 4e and Extended Data Fig. 5c,d). This difference in blood–spinal cord barrier function likewise was not observed in comparisons of uninjured young and old mice (Supplementary Fig. 16b).

We next asked how age affected the transcriptional responses to SCI within individual cell types. Cell-type prioritization[30,31] comparing cells from old and young mice with SCI revealed abnormal responses in infiltrating immune cells from old mice, including dividing myeloid progenitors, natural killer cells and T cells (Extended Data Fig. 5e). However, Augur also detected abnormal responses within cell types involved in the formation of the blood–spinal cord barrier and the astrocyte barrier, including extracellular matrix-forming VLMCs, capillary endothelial cells and OPCs. Consistent with this observation, we detected an age-dependent decrease in the proportion of *Id3*-expressing astrocytes, which form the astrocyte lesion border[47], and of arachnoid barrier cells, which form the CSF barrier (Extended Data Fig. 5f,g). Immunohistochemistry for SOX9 and ID3 confirmed these findings (Fig. 4f,g). Within the vascular compartment, we identified an age-dependent upregulation of gene programs associated with dysfunction of the BBB and downregulation of the specialized gene programs that enable vascular cells to establish the BBB[22], after injury (Fig. 4h, Extended Data Fig. 5h and Supplementary Table 2).

To dissect the transcriptional programs that are dysregulated in old mice, we performed DE analysis[48] of all the cell types in the spinal cord. In comparisons of old and young injured mice, we observed that many genes were DE within just a single cell type (Fig. 4i). Moreover, other genes showed opposing patterns of up- and downregulation across different cell types (Extended Data Fig. 5i,j). To quantify the coordination of the transcriptional responses to SCI across cell types, we devised statistical measures that aimed to capture both the variability of DE and changes in the direction of DE across cell types. These quantifications revealed that transcriptional responses to injury were profoundly discoordinated across the cell types of the spinal cord in old mice, relative to every other experimental comparison involving injured young mice (Fig. 4j and Extended Data Fig. 5i,j).

Together, these findings suggest that old mice fail to deploy the coordinated, multicellular response to SCI that naturally occurs in young mice, although we cannot exclude the possibility that some of the observed differences are present at baseline in the uninjured spinal cord. Notwithstanding this caveat, our snRNA-seq data demonstrates an age-dependent disruption of the cells that establish three essential neuroprotective barriers between the immune-privileged and extra-neural environments of the injured spinal cord: (1) the blood–spinal cord barrier; (2) the CSF–spinal cord barrier and (3) the border-forming astrocyte barrier (Fig. 4k). This disruption is accompanied by a dramatic increase in peripheral immune cell invasion, the uncontrolled expansion of the lesion, the loss of neurons adjacent to the injury site and an inability to coordinate the recovery of neurological functions.

A multiome atlas of SCI

Our snRNA-seq atlas uncovered the transcriptional programs triggered by SCI across the entire repertoire of cells in the spinal cord. However, we recognized that this atlas was intrinsically limited in its ability to reveal the regulatory mechanisms that underlie these transcriptional programs. To overcome this limitation, we compiled the second atlas of the *Tabulae Paralytica*: a multiomic atlas of the injured spinal cord (Fig. 5a).

We deployed single-nucleus multiomics to measure both RNA and accessible chromatin within the same individual cells, using the assay

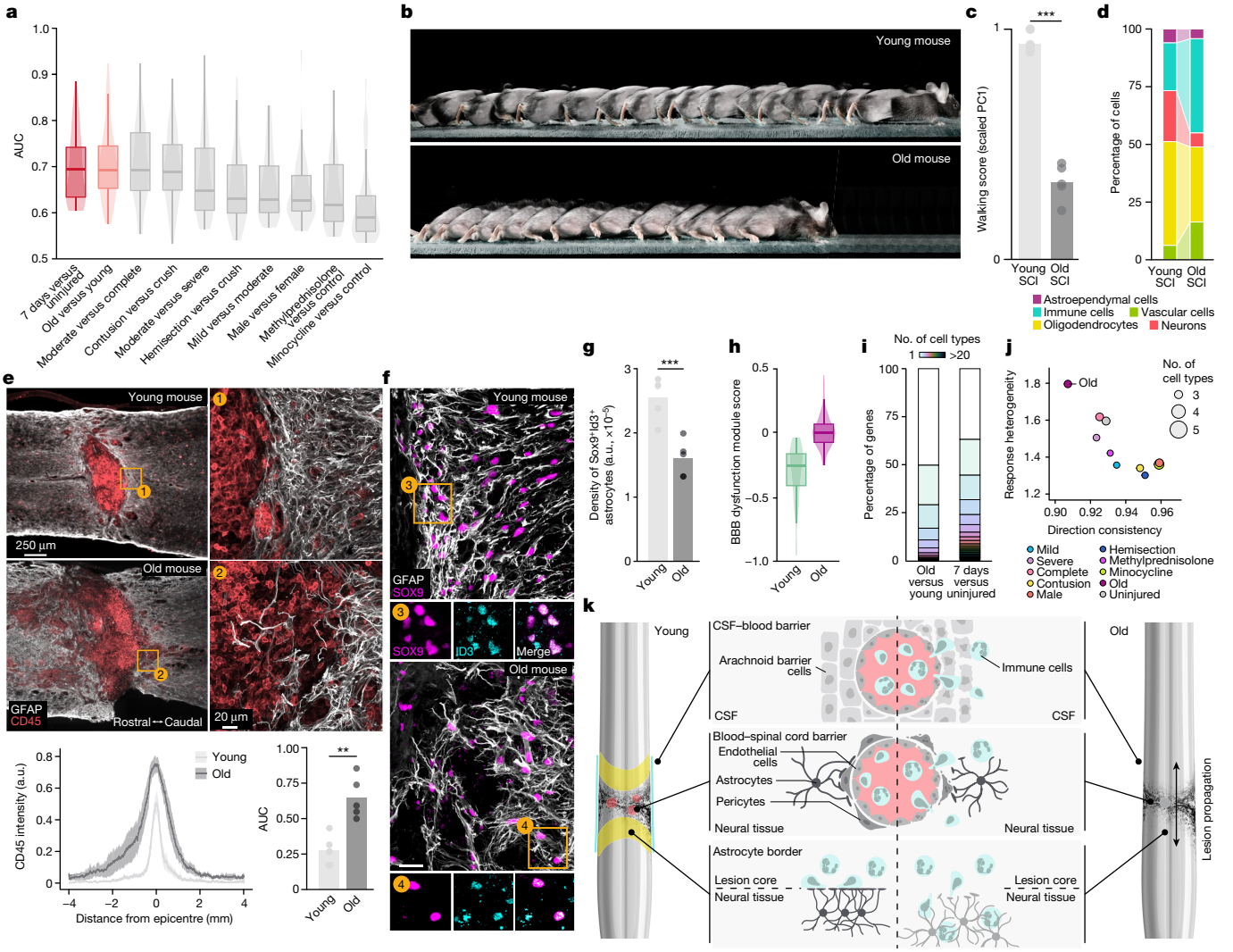

Fig. 4 | Failure to re-establish a tripartite neuroprotective barrier in old mice. a, Intensity of the transcriptional perturbation across all cell types of the spinal cord, as quantified by Augur, for all comparisons involving the injured spinal cord at 7 days postinjury. Comparisons between injured and uninjured mice, and old and young injured mice, are highlighted. **b**,**c**, Chronophotography (**b**) and walking performance ($n = 5$ each) (**c**) of young and old mice after spontaneous recovery from moderate crush SCI. **d**, Proportions of each major spinal cord cell type in young versus old mice after SCI. **e**, Composite tiled scans of GFAP and CD45 in horizontal sections from representative old and young mice. Bottom left, line graph demonstrates CD45 intensity at specific distances rostral and caudal to lesion centres. Bottom right, bar graph indicates the AUC (independent samples two-tailed *t*-test; $n = 5$ per group; $t = 4.57$; $P = 0.002$). **f**, Horizontal sections from representative old and young mice identifying a lack of $Sox9^{ON}Id3^{ON}$ cells in the astrocyte border region in old mice compared to young mice. Scale bar, 10 µm. **g**, Density of $Sox9^{ON}Id3^{ON}$ cells in the astrocyte border region (independent samples two-tailed *t*-test; $n = 5$ per group; $t = 4.84$; $P = 0.001$). **h**, Expression of the BBB dysfunction module in capillary endothelial cells from young and old mice at 7 days postinjury. **i**, Cell-type specificity of DE genes in comparisons of young versus old mice or injured versus uninjured mice. **j**, Heterogeneity of cell-type-specific DE in experimental comparisons involving the injured spinal cord at 7 days after SCI. Ageing is characterized by greater discoordination of gene expression than any other condition in the snRNA-seq atlas, as reflected by increased response heterogeneity and decreased direction consistency. **k**, Schematic overview of the cell types comprising the tripartite neuroprotective barrier. a.u., arbitrary units.

for transposase-accessible chromatin by sequencing (ATAC-seq). We leveraged these methodologies to profile the uninjured and injured spinal cords of mice at 7 days and 2 months postinjury. After quality control of both modalities[49], we obtained a dataset measuring gene expression and chromatin accessibility in 47,726 nuclei (Fig. 5b,c and Supplementary Fig. 17).

We aimed to link the multiomic atlas to the cellular taxonomy of the spinal cord that our snRNA-seq atlas had established. To overcome challenges in cell-type annotation within snATAC-seq data, we adapted an automated cell-type annotation approach[50] to hierarchically assign cell types and subtypes to each cell in the multiome atlas on the basis of the RNA modality. We validated the accuracy of this approach through cross-validation in the snRNA-seq atlas, and established that cell types were recovered at similar frequencies in both atlases (Supplementary Figs. 18–20).

We then leveraged this taxonomy to call peaks within each cell type and subtype at increasingly granular resolutions on the clustering tree (Supplementary Fig. 21)[49], and identified differentially accessible transcriptional factors within each subpopulation (Supplementary Figs. 22 and 23)[51].

Regulatory logic of barrier formation

Because our snRNA-seq atlas uncovered a number of biological principles that dictate the multifaceted responses to SCI in different cell types of the spinal cord, we sought to leverage our multiome atlas to

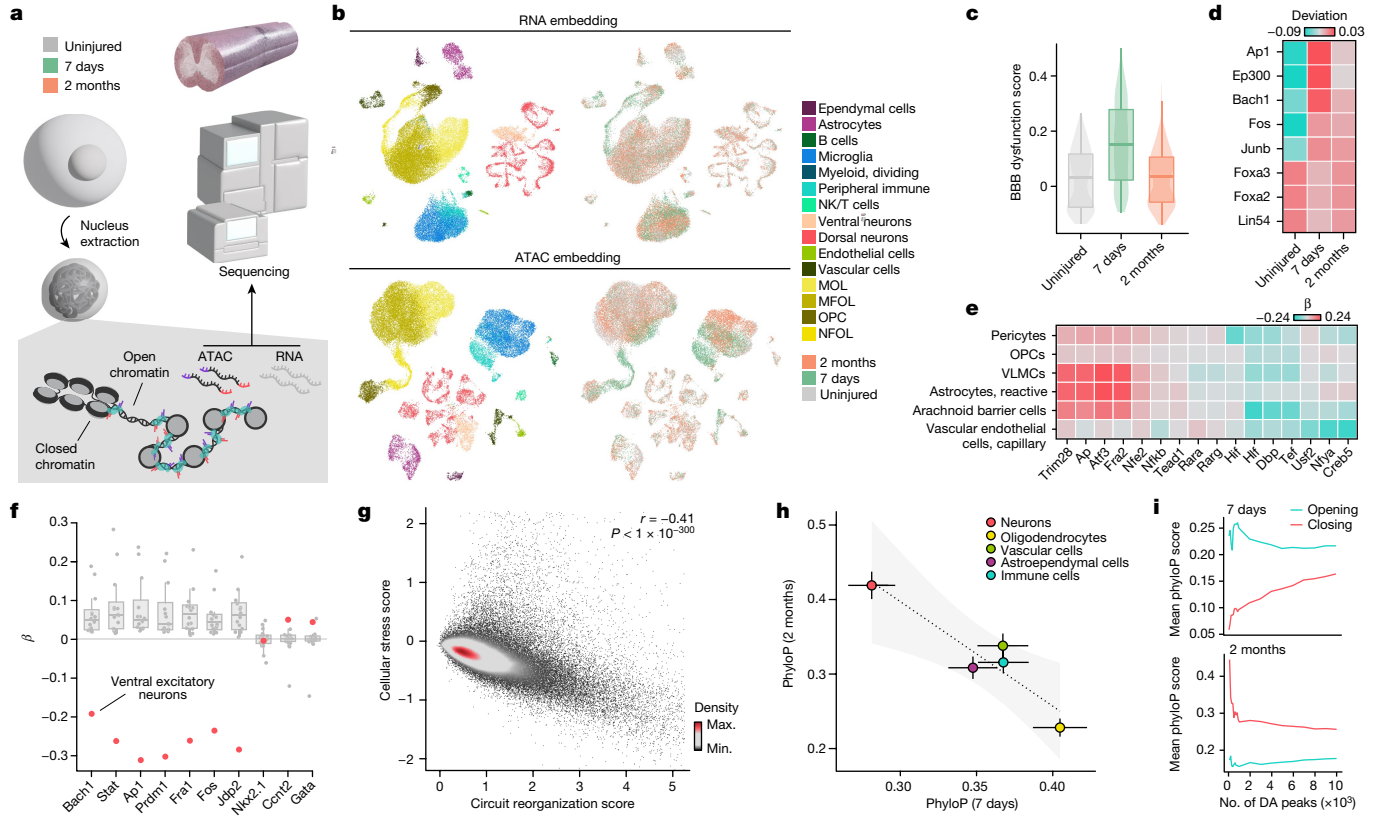

Fig. 5 | A multiomic atlas of SCI. a, Schematic overview of the multiome atlas. **b**, UMAP visualizations of the 40,256 cells in the multiome atlas, based on the RNA (top) or ATAC (bottom) modalities, and coloured by cell types (left) or experimental conditions (right). **c**, Expression of the BBB dysfunction module score in vascular cells across time points in the multiome atlas. **d**, Transcription factors for which motif accessibility in the ATAC modality correlated with expression of the BBB dysfunction module in the RNA modality across vascular cells in the multiome atlas. **e**, Selected transcription factors with significant differences in motif accessibility at 7 days in cell types that establish the tripartite barrier. **f**, Transcription factors showing significant variability in transcription factor binding across neuron subtypes at 2 months. Motif accessibility in ventral excitatory interneurons is highlighted. **g**, Anticorrelated expression of the circuit reorganization module, *x* axis, versus that of the cellular stress module, *y* axis, in 80,315 neurons from the snRNA-seq atlas. **h**, Mean phyloP scores of differentially accessible peaks in the major cell types of the spinal cord at 7 days, *x* axis and 2 months, *y* axis. Error bars show the standard error of the mean for each comparison. **i**, Mean phyloP scores of differentially accessible peaks that are opening or closing in neurons at 7 days or 2 months postinjury. Max., maximum. Min., minimum.

understand the regulatory programs that orchestrate these transcriptional responses.

We first aimed to dissect the gene regulatory programs involved in the re-establishment of the tripartite barrier after SCI. Because our multiome atlas recapitulated the upregulation of gene programs associated with BBB dysfunction that we had observed in the snRNA-seq atlas (Fig. 5c), we leveraged the ATAC modality to identify the transcriptional factors that underlie this dysfunction. To exploit the link between RNA and ATAC modalities, we correlated the accessibility of transcriptional factor binding motifs to the expression of these gene programs within the same cell (Supplementary Fig. 24a). Within vascular cells, the expression of the BBB dysfunction program[22] was correlated with the accessibility of transcription factors associated with cellular stress and inflammation (*Ap1*, *Junb*, *Bach1* and *Fos*[52]) and hypoxia-induced VEGF (vascular endothelial growth factor) stimulation (*Ep300*), and anticorrelated with the accessibility of transcription factors driving cellular proliferation (*Foxa2*, *Foxa3* and *Lin54*; Fig. 5d and Supplementary Fig. 24b).

These responses were mirrored by shared and cell-type-specific regulatory programs in the other cellular subpopulations that coordinate the formation of the tripartite barrier (Fig. 5e and Supplementary Fig. 24c). VLMCs, pericytes and arachnoid barrier cells showed decreased accessibility of transcription factors known to modulate the permeability of the blood–brain or CSF barriers (*Rarg* and *Hif1*), whereas arachnoid barrier cells and pericytes showed decreased accessibility of transcription factors that govern barrier efflux of metabolites and that regulate neuronal activity (*Dbp* and *Tef*). Finally, border-forming astrocytes showed increased accessibility of several transcription factors associated with acute responses to stress or hypoxia[53], including *Junb*, *Bach1*, *Fos* and *Ep300*.

Regulatory logic of neuronal responses

Our snRNA-seq atlas established that SCI triggers an immediate transcriptional response that is conserved across all neuronal subpopulations. Conversely, we found that transcriptional responses gradually diverged between neuronal subpopulations over time after SCI (Fig. 3c). We therefore next sought to understand the regulatory programs that govern neuronal responses to SCI as well as their associated functional consequences and potential origins.

In the multiome atlas, we observed that the early-conserved transcriptional response was mirrored by conserved regulatory programs that involved increased accessibility of transcription factors associated with cellular stress (*Myc* and *Nfe2*) and apoptosis (*Tfap2*) (Supplementary Fig. 25a). To characterize late-diverging regulatory programs, we devised a permutation-based statistical approach that evaluated variability in transcription factor binding across all subpopulations of neurons (Supplementary Fig. 25b). We found that this variability originated from divergent regulatory responses within a mixed population of ventral excitatory interneurons, containing several subtypes of

V0 neurons known to be involved in the control of movement (Fig. 5f and Supplementary Fig. 25c). Whereas every other subpopulation of neurons showed increased accessibility of transcription factors associated with cellular stress responses (*Ap1*, *Stat*, *Bach1* and *Fos*), this subpopulation of ventral excitatory interneurons instead showed decreased accessibility of these transcription factors.

The results from our snRNA-seq atlas revealed that these and other ventral excitatory interneurons express genes implicated in circuit reorganization at high levels (Extended Data Fig. 3e). The distinctive lack of cellular stress responses within these neurons led us to hypothesize that, in general, neurons face an inherent trade-off between the expression of cellular stress response programs and transcriptional programs associated with circuit reorganization. To test this hypothesis, we re-examined our snRNA-seq atlas and confirmed the existence of an anticorrelation between the expression of programs related to stress response versus circuit reorganization (Fig. 5g and Supplementary Table 2), which could not be explained by the presence of low-quality neurons (Supplementary Fig. 25d–f). These observations suggest a model whereby the ability of different neuronal subpopulations to participate in circuit reorganization is intrinsically linked to the intensity of their response to cellular stress.

Neuronal responses to injury vary markedly across the tree of life, to the extent that neurons from primitive vertebrates can demonstrate spontaneous regeneration whereas neurons from adult mammals fail to regenerate after SCI[11]. This divergence compelled us to characterize the evolutionary conservation of the genomic regions that become differentially accessible following SCI. We used phyloP[54] to quantify the sequence conservation of these regions, and identified profound differences in the evolutionary conservation of differentially accessible peaks within neurons, as compared to glia (Fig. 5h and Supplementary Fig. 26a–c). Inspecting these differences more closely, we discovered dichotomous patterns of evolutionary conservation for peaks that opened versus closed in neurons after SCI (Fig. 5i and Supplementary Fig. 26d–f). In the acute phase of SCI, neurons showed increased accessibility of evolutionarily conserved genomic regions, which was mirrored by decreased accessibility of evolutionarily accelerated genomic regions. These trends were reversed 2 months after SCI, when evolutionarily accelerated regions showed increased accessibility.

Together, these observations reveal an inverse relationship between cellular stress responses and the activation of circuit reorganization programs across the 80,315 neurons in our snRNA-seq atlas. We observe that the upregulation of gene programs associated with circuit reorganization coincides temporally with the opening of evolutionarily accelerated genomic regions, particularly in ventral excitatory interneurons.

A spatial transcriptomic atlas of SCI

Interrogation of our snRNA-seq and multiome atlases identified cell-type-specific transcriptional and regulatory programs triggered by SCI. However, these transcriptional and regulatory programs were identified in dissociated cells and, therefore, could not be visualized within the complex microenvironment of the injury. To overcome this limitation, we resolved these programs within the cytoarchitecture of the spinal cord using spatial transcriptomics (Fig. 6a).

We profiled the spinal cords of uninjured and injured mice at 7 days and 2 months after SCI, and obtained 33,941 high-quality spatial barcodes from 36 transverse sections (Supplementary Fig. 27). To permit direct comparison across experimental conditions, we registered all 36 sections to a common coordinate system[8] (Fig. 6b).

The coordinated, multicellular response to SCI establishes a thin astrocyte barrier that separates the fibrotic lesion core from surrounding immune-privileged neural tissue. The requirements to promote neural repair are known to differ between these distinct lesion compartments, but the underlying molecular logic remains incompletely understood[1,2]. We leveraged our spatial atlas to uncover the molecular programs that are shared between, or specific to, each of these compartments.

To identify molecular differences between lesion compartments, we demarcated spatial barcodes corresponding to the fibrotic scar, the astrocyte barrier and the adjacent neural tissue (Fig. 6c and Supplementary Fig. 28). We then performed DE analysis to identify genes specific to each lesion compartment, and dissected the cellular composition of each lesion compartment by deconvolving the cell types within each spatial barcode (Fig. 6d–h, Extended Data Figs. 6 and 7, Supplementary Fig. 29 and Supplementary Note 4).

To quantify the relative degree of transcriptional perturbation throughout the lesion microenvironment, we applied Magellan[8]. Magellan is a machine-learning framework that quantifies the relative magnitude of the transcriptional response at any given spatial locus to an arbitrary perturbation, a procedure we refer to as spatial prioritization (Supplementary Fig. 30a). This prioritization recovered the profound transcriptional perturbation occurring at the lesion core during the first 7 days after injury, with a gradient of decreasing intensity that spread radially throughout the spared but reactive neural tissue adjacent to the fibrotic scar (Fig. 6i and Supplementary Fig. 30b). Spatial prioritization also captured the contraction of the injury border after 2 months of recovery from SCI (Fig. 6j and Supplementary Fig. 30c,d).

These results illustrate how spatial prioritization accurately recovered the two-dimensional (2D) architecture of the evolving injury. We therefore asked whether spatial prioritization could also provide a resource to identify the molecular programs that elaborate this architecture, without any a priori definition of the lesion compartments. To answer this question, we tested for correlation between the spatial prioritization scores assigned to each barcode by Magellan and the expression of individual genes (Extended Data Fig. 8a–c). As anticipated, this approach recovered many of the genes associated with canonical lesion compartments, including extracellular matrix molecules at the lesion core (*Col1a1* and *Col13a1*) and neuronal genes (*Nefl* and *Nefh*) in spared but reactive neural tissue (Fig. 6k and Extended Data Fig. 8d–f). Similarly, we tested for correlation between the spatial prioritizations assigned by Magellan and the average expression of all genes associated with a given Gene Ontology (GO) term. This analysis recapitulated the multifaceted innate and adaptive immune responses within the lesion site (Supplementary Fig. 31).

We then asked whether the spatial transcriptomic atlas could identify genes whose correlation to the perturbation response differed between 7 days and 2 months after SCI. To answer this question, we tested for differential correlation between spatial prioritization scores and gene expression at 7 days and 2 months post-SCI (Supplementary Fig. 32a). This analysis highlighted genes (*Gfap, Aqp4* and *Apod*) coinciding with the location of the astrocyte barrier, reflecting the contraction of this border that takes place between 7 days and 2 months after injury (Fig. 6l and Supplementary Fig. 32b). Beyond the astrocyte barrier, differential prioritization also pointed to temporal evolution in the innate and adaptive immune responses, including immediate microglial activation (*Wfdc17* and *Spp1*) and lymphocyte homing (*Stab1*), which contrasted with delayed complement activation (*C3*) and monocyte maturation (*Ms4a7*) (Fig. 6k and Supplementary Fig. 32b). Repeating this differential prioritization at the level of GO terms highlighted the spatial evolution of astrocyte differentiation, vascular endothelial growth factor production and phagocytosis (Fig. 6l and Supplementary Fig. 33).

Spatial prioritization also allowed us to uncover less appreciated aspects of the biology of an SCI. For example, we identified chronic activation of immunoglobulin factors (*Ighg2c*, *Jchain* and *Igha*) within the lesion core, which probably contribute to maintaining host defences and antigen binding within the fibrotic core (Supplementary Fig. 32b).

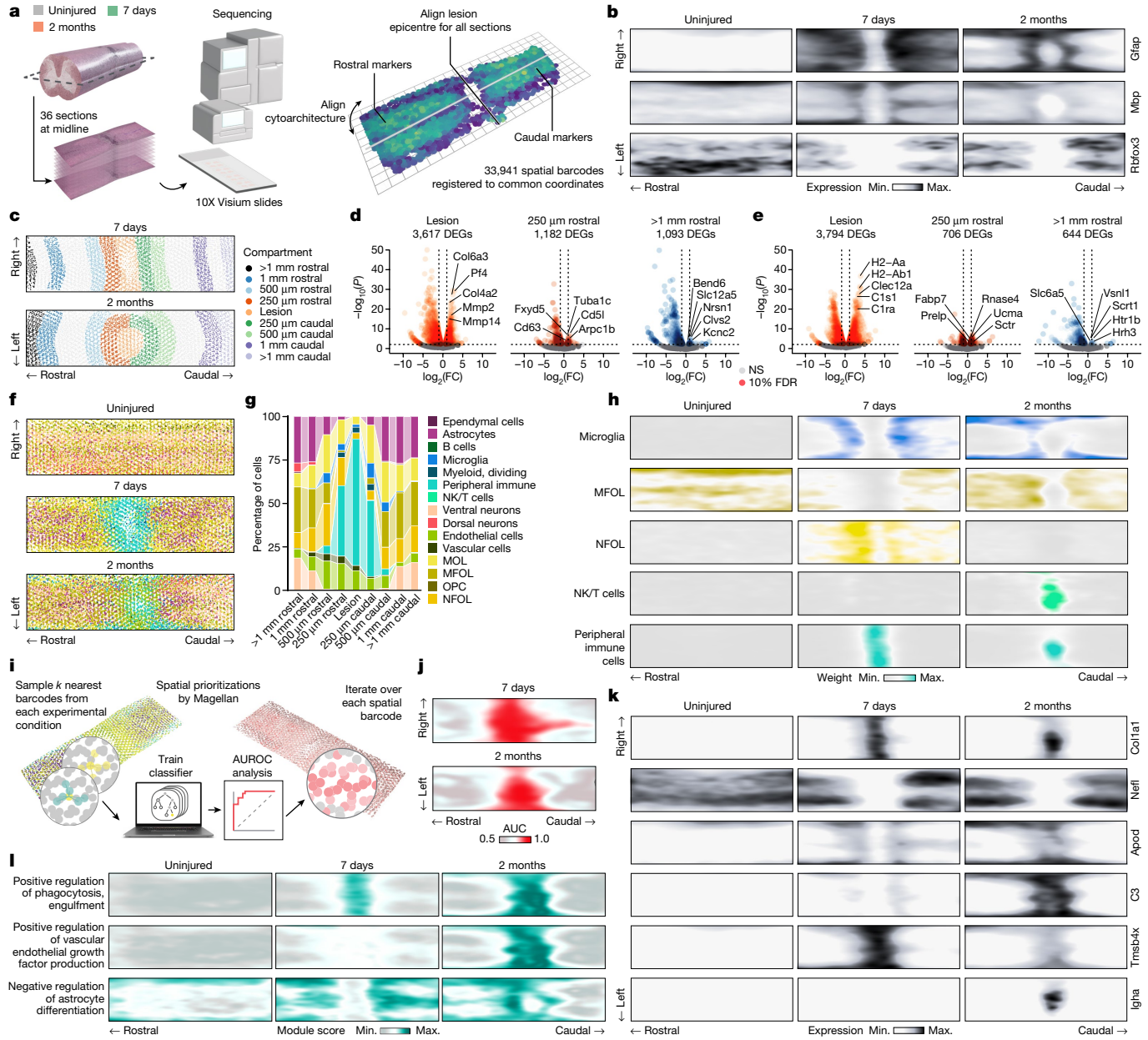

Fig. 6 | A spatial transcriptomic atlas of SCI. a, Schematic overview of the 2D spatial transcriptomic atlas. **b**, Computational histology of key marker genes on the 2D common coordinate system of the spinal cord. **c**, Legend showing the position of each lesion compartment on the coordinate system of the spinal cord. **d**,**e**, Volcano plots showing compartment-specific genes at 7 days (**d**) and 2 months (**e**) for a subset of the lesion compartments discussed in the text. **f**, Cell-type deconvolution of spatial barcodes in the 2D spatial transcriptomic atlas. **g**, Cellular composition of each lesion compartment at 7 days postinjury, as determined by cell-type deconvolution. **h**, Deconvolution weights assigned by RCTD to selected cell types. **i**,**j**, Spatial prioritizations assigned by Magellan to each spatial barcode at 7 days (**i**) and 2 months (**j**). AUC, area under receiver operating curve. **k**,**l**, Expression of selected genes (**k**) and GO term modules (**l**) prioritized by their correlation to spatial prioritizations assigned by Magellan at each spatial barcode. MFOL, myelin forming oligodendrocytes; NFOL, newly formed oligodendrocytes.

Spatial prioritization also highlighted a robust expression of *Dbi*[55] along the lesion border (Supplementary Fig. 32b). As *Dbi* modulates the activity of the neurotransmitter γ-aminobutyric acid, the expression of this gene may be involved in the reported reduction of neuronal activity in the vicinity of lesion borders. Moreover, our analyses identified *Prdx6* as highly associated with the lesion border, suggesting the expression of this antioxidant enzyme may protect the surrounding reactive neural tissue from oxidative injury (Supplementary Fig. 32b). Last, spatial prioritization identified distinct subcompartments of the lesion core itself. We observed that genes associated with iron metabolism (*Flt1*) expressed diffusely throughout the lesion, but genes associated with fat metabolism (*Plin2*) confined to the innermost aspects of the lesion core, and genes associated with actin sequestration (*Tms4bx*) extending out along the lesion edges (Fig. 6k and Extended Data Fig. 8f).

To validate the spatial localization of genes identified through DE analysis of lesion compartments or spatial prioritization with Magellan, we carried out further in situ hybridization and immunohistochemical analyses. These experiments recapitulated the localization of genes prioritized by both methods, including *Col1a1*, *Id3*, *Plin2* and *Tmsb4x* (Supplementary Fig. 34).

Together, these results establish a resource to explore the multicellular responses to SCI across the cytoarchitecture of the spinal cord, and validate the ability of spatial prioritization to resolve both well-documented and new aspects of these responses.

A 4D spatial atlas of SCI

The ability to visualize the CNS in three dimensions using tissue clearing technologies has opened new possibilities to study the anatomy and function of the nervous system[56]. Analogously, we reasoned that expanding our spatial transcriptomic atlas into a third spatial dimension would enable a more complete description of the biology of SCI. We further surmised that our snRNA-seq and multiome atlases could be overlaid onto this 3D model of the spinal cord to resolve the spatiotemporal distribution of the transcriptional and regulatory responses across the compendium of experimental conditions included in our *Tabulae*.

To develop a four-dimensional (4D) spatial atlas of the spinal cord, we collected 16 tissue sections that were equally spaced along the dorsoventral axis of spinal cords from uninjured and injured mice at 7 days and 2 months after SCI (Fig. 7a). The distance between each section was approximately 50 µm, which ensured a dense coverage of the third spatial dimension. After quality control and registration to a common 3D coordinate system, we obtained a dataset comprising 37,558 spatial barcodes from 48 sections (Supplementary Fig. 35).

To validate the construction of our 4D atlas, we first confirmed that our dataset resolved the established spatial distributions of cell types in the uninjured and injured spinal cord, and inspected the expression of well-studied inhibitory and facilitating molecules (Fig. 7b, Extended Data Fig. 9, Supplementary Fig. 36 and Supplementary Note 5).

To increase the resolution of this spatiotemporal atlas, we again leveraged our snRNA-seq atlas to deconvolve the cellular composition of each spatial barcode (Supplementary Figs. 37 and 38). This procedure resolved cellular subpopulations within highly specific locations, such as ependymal cells and border-forming macrophages. Moreover, dorsal and ventral neurons were appropriately separated along the coronal plane, and the locations of specific neuronal subpopulations such as CSF-contacting neurons, Vsx2-expressing neurons and motor neurons were correctly resolved (Fig. 7c).

We next aimed to integrate all the *Tabulae* into a single, unified framework. Using Tangram, we embedded single-nucleus transcriptomes and epigenomes onto our 4D atlas of the mouse spinal cord, generating a unified dataset of 554,324 single-nucleus or spatial barcodes that were each associated with a full transcriptome, an experimental condition and *x*, *y* and *z* coordinates (Fig. 7d).

We then applied Magellan to the integrated spatial dataset. This spatial prioritization reflected the severity-dependent increase in transcriptional perturbation within increasing injury severity (Fig. 7e). Consistent with these observations, Magellan captured severity-dependent changes in genes associated with peripheral immune cell invasion, astrocytic demarcation of the lesion and neuronal death (Supplementary Fig. 39). Moreover, we spatialized the expression of conserved early neuronal responses, as well as late-diverging expression of programs associated with circuit reorganization (Supplementary Fig. 40). We then linked these changes in cell-type composition and gene expression to transcription factor accessibility by spatializing the accessibility of transcription factors involved in the establishment of the tripartite barrier (Fig. 7f and Supplementary Fig. 41).

Our snRNA-seq atlas identified a profound transcriptional perturbation across spinal cord cell types in old mice following SCI. We therefore sought to understand the spatial distribution of this perturbation. Magellan revealed that old mice developed an expanded and poorly circumscribed territory of transcriptional perturbation as compared to young mice, reflecting their failure to re-establish the tripartite neuroprotective barrier. This failure was reflected by global upregulation of the BBB dysfunction module, and downregulation of gene expression programs associated with BBB identity (Fig. 7g and Supplementary Fig. 42). Three-dimensional visualization of genes associated with peripheral immune invasion underscored the failure to demarcate the lesion in old mice (Fig. 7h).

Collectively, these results establish the feasibility of constructing an integrated transcriptomic and epigenomic atlas of healthy and perturbed tissues across four spatiotemporal dimensions.

Enhanced barrier formation restores walking

The *Tabulae Paralytica* documented the spatially and temporally dependent activation of transcriptional and regulatory mechanisms that are triggered after SCI to re-establish a tripartite neuroprotective barrier. Conversely, our snRNA-seq atlas identified disruption of the cell types and subtypes that establish the tripartite barrier in old mice (Fig. 4d,h and Extended Data Fig. 5a–h), and this disruption was accompanied by poorly circumscribed lesions (Fig. 4e–g), a decrease in the proportion of surviving neurons (Fig. 4d) and impaired recovery of neurological functions (Fig. 4b,c and Supplementary Video 3). These observations led us to hypothesize that interventions that accelerate wound repair by promoting the formation of the tripartite barrier could restore neurological functions in old mice.

Because we found that the number of *Id3*-expressing, border-forming astrocytes was decreased in old mice (Fig. 4f,g), we reasoned that increasing their production would accelerate the formation of the astrocyte barrier, limiting lesion size and preserving neurological function. We previously found that the delivery of epidermal growth factor (EGF) and fibroblast growth factor 2 (FGF2) increased both the proliferation and absolute number of border-forming astrocytes[37]. Moreover, it is established that the delivery of VEGF accelerates endothelial cell proliferation and reformation of vascular networks[57]. We therefore engineered lentiviruses to overexpress *Egf*, *Fgf2* and *Vegf* and, as a proof-of-principle test, delivered these vectors to the lower thoracic spinal cord 2 days before SCI (Fig. 8a and Extended Data Fig. 10a). This procedure increased the production of border-forming astrocytes, reduced the number of $CD45^+$ infiltrating immune cells, augmented the re-establishment of the blood–spinal cord barrier and resulted in smaller and more circumscribed lesions (Fig. 8b,c and Extended Data Fig. 10b–e). In addition, treated old mice showed a natural recovery of walking resembling that of young mice subjected to the same severity of SCI (Fig. 8d–f, Extended Data Fig. 10f,g and Supplementary Video 3).

Together, these findings demonstrate that interventions that augment the tripartite neuroprotective barrier and thereby maintain the immune-privileged environment of the spinal cord can prevent the exaggerated neural damage resulting from SCI in aged mice.

Discussion

SCI triggers a coordinated cascade of cellular and molecular responses, whose spatiotemporal complexity has thus far prevented the development of safe and effective therapies to repair the injured spinal cord. To help to unravel this complexity, we established the *Tabulae Paralytica*: a resource comprising multimodal single-cell and spatial atlases of SCI. We profiled RNA expression in more than 400,000 nuclei, spanning 18 experimental conditions that captured the most commonly studied manipulations in basic and translational research on SCI that could be made accessible for these experiments. The scale of our snRNA-seq atlas significantly extends past single-cell studies of the injured spinal cord, enabling a more complete characterization of the cellular and molecular responses triggered by injury[16,58,59]. We simultaneously profiled the dynamics of chromatin accessibility and gene expression in a further 40,000 cells to dissect the regulatory programs that direct the response to injury. To delineate these responses within the cytoarchitecture of the injured spinal cord, we generated a spatial transcriptomic atlas of the injury that we extended into four spatial and temporal dimensions. We integrated these atlases

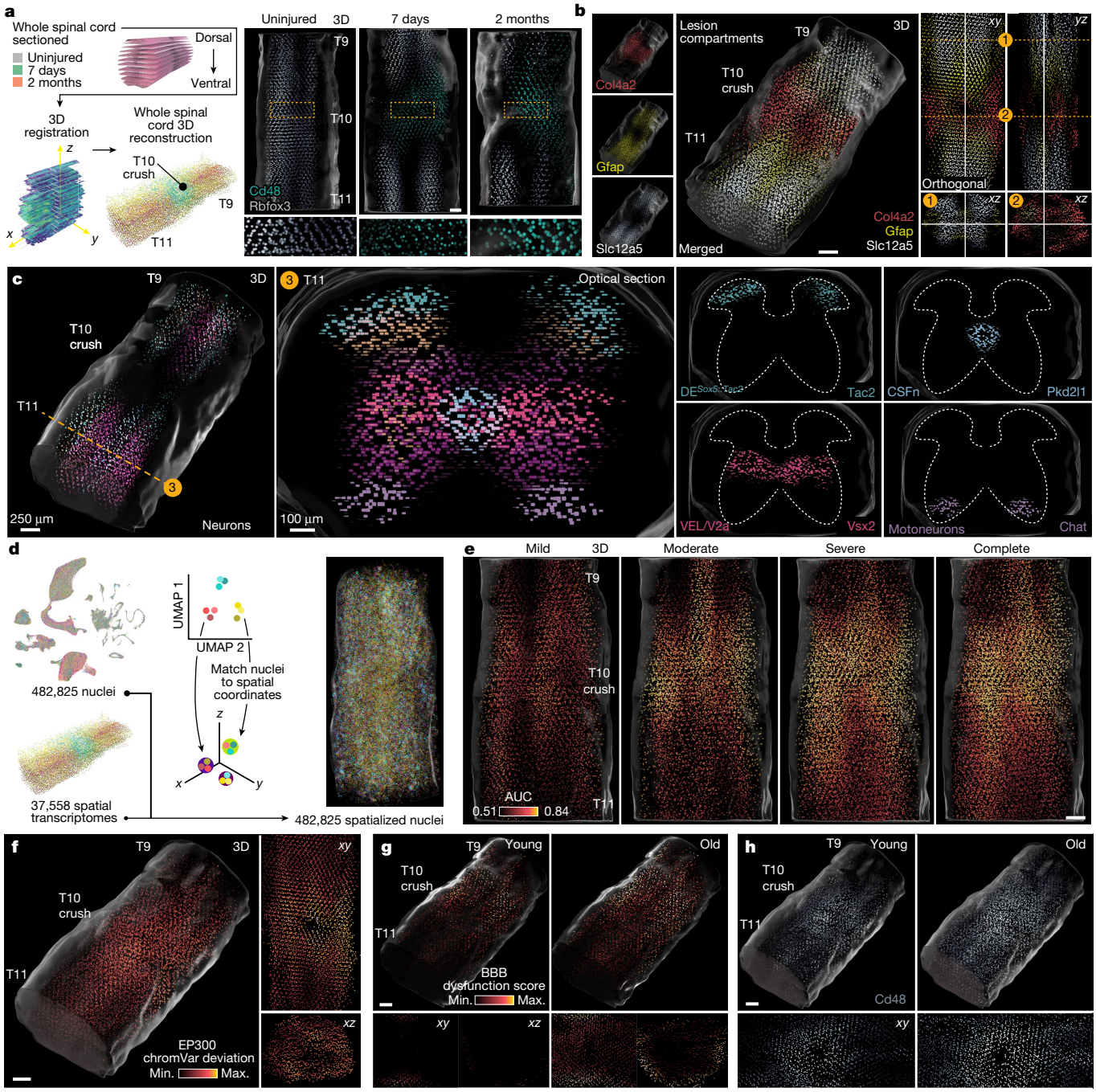

Fig. 7 | A 4D spatiotemporal atlas of SCI. a, Left, schematic overview of the 3D spatial transcriptomic atlas. Right, expression of marker genes for neurons (*Rbfox3*) and immune cells (*Cd48*) across three dimensions in the uninjured and injured mouse spinal cord. Scale bar, 200 µm. **b**, Expression of marker genes associated with distinct lesion compartments across the 3D spatial transcriptomic atlas at 7 days, including the fibrotic scar (*Col4a2*), the astrocyte barrier (*Gfap*) and the surrounding spared but reactive neural tissue (*Slc12a5*). Scale bar, 250 µm. **c**, Spatial localization of selected neuronal subpopulations defined by snRNA-seq across the 3D spatial transcriptomic atlas at 7 days. **d**, Left, UMAP representation of 435,099 single-nucleus transcriptomes from the snRNA-seq atlases, coloured by experimental condition. Right, spatial coordinates assigned to each single-nucleus transcriptome within the 3D spatial transcriptomic atlas. **e**, 3D spatial prioritization of spatialized cells from the snRNA-seq atlas, across injury severities. Scale bar, 250 µm. **f**, Accessibility of the EP300 binding motif within spatialized cells from the multiome atlas at 7 days, visualized on the 3D spatial transcriptomic atlas. Scale bar, 250 µm. **g**, Expression of the BBB dysfunction module in vascular cells from young and old mice at 7 days, visualized on the 3D spatial transcriptomic atlas. Scale bar, 250 µm. **h**, Expression of *Cd48* in spatialized cells from young and old mice at 7 days, visualized on the 3D spatial transcriptomic atlas. Scale bar, 250 µm.

to provide an unprecedented window into the genome-wide molecular cascade that unfolds after an injury to the spinal cord—from epigenetic regulation, to transcriptional programs within individual cells, to spatially and temporally dependent multicellular responses—that we overlaid onto a 4D model of the spinal cord. In Supplementary Note 6, we discuss the implications of the *Tabulae Paralytica* for the field of SCI.

The *Tabulae Paralytica* embody a number of technological and conceptual advances that demonstrate how genome-wide single-cell and spatial technologies can deliver new insights into uninjured and

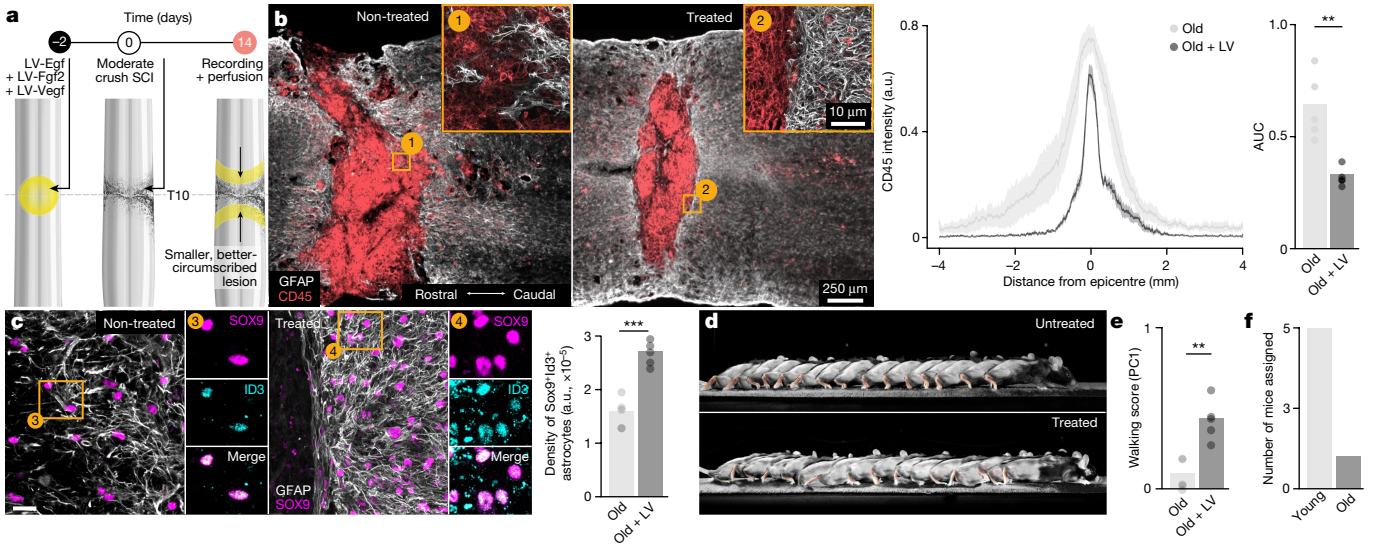

Fig. 8 | A rejuvenative gene therapy re-establishes the tripartite barrier to restore walking. a, Experimental design of a gene therapy intervention to promote the formation of the tripartite barrier. **b**, Composite tiled scans of GFAP and CD45 in horizontal sections from representative old and treated mice. Line graph demonstrates CD45 intensity at specific distances rostral and caudal to lesion centres. Bar graph shows the AUC (independent samples two-tailed *t*-test; $n = 5$ per group; $t = 4.57$; $P = 0.002$). **c**, Horizontal sections from representative old and treated mice identifying a restoration of $Sox9^{ON}Id3^{ON}$ cells in the astrocyte border region in treated mice. Scale bar, 10 µm. Right, bar graph indicates the density of $Sox9^{ON}Id3^{ON}$ cells in the astrocyte border region (independent samples two-tailed *t*-test; $n = 5$ per group; $t = 6.84$; $P = 0.0002$). **d**, Chronophotography of walking in old mice without (top) and with (bottom) a gene therapy intervention to promote the formation of the tripartite barrier. **e**, Walking performance of old mice with and without treatment (independent samples two-tailed *t*-test; $n = 5$ per group; $t = 4.85$; $P = 0.001$). **f**, Experimental conditions assigned to old mice that received gene therapy by a machine-learning model trained on kinematics data from untreated animals. Mice were predominantly assigned to the young mouse group, indicating that the walking patterns of treated old mice most resemble those of young mice.

perturbed tissues. On a conceptual level, we demonstrate how the increasing scale of single-cell technologies enables a comprehensive interrogation of the experimental manipulations relevant to any given disease within a single study. On a technical level, we establish the possibility of extending spatial transcriptomics into three and even four spatial and temporal dimensions within a common coordinate framework. Moreover, we show that the integration of multiomic single-cell atlases allows us to overlay patterns of chromatin accessibility onto a 4D spatial model. Finally, our findings illustrate the power of cell type and spatial prioritization, as implemented by Augur and Magellan, to resolve the molecular basis of diseases or biological perturbations using single-cell and spatial genomics.

The *Tabulae Paralytica*, or 'atlases of spinal cord injury', will serve as (1) a foundational resource to understand the pathobiology of SCI; (2) a reference of cellular and molecular responses to predict and interrogate the consequences of new therapeutic strategies; (3) a conceptual and technical framework to advance spatially resolved single-cell studies of disease and biological perturbations and (4) a translational resource to uncover new biological mechanisms of SCI that can be exploited to develop therapies to repair the injured spinal cord.

Online content

Any methods, additional references, Nature Portfolio reporting summaries, source data, extended data, supplementary information, acknowledgements, peer review information; details of author contributions and competing interests; and statements of data and code availability are available at https://doi.org/10.1038/s41586-024-07504-y.

1. Sofroniew, M. V. Dissecting spinal cord regeneration. *Nature* **557**, 343–350 (2018).
2. Anderson, M. A. et al. Natural and targeted circuit reorganization after spinal cord injury. *Nature Neurosci.* **25**, 1584–1596 (2022).
3. Courtine, G. & Sofroniew, M. V. Spinal cord repair: advances in biology and technology. *Nat. Med.* **25**, 898–908 (2019).
4. Ahuja, C. S. et al. Traumatic spinal cord injury. *Nat. Rev. Dis. Primers* **3**, 17018 (2017).
5. Rowald, A. et al. Activity-dependent spinal cord neuromodulation rapidly restores trunk and leg motor functions after complete paralysis. *Nat. Med.* **28**, 260–271 (2022).
6. Squair, J. W. et al. Neuroprosthetic baroreflex controls haemodynamics after spinal cord injury. *Nature* **590**, 308–314 (2021).
7. Wagner, F. B. et al. Targeted neurotechnology restores walking in humans with spinal cord injury. *Nature* **563**, 65–71 (2018).
8. Kathe, C. et al. The neurons that restore walking after paralysis. *Nature* **611**, 540–547 (2022).
9. Popovich, P. G., Wei, P. & Stokes, B. T. Cellular inflammatory response after spinal cord injury in Sprague-Dawley and Lewis rats. *J. Comp. Neurol.* **377**, 443–464 (1997).
10. Anderson, M. A. et al. Astrocyte scar formation aids central nervous system axon regeneration. *Nature* **532**, 195–200 (2016).
11. Squair, J. W., Gautier, M., Sofroniew, M. V., Courtine, G. & Anderson, M. A. Engineering spinal cord repair. *Curr. Opin. Biotech.* **72**, 48–53 (2021).
12. Asboth, L. et al. Cortico-reticulo-spinal circuit reorganization enables functional recovery after severe spinal cord contusion. *Nat. Neurosci.* **21**, 576–588 (2018).
13. Scheff, S. W., Rabchevsky, A. G., Fugaccia, I., Main, J. A. & Lumpp, J. E. Experimental modeling of spinal cord injury: characterization of a force-defined injury device. *J. Neurotraum.* **20**, 179–193 (2003).
14. Dusart, I. & Schwab, M. E. Secondary cell death and the inflammatory reaction after dorsal hemisection of the rat spinal cord. *Eur. J. Neurosci.* **6**, 712–724 (1994).
15. Zappia, L. & Oshlack, A. Clustering trees: a visualization for evaluating clusterings at multiple resolutions. *Gigascience* **7**, giy083 (2018).
16. Milich, L. M. et al. Single-cell analysis of the cellular heterogeneity and interactions in the injured mouse spinal cord. *J. Exp. Med.* **218**, e20210040 (2021).
17. Sofroniew, M. V. & Vinters, H. V. Astrocytes: biology and pathology. *Acta Neuropathol.* **119**, 7–35 (2010).
18. Faulkner, J. R. et al. Reactive astrocytes protect tissue and preserve function after spinal cord injury. *J. Neurosci.* **24**, 2143–2155 (2004).
19. Herrmann, J. E. et al. STAT3 is a critical regulator of astrogliosis and scar formation after spinal cord injury. *J. Neurosci.* **28**, 7231–7243 (2008).
20. Wanner, I. B. et al. Glial scar borders are formed by newly proliferated, elongated astrocytes that interact to corral inflammatory and fibrotic cells via STAT3-dependent mechanisms after spinal cord injury. *J. Neurosci.* **33**, 12870–12886 (2013).
21. Zheng, S. C. et al. Universal prediction of cell-cycle position using transfer learning. *Genome Biol.* **23**, 41 (2022).
22. Munji, R. N. et al. Profiling the mouse brain endothelial transcriptome in health and disease models reveals a core blood–brain barrier dysfunction module. *Nat. Neurosci.* **22**, 1892–1902 (2019).
23. Zeisel, A. et al. Molecular architecture of the mouse nervous system. *Cell* **174**, 999–1014.e22 (2018).
24. Yasuda, K. et al. Drug transporters on arachnoid barrier cells contribute to the blood–cerebrospinal fluid barrier. *Drug Metab. Dispos.* **41**, 923–931 (2013).
25. Dewar, D., Underhill, S. M. & Goldberg, M. P. Oligodendrocytes and ischemic brain injury. *J. Cereb. Blood Flow Metabol.* **23**, 263–274 (2002).

26. Petracca, Y. L. et al. The late and dual origin of cerebrospinal fluid-contacting neurons in the mouse spinal cord. *Development* **143**, 880–891 (2016).
27. Vígh, B. et al. The system of cerebrospinal fluid-contacting neurons. Its supposed role in the nonsynaptic signal transmission of the brain. *Histol. Histopathol.* **19**, 607–628 (2004).
28. Squair, J. W. et al. Recovery of walking after paralysis by regenerating characterized neurons to their natural target region. *Science* **381**, 1338–1345 (2023).
29. Courtine, G. et al. Recovery of supraspinal control of stepping via indirect propriospinal relay connections after spinal cord injury. *Nat. Med.* **14**, 69–74 (2008).
30. Skinnider, M. A. et al. Cell type prioritization in single-cell data. *Nat. Biotechnol.* **39**, 30–34 (2021).
31. Squair, J. W., Skinnider, M. A., Gautier, M., Foster, L. J. & Courtine, G. Prioritization of cell types responsive to biological perturbations in single-cell data with Augur. *Nat. Protoc.* **16**, 3836–3873 (2021).
32. Renthal, W. et al. Transcriptional reprogramming of distinct peripheral sensory neuron subtypes after axonal injury. *Neuron* **108**, 128–144.e9 (2020).
33. Nguyen, M. Q., Pichon, C. E. L. & Ryba, N. Stereotyped transcriptomic transformation of somatosensory neurons in response to injury. *eLife* **8**, e49679 (2019).
34. Cajal, S. R. Y. & May, R. M. *Cajal's Degeneration and Regeneration of the Nervous System* (Oxford Univ. Press, 1991).
35. Sperry, R. W. Chemoaffinity in the orderly growth of nerve fiber patterns and connections. *Proc. Natl Acad. Sci. USA* **50**, 703–710 (1963).
36. Cajal, S. R. Y. *Degeneration and Regeneration of the Nervous System* (Oxford Univ. Press, 1928).
37. Anderson, M. A. et al. Required growth facilitators propel axon regeneration across complete spinal cord injury. *Nature* **561**, 396–400 (2018).
38. Harel, N. Y. & Strittmatter, S. M. Can regenerating axons recapitulate developmental guidance during recovery from spinal cord injury?. *Nat. Rev. Neurosci.* **7**, 603–616 (2006).
39. Mironova, Y. A. & Giger, R. J. Where no synapses go: gatekeepers of circuit remodeling and synaptic strength. *Trends Neurosci.* **36**, 363–373 (2013).
40. Lin, A. C. & Holt, C. E. Local translation and directional steering in axons. *EMBO J.* **26**, 3729–3736 (2007).
41. Short, D., Masry, W. E. & Jones, P. High dose methylprednisolone in the management of acute spinal cord injury–a systematic review from a clinical perspective. *Spinal Cord* **38**, 273–286 (2000).
42. Bracken, M. B. Efficacy of methylprednisolone in acute spinal cord injury. *JAMA* **251**, 45 (1984).
43. Hurlbert, R. J. Methylprednisolone for acute spinal cord injury: an inappropriate standard of care. *J. Neurosurg. Spine* **93**, 1–7 (2000).
44. Klein, S. L. & Flanagan, K. L. Sex differences in immune responses. *Nat. Rev. Immunol.* **16**, 626–638 (2016).
45. Gal-Oz, S. T. et al. ImmGen report: sexual dimorphism in the immune system transcriptome. *Nat. Commun.* **10**, 4295 (2019).
46. Mattucci, S. et al. Basic biomechanics of spinal cord injury—how injuries happen in people and how animal models have informed our understanding. *Clin. Biomech.* **64**, 58–68 (2018).
47. O'Shea, T. M. et al. Lesion environments direct transplanted neural progenitors towards a wound repair astroglial phenotype in mice. *Nat. Commun.* **13**, 5702 (2022).
48. Squair, J. W. et al. Confronting false discoveries in single-cell differential expression. *Nat. Commun.* **12**, 5692 (2021).
49. Granja, J. M. et al. ArchR is a scalable software package for integrative single-cell chromatin accessibility analysis. *Nat. Genet.* **53**, 403–411 (2021).
50. Kang, J. B. et al. Efficient and precise single-cell reference atlas mapping with Symphony. *Nat. Commun.* **12**, 5890 (2021).
51. Schep, A. N., Wu, B., Buenrostro, J. D. & Greenleaf, W. J. chromVAR: inferring transcription-factor-associated accessibility from single-cell epigenomic data. *Nat. Methods* **14**, 975–978 (2017).
52. Schwarzschild, M. A., Cole, R. L. & Hyman, S. E. Glutamate, but not dopamine, stimulates stress-activated protein kinase and AP-1-mediated transcription in striatal neurons. *J. Neurosci.* **17**, 3455–3466 (1997).
53. Burda, J. E. et al. Divergent transcriptional regulation of astrocyte reactivity across disorders. *Nature* **606**, 557–564 (2022).
54. Pollard, K. S., Hubisz, M. J., Rosenbloom, K. R. & Siepel, A. Detection of nonneutral substitution rates on mammalian phylogenies. *Genome Res.* **20**, 110–121 (2010).
55. Christian, C. A. et al. Endogenous positive allosteric modulation of GABAA receptors by diazepam binding inhibitor. *Neuron* **78**, 1063–1074 (2013).
56. Chung, K. & Deisseroth, K. CLARITY for mapping the nervous system. *Nat. Methods* **10**, 508–513 (2013).
57. Olsson, A.-K., Dimberg, A., Kreuger, J. & Claesson-Welsh, L. VEGF receptor signalling? in control of vascular function. *Nat. Rev. Mol. Cell Bio.* **7**, 359–371 (2006).
58. Li, Y. et al. Microglia-organized scar-free spinal cord repair in neonatal mice. *Nature* **587**, 613–618 (2020).
59. Li, C. et al. Temporal and spatial cellular and molecular pathological alterations with single-cell resolution in the adult spinal cord after injury. *Signal Transduct. Target Ther.* **7**, 65 (2022).

Publisher's note Springer Nature remains neutral with regard to jurisdictional claims in published maps and institutional affiliations.

Springer Nature or its licensor (e.g. a society or other partner) holds exclusive rights to this article under a publishing agreement with the author(s) or other rightsholder(s); author self-archiving of the accepted manuscript version of this article is solely governed by the terms of such publishing agreement and applicable law.

© The Author(s), under exclusive licence to Springer Nature Limited 2024

Methods

Mouse model and experimental conditions

Adult male or female C57BL/6 mice (15–25 g body weight, 8–15 weeks of age) or transgenic mice were used for all experiments. Aged mice were purchased from JAX at 60 weeks of age (stock no. 000664). Vsx2^{Cre} (MMMRRC 36672, also called Chx10^{Cre}) transgenic mouse strain was bred and maintained on a mixed genetic background (C57BL/6). Housing, surgery, behavioural experiments and euthanasia were all performed in compliance with the Swiss Veterinary Law guidelines. Manual bladder voiding and all other animal care was performed twice daily throughout the entire experiment. All procedures and surgeries were approved by the Veterinary Office of the Canton of Geneva (Switzerland; authorizations GE/145/2).

A crush injury was selected as the primary injury model because, in our hands, this model produces more homogeneous functional deficits[10,37]. Spinal cord crushes were performed as previously described[10,37]. For time-course experiments, animals were euthanized at 1 day, 4 days, 7 days, 14 days, 1 month or 2 months postinjury. Crush injuries were performed at several severities by including spacers within No. 5 Dumont forceps (Fine Science Tools) such that, when closed, there was a maximal distance of 1, 0.5, 0.25 or 0 mm (no spacer) with a tip width of 0.5 mm. Dorsal hemisection SCIs were performed as previously described[14]. For dorsal hemisection SCI, a laminectomy was made at the mid-thoracic level (T10) and the dorsal half of the spinal cord was cut using a microscapel. Contusion SCIs were performed as previously described[8,12].

Minocycline was administered with intraperitoneal injections as previously described[60–62], with a loading dose of 50 mg kg^{-1} at 1 and 24 h postinjury, followed by maintenance doses of 25 mg kg^{-1} every 24 h for the next 5 days. Methylprednisolone was administered intramuscularly as previously described[63], with a loading dose of 60 mg kg^{-1} at 1 h postinjury then an extra 30 mg kg^{-1} dose every 6 h for 24 h. ChABC was delivered by means of lentiviral injections as previously described[64]. In brief, the *Proteus vulgaris* ChABC gene was previously modified to make a mammalian-compatible engineered ChABC gene[65]. The modified ChABC complementary DNA (cDNA) was subcloned into a lentiviral transfer vector (termed LV-ChABC) with the mouse phosphoglycerate kinase promoter[66]. The final viral titre was 479 μg ml^{-1} of P24, corresponding to roughly 10^6 TU μl^{-1}. A control lentiviral vector (termed LV-GFP) was generated from the same transfer vector containing the cDNA coding for green fluorescent protein, with a viral titre of 346 μg ml^{-1} of P24.

Viral vectors and vector production

Viruses used in this study were either acquired commercially or produced at the EPFL core facility. The following adeno-associated virus (AAV) plasmids were used and detailed sequence information is available as detailed or on request: AAV-CAG-flex-human Diphtheria Toxin Receptor (DTR) (plasmid gift from S. Arber), and produced as AAV5 at the EPFL Bertarelli Foundation Platform in Gene Therapy and SIN-cPPT-PGK-FGF2-WPRE, SIN-cPPT-PGK-EGF-WPRE SIN-cPPT-PGK-VEGF-WPRE, SIN-cPPT-GFAP-GDNF-WPRE and LV-PGK-ChABC (gift from E. Bradbury). Injection volumes, coordinates and experimental designs are described below.

Biological repair intervention in ageing mice

General surgical procedures have been previously described in detail[10,12,37]. Surgeries were performed at EPFL under aseptic conditions and under 1–2% isoflurane in 0.5–1 l min^{-1} flow of oxygen as general anaesthesia, using an operating microscope (Zeiss) and rodent stereotaxic apparatus (David Kopf) as previously described[12,37]. Lentiviral injections were made 2 days before SCI to allow time for expression, and were targeted over the intended spinal cord segment to be injured. Lentivirals were injected into four sites (two sets of bilateral injections, 0.30 μl per injection (all vectors diluted to 600 μg P24 per millilitre in sterile saline)) 0.6 mm below the surface at 0.15 μl min^{-1} using glass micropipettes connected through high-pressure tubing (Kopf) to 10 μl syringes under the control of a microinfusion pump. Moderate crush SCIs were introduced at the level of T10/T11 after laminectomy of a single vertebra by using No. 5 Dumont forceps (Fine Science Tools) with a spacer so that when closed a 0.5 mm space remained, and with a tip width of 0.5 mm to completely compress the entire spinal cord laterally from both sides for 5 s. After surgeries, mice were allowed to wake up in an incubator. Analgesia, buprenorphine (Essex Chemie AG, 0.01–0.05 mg kg^{-1} subcutaneously (s.c.)) or carprofen (5 mg kg^{-1} s.c.), was given twice daily for 2–3 days after surgery. Animals were randomly assigned numbers and thereafter were evaluated blind to experimental conditions. Fourteen days after SCI, all mice were evaluated in an open field and all animals showing any hindlimb movements were not studied further.

Neuron subpopulation-specific ablation

For ablation experiments with diphtheria toxin, Vsx2^{Cre} mice were subjected to crush SCI as described above. Three sets of bilateral injections of AAV5-CAG-FLEX-DTR (ref. 67) were made over the T9, T10 and T11 spinal segments (0.25 μl per injection) at a depth of 0.6 mm below the dorsal surface and separated by 1 mm. Two weeks after spinal infusions, mice received intraperitoneal injections of diphtheria toxin (Sigma, D0564) diluted in saline (100 μg kg^{-1}) to ablate Vsx2 neurons. Kinematics were evaluated in all mice before ablation, 2 weeks postablation and again after SCI.

Behavioural assessments

Behavioural procedures have been previously described in detail[12,68,69]. In brief, during overground walking, bilateral leg kinematics were captured with 12 infrared cameras of a Vicon Motion Systems that tracked reflective markers attached to the crest, hip, knee, ankle joints and distal toes. The limbs were modelled as an interconnected chain of segments and a total of 80 gait parameters were calculated from the recordings. To evaluate differences between experimental conditions, as well as to identify the most relevant parameters to account for these differences, we implemented a multistep multifactorial analysis based on principal component analysis, as previously described in detail[12,68,69], and coupled to automated, markless tracking software[70]. In brief, reconstructed kinematic data were processed with custom MATLAB scripts to compute gait parameters. For each experiment, a principal component analysis was performed by computing the covariance matrix A of the ensemble of parameters over the gait cycle, after subtraction of their respective mean values. The principal components were computed from eigenvalues λ_j and eigenvectors $\mathbf{U}_j$ of A. The principal components were ordered according to the amount of data variance accounted for by each component. The coordinate of each gait cycle on the first principal component, that is, the component vector explaining the greatest amount of variance across the gait parameters was thereafter referred to as the walking score. These scores were subsequently normalized for each experiment. Individual parameters were then selected to be compared between groups on the basis of their correlation to the first principal component.

Perfusions

Mice were perfused at the end of the experiments. Mice were deeply anaesthetized by an intraperitoneal injection of 0.2 ml of sodium pentobarbital (50 mg ml^{-1}). Mice were transcardially perfused with PBS followed by 4% paraformaldehyde in PBS. Tissue was removed and postfixed overnight in 4% paraformaldehyde before being transferred to PBS or cryoprotected in 30% sucrose in PBS.

Immunohistochemistry

Immunohistochemistry was performed as previously described[10,12,37]. Perfused postmortem tissue was cryoprotected in 30% sucrose in PBS

for 48 h before being embedded in cryomatrix (Tissue Tek OCT, Sakura Finetek Europe B.V.) and freezing. Next, 30 µm thick transverse or horizontal sections of the spinal cord were cut on a cryostat (Leica), immediately mounted on glass slides and dried or in free floating wells containing PBS plus 0.03% sodium azide. Primary antibodies were: rabbit anti-GFAP (glial fibrillary acidic protein) (1:1,000; Dako); mouse anti-GFAP (1:1,000; Cell Signalling Technology), rat anti-GFAP (1:1,000; ThermoFisher Scientific); rabbit anti-albumin (1:250; Abcam); rabbit anti-Chat (1:200; Millipore); guinea pig anti-NeuN (1:300; Millipore); chicken anti-RFP (1:500, Novus Biologicals); rabbit anti-Chx10 (also known as Vsx2) (1:500, Novus Biologicals); rat anti-CD45 (1:100, BD Biosciences); goat anti-Sox9 (1:200, Novus Biologicals); rabbit anti-Id3 (1:500; Cell Signaling Technology); rabbit anti-PKD1L2 (1:1,000; Merck Millipore). Fluorescent secondary antibodies were conjugated to Alexa 488 (green), Alexa 405 (blue), Alexa 555 (red) or Alexa 647 (far red) (ThermoFisher Scientific). The nuclear stain was 4′,6′-diamidino-2-phenylindole dihydrochloride (DAPI; 2 ng ml^{-1}; Molecular Probes). Sections were imaged digitally using a slide scanner (Olympus VS-120 Slide scanner) or confocal microscope (Zeiss LSM880 + Airy fast module with ZEN 2 Black software). Images were digitally processed using ImageJ (ImageJ, NIH) software or Imaris (Bitplane, v.9.0.0).

Fluorescence in situ hybridization

To validate the spatial gene expression patterns after SCI that emerged from spatial transcriptomics analyses, we performed in situ hybridization of the relevant messenger RNA molecules using RNAscope (Advanced Cell Diagnostics). Target genes were obtained from spatial transcriptomics data by performing spatial prioritization with Magellan, and the results were cross-referenced against a list of validated probes designed and provided by Advanced Cell Diagnostics. Probes were obtained for the following genes: *Col1a1*, catalogue no. 319371; *Plin2*, catalogue no. 577111; *Tmsb4x*, catalogue no. 472851. We then generated 12 µm cryosections from fixed-frozen spinal cords as previously described and performed fluorescence in situ hybridization for each probe according to the manufacturer's instructions, using the RNAscope Fluorescent Multiplex Reagent Kit (catalogue no. 323133).

Tissue clearing (CLARITY)

Samples were incubated in X-CLARITY[12,71,72] hydrogel solution (Logos Biosystems Inc.) for 24 h at 4 °C with gentle shaking. Samples were then degassed and polymerized using the X-CLARITY Polymerisation System (Logos Biosystems), followed by washes in 0.001 M PBS for 5 min at room temperature. Samples were next placed in the X-CLARITY Tissue Clearing System (Logos Biosystems), set to 1.5 A, 100 rpm, 37 °C, for 29 h. Clearing solution was made in-house with 4% SDS, 200 mM boric acid with dH_2O, pH adjusted to 8.5. Following this, samples were washed for at least 24 h at room temperature with gentle shaking in 0.1 M PBS solution containing 0.1% Triton X-100 to remove excess SDS. Finally, samples were incubated in 40 g of Histodenz dissolved in 30 ml of 0.02 M PB, pH 7.5, 0.01% sodium azide (refractive index 1.465) for at least 24 h at room temperature with gentle shaking before imaging.

3D imaging

Imaging of cleared tissue was performed using a customized mesoSPIM[73] and CLARITY-optimized light-sheet microscope (COLM)[72]. A custom-built sample holder was used to secure the CNS in a chamber filled with refractive index matching solution. Samples were imaged using either a 1.25× or 2.5× objective at the mesoSPIM[73] and a 4× or 10× objective at the COLM[72] with one or two light sheets illuminating the sample from both the left and right sides. The voxel resolution in the *x*, *y* and *z* directions was 5.3 × 5.3 × 5 µm for the ×1.25 acquisition and 2.6 × 2.6 × 3 µm for the 2.5× acquisition. The voxel resolution of the COLM was 1.4 × 1.4 µm by 5 µm. Images were generated as 16 bit TIFF files and then stitched using Arivis Vision4D (Arivis AG). 3D reconstructions and optical sections of raw images were generated using Imaris (Bitplane, v.9.0.0) software.

Histological analysis

To quantify immune invasion after different models of SCI, we measured the percentage of CD45 immunopositive area after binarizing the fluorescent signal using the image analysis software Fiji. To quantify BSCB dysfunction and immune invasion in young and old mice, we measured immunopositive areas for albumin and CD45, respectively, after binarizing the fluorescent signal using the image analysis software Fiji. To assess the formation of astrocyte scar borders after SCI in young and old mice, we counted the number of Sox9^{ON} cells using the image analysis software QuPath and the cell detection functionality with default settings (v.0.4.3). We then classified Sox9^{ON} cells as either Id3^{ON} or Id3^{OFF} by setting a mean signal intensity threshold. We used the same approach to count the number of NeuN^{ON} and PKD1L2^{ON} neurons, to assess the resilience of CSF-contacting neurons after SCI. To quantify the number of Vsx2^{ON} neurons after neuronal subpopulation-specific ablation with DTR we used the image analysis software Imaris (Bitplane, v.9.0.0).

Chronophotography

Chronophotography was used to generate a representative series of still pictures arranged in a single photograph to illustrate the locomotor abilities of mice. Videos at 25 fps or photographs at 15 fps were recorded while mice were performing locomotor tasks such as quadrupedal walking on the runway. Images from these recordings were chosen to best illustrate the different consecutive phases of walking of the hindlimbs, that is, stance phases and swing phases. The frequency of chosen pictures varied due to the varying velocity of the mice. The series of pictures were assembled in Photoshop while blending out non-essential details.

snRNA-seq library preparation

Single-nucleus dissociation of the mouse lumbar spinal cord was performed according to our established procedures[30,48]. Following euthanasia by isoflurane inhalation and cervical dislocation, the lumbar spinal cord site was immediately dissected and frozen on dry ice. We dounced spinal cords in 250 µl of sucrose buffer (0.32 M sucrose, 10 mM HEPES (pH 8.0), 5 mM $CaCl_2$, 3 mM Mg acetate, 0.1 mM EDTA, 1 mM dithiothreitol (DTT)) and 0.1% Triton X-100 with the Kontes Dounce Tissue Grinder. Then, 1.1 ml of sucrose buffer was added and filtered through a 40 µm cell strainer. The lysate was centrifuged at 3,200*g* for 5 min at 4 °C. The supernatant was decanted, and 1 ml of sucrose buffer added to the pellet and incubated for 1 min. The pellet was homogenized using an Ultra-Turrax and 3 ml of density buffer (1 M sucrose, 10 mM HEPES (pH 8.0), 3 mM Mg acetate, 1 mM DTT) was added below the nuclei layer. The tube was centrifuged at 3,200*g* at 4 °C for 10 min and supernatant was immediately poured off. Nuclei on the bottom half of the tube wall were resuspended in 100 µl of PBS with 1% bovine serum albumin for subsequent snRNA-seq or in 10X Nuclei Buffer (catalogue no. 2000153, 10X Genomics) for subsequent single-nucleus multiome sequencing. Resuspended nuclei were filtered through a 30 µm strainer, and adjusted to 1,000 nuclei per microlitre. We carried out snRNA-seq library preparation using the 10X Genomics Chromium Single Cell Gene Expression Kit v.3.1. The nuclei suspension was added to the Chromium RT mix to achieve loading numbers of 10,000 nuclei. For downstream cDNA synthesis, library preparation and sequencing, the manufacturer's instructions were followed.

Multiome sequencing library preparation

We carried out snRNA and ATAC library preparation using the 10X Genomics Chromium Single Cell Multiome ATAC + Gene Expression Kit. First, the transposition mix was added to the resuspended nuclei followed by 60 min of incubation at 37 °C. The transposed nuclei were added to the Chromium RT mix to achieve loading numbers of 10,000

nuclei. The manufacturer's instructions were followed for downstream cDNA synthesis, library construction, indexing and sequencing.

Spatial transcriptomics library preparation

We carried out two separate experiments to study the cytoarchitecture of the lesion microenvironment after SCI. First, we prepared sections from uninjured mice, 7 days and 2 months after crush SCI (performed with a 0.5 mm spacer as described above). For each experimental condition, we prepared sections from the lesion epicentre of three independent biological replicates. Second, to prepare our 4D spatiotemporal atlas, we collected sections throughout the entire spinal cord of mice from each of the three experimental conditions. The SCI sites of mice were embedded in optimal cutting temperature compound and cryosections were generated at 10 µm at −20 °C. For the 4D atlas, every fifth section was collected throughout the entire dorsoventral axis of each spinal cord. Sections were immediately placed on chilled Visium Tissue Optimization Slides (catalogue no. 1000193, 10X Genomics) or Visium Spatial Gene Expression Slides (catalogue no. 1000184, 10X Genomics). Tissue sections were then fixed in chilled methanol and stained according to the Visium Spatial Gene Expression User Guide (catalogue no. CG000239 Rev A, 10X Genomics) or Visium Spatial Tissue Optimization User Guide (catalogue no. CG000238 Rev A, 10X Genomics). For gene expression samples, tissue was permeabilized for 12 min, which was selected as the optimal time on the basis of tissue optimization time-course experiments. Brightfield histology images were taken using a ×10 objective on a slide scanner (Olympus VS-120 Slide scanner). For tissue optimization experiments, fluorescent images were taken with a TRITC (tetramethylrhodamine) filter using a ×10 objective and 400 ms exposure time. Libraries were prepared according to the Visium Spatial Gene Expression User Guide.

Read alignment

Following sequencing on our HiSeq4000 (EPFL Gene Expression Core Facility), snRNA-seq reads were aligned to the latest Ensembl release of the mouse genome (GRCm38.101), and a matrix of unique molecular identifier (UMI) counts was obtained using CellRanger (10X Genomics, v.4.0.0)[74]. For spatial transcriptomics, a spatial expression UMI count matrix was obtained using SpaceRanger (10X Genomics, v.1.0.0). For the multiome dataset, RNA-seq and ATAC-seq data were aligned to the reference genome using CellRanger-ARC (10X Genomics, v.2.0.0), and a matrix of UMI counts was obtained for the RNA modality. The ATAC modality was then processed further using ArchR, as described below.

snRNA-seq preprocessing and quality control

Droplet-based snRNA-seq experiments are known to be affected by ambient RNA contamination, whereby freely floating RNA molecules are encapsulated along with a cell or nucleus in a single droplet and spuriously attributed to the endogenous expression profile of the encapsulated cell[75]. The presence of ambient RNA is a potential source of batch effects and spurious DE. To mitigate this possibility, we used CellBender[76] to remove ambient RNA molecules and filter empty droplets. CellBender remove-background was run for 50 epochs with a learning rate of 5×10^{-5}. Corrected count matrices were then imported into Seurat[77] for further quality control. Quality control metrics included the number of UMIs per cell, the number of genes detectably expressed per cell and the proportion of UMI counts arising from mitochondrial genes. For the pilot dataset, cells with between 200 and 40,000 UMIs, and fewer than 7,500 genes expressed, were retained. For the snRNA-seq and multiome datasets, cells with at least 200 UMIs were retained. The proportion of mitochondrial counts was not used to perform cell-level quality control. Further quality control was performed for the multiome dataset on the basis of the ATAC modality, as described further below. Low-quality libraries were identified as those with distributions of number of UMIs, number of genes expressed or proportion of mitochondrial counts that differed markedly from the remainder of the libraries in the dataset, and a total of three low-quality libraries (two from the snRNA-seq dataset and one from the multiome dataset) were removed.

Putative doublets were then identified and filtered using a combination of approaches. We tested the performance of four computational methods for doublet detection in our pilot dataset, including DoubletFinder[78], scDblFinder[79], scds[79,80] and Scrublet[81]. On the basis of this analysis, we selected scDblFinder and scds as the two methods that (1) did not show an overt bias towards doublet detection for cells of any particular type, (2) that showed the highest agreement with one another and (3) that were also found to be among the top-performing methods in an independent benchmark[81]. We adopted a conservative approach by filtering barcodes from the union of those called doublets by either scDblFinder or scds in both the pilot and snRNA-seq datasets. For the multiome dataset, doublets were instead identified and filtered using ArchR, as described below.

Integration and cell-type annotation

Before clustering and cell-type annotation, we first performed batch effect correction and data integration across experimental conditions using Harmony[82]. Gene expression counts were normalized to counts per 10,000 and log transformed, and the top 2,000 variable genes were identified using the 'vst' method in Seurat. Gene expression values were then scaled and centred and provided as input to Harmony, which was run with 50 principal components. The integrated Harmony embeddings were then provided as input to *k* nearest neighbour graph construction and Leiden clustering using the default Seurat workflow[77], as in our previous studies[8,30,48]. Cell types were then manually annotated on the basis of marker gene expression, guided by previous studies of the mouse spinal cord[8,23,30,48,58,83–93] and other relevant cell atlases of major cell types[94,95]. Local and projecting neuronal subpopulations were annotated on the basis of *Nfib* and *Zfhx3* expression, respectively[83]. Astrocyte subtype annotations were validated through comparisons to white and grey matter astrocyte signatures reported in ref. 96, pan-reactive astrocyte signature reported by ref. 97 and cell-cycle signature genes from ref. 98, in each case using the Seurat function 'AddModuleScore'. Clusters corresponding to damaged cells or doublets that had survived initial quality control were removed at this stage. In the pilot dataset, we performed an initial round of clustering to identify coarse cell types with a resolution of 0.05, followed by subclustering of neurons (resolution 0.5) and glia (resolution 0.1) to annotate more fine-grained subtypes. In the snRNA-seq dataset, we repeated the clustering analysis for several values of the resolution parameter (0.01, 0.05, 0.2, 0.5, 2) to annotate cell types across several resolutions (for example, neurons → ventral neurons → ventral excitatory interneurons). We then used the clustree package[15] to link clusters across adjacent resolutions into a hierarchical clustering tree, as previously described[8,30,48].

Pilot dataset and meta-analysis of published spinal cord snRNA-seq datasets

We conducted an initial pilot experiment to confirm that our dissociation procedures enabled the recovery of all the cell types comprising the mouse spinal cord. snRNA-seq libraries were prepared from one uninjured mouse and one mouse 7 days after crush SCI, and deeply sequenced to a target depth of 100,000 reads per nucleus. After preprocessing and quality control as described above, we retained 9,170 nuclei from the injured sample and 9,099 nuclei from the uninjured sample. Following data integration and cell-type annotation as described above, we confirmed that we recovered the major cell types of the spinal cord in both the injured and uninjured spinal cords, and that changes in cell-type proportions across experimental conditions were concordant with the established pathophysiology of SCI. We then compared the cell-type proportions in our pilot dataset to those in 16 published single-cell datasets from the mouse spinal cord[16,23,30,58,59,83–93]. Automated cell-type annotation of published datasets was performed

using the label transfer workflow in Seurat, with our own previously published dataset from the uninjured lumbar spinal cord[30] used as the reference. We confirmed that the label transfer workflow yielded reliable predictions by comparing automated cell-type annotations to manual annotations from a published dataset[91]. This analysis established that our dissociation protocols allowed us to recover the major cell types of the spinal cord in proportions consistent with published snRNA-seq studies of the whole adult spinal cord. Finally, we took advantage of our deeply sequenced pilot dataset to calibrate our target sequencing depth of our main experiments, and selected a target depth of 75,000 reads per nucleus on the basis of downsampling analysis of the pilot dataset.

snRNA-seq atlas

For the snRNA-seq dataset, preprocessing, quality control, data integration and cell-type annotation were performed as described above, yielding a dataset comprising 435,099 nuclei from 52 mice spanning 18 experimental conditions. Two libraries were removed at the quality control stage, one from 7 days postinjury and one from male mice, because of low numbers of UMIs and genes per cell. Marker genes were identified for each cluster using the FindMarkers function in Seurat. We visualized the distribution of cell types, experimental conditions and the expression of marker genes with uniform manifold approximation and projection (UMAP) embeddings of both the entire dataset as well as each major cell type. Colour palettes were selected using the Palo R package to perform spatially aware colour palette optimization[99]. Marker gene dotplots were constructed using the DotPlot function in Seurat. Cell-type proportions were visualized using sunburst plots[100] and Sankey diagrams. The cell-cycle positions of astroependymal cells were estimated using tricycle[21], which provides a universal method for estimating progression through the phases of the cell cycle based on projection of cell-cycle gene expression onto embeddings defined by principal component analysis of a fixed reference dataset in which the cell cycle is the primary source of transcriptional variation. The output of tricycle is a cell-level continuous variable, θ, estimated as the polar angle around the origin for each cell, which takes on values between 0 and 2π. The authors of tricycle show that this angle captures structure in single-cell gene expression data that are not reflected in the discrete cell-cycle stages assigned by tools such as Seurat. To study the proportion of actively proliferating cells, astroependymal cells were discretized along θ into two bins corresponding to actively proliferating ($0.25\pi < \theta < 1.5\pi$; S/G2/M) or non-proliferating (G1/G0), as recommended by the authors of tricycle[21]. The expression of a previously described gene module[22] associated with BBB dysfunction was estimated using the Seurat function AddModuleScore. Unless otherwise stated, all cell subtype analyses were performed at level 5 of the clustering tree (corresponding to a resolution of 2).

Cell-type proportions

Testing for differences in cell-type proportions within single-cell data can lead to false discoveries because the data are compositional in nature and, consequently, increase the proportion of one cell type, which can cause an artefactual decrease in the proportions of every other cell type[101]. To avoid this pitfall, we used the propeller method[102], as implemented in the speckle R package, to test for differences in cell-type proportions between experimental conditions, as an independent benchmark showed this to be among the most accurate methods in balancing control of the false discovery rate with statistical power[103]. The details of individual cell-type proportion analyses are described below.

DE

To identify genes differentially expressed between experimental conditions, we performed DE analysis by aggregating expression from all cells of a given type within each replicate into a 'pseudobulk' profile, as previously described[48] and implemented in the Libra R package (https://github.com/neurorestore/Libra). In our previous work[48], we demonstrated that this approach allowed us to overcome false discoveries caused by variability between biological replicates[104]. We showed that widely used single-cell DE methods can conflate this variability with the effect of a biological perturbation, leading to hundreds or even thousands of false discoveries. We therefore instead used the likelihood ratio test implemented in edgeR[105] to identify DE genes between pseudobulks from each cell type. The details of individual DE analyses are described below.

GO enrichment analysis

GO term annotations for mouse were obtained from the GO Consortium website. GO terms annotated to fewer than five genes were excluded. The average expression level of genes associated with each GO term in individual cells was calculated using the Seurat function AddModuleScores, which controls for the average expression of randomly selected control features. Linear mixed models were then used to test for differences in GO module scores test across experimental conditions, using the 'lmerTest' R package to optimize the restricted maximum likelihood and obtain *P* values from the Satterthwaite approximation for degrees of freedom. The details of individual GO enrichment analyses are described below.

Cell-type prioritization

To identify cell types activated in response to each biological perturbation captured in the *Tabulae Paralytica*, we used a machine-learning method for cell-type prioritization that we previously developed, named Augur[8,30,31]. In brief, Augur seeks to rank cell types on the basis of the intensity of their transcriptional response to a biological perturbation. The key assumption underlying Augur is that cell types undergoing a profound response to a perturbation should become more separable, within the highly multidimensional space of gene expression, than less affected cell types. To quantify this separability, we framed this problem as a classification task. Augur first withholds a proportion of experimental condition labels, then trains a random forest classifier to predict the condition from which each cell was obtained (for instance, SCI or uninjured). The accuracy with which this prediction can be made from single-cell gene expression measurements is then evaluated in cross-validation, and quantified using the area under the receiver operating characteristic curve (AUC). This process is repeated separately for each cell type. The AUC then provides a quantitative measure of separability that can be used to rank cell types on the basis of the relative magnitude of their response to an arbitrary perturbation. We refer to this process as cell-type prioritization. Augur was run with default parameters directly on the UMI count matrix for all comparisons. To evaluate the robustness of cell-type prioritizations to the resolution at which neuronal subtypes were defined in the snRNA-seq data, we applied Augur at various clustering resolutions, and visualized the resulting cell-type prioritizations both on a hierarchical clustering tree[15] of cell types and as a progression of UMAPs[8]. The details of individual cell-type prioritization analyses are described below.

Conserved and divergent neuronal responses to SCI

To identify spinal cord neurons that were resilient or susceptible to SCI, we computed the $\log_2$ odds ratio between the uninjured spinal cord and each experimental condition in which the injured spinal cord was profiled at 7 days postinjury, using neuron subtypes defined at level 4 of the clustering tree (corresponding to a resolution of 0.5), then identified resilient or susceptible neuron subtypes using a *t*-test on $\log_2$ odds ratios. To identify DE genes specific to CSF-contacting neurons at the most acute phase of the injury response, we used edgeR to test for an interaction term between neuronal subtype and experimental condition at 1 day postinjury, using pseudobulk gene expression profiles.

To quantify the degree to which transcriptional responses to injury were conserved across neuron subtypes, we computed the Spearman correlation between log-fold changes estimated by edgeR between each pair of level 4 neuron subtypes. For genes that were not quantified in one of the two subtypes, missing log-fold change values were replaced with zeros.

To characterize the conserved early response of neurons to SCI, we first filtered to genes that were differentially expressed within individual level 4 neuron subtypes at a 10% false discovery rate. We then sorted these genes first by the number of neuron subtypes in which they were differentially expressed, and second by the mean absolute log-fold change estimated by edgeR. To delineate the time course with which this module of early-conserved genes was up- or downregulated in any given neuron subtype, we tested for differences in the average expression of a gene module comprising the top 25 early-conserved response genes (that is, the 25 genes that were upregulated in the greatest number of level 4 neuron subtypes and with the greatest mean log-fold change at 1 day postinjury) using a linear mixed model. Separately, we computed module scores for GO terms within each neuron with the Seurat function AddModuleScore, as described above, then tested for differences between injured and uninjured neurons using a linear mixed model.

To quantify the expression of transcriptional programs associated with projection growth and morphogenesis, we used the median expression of genes associated with the GO term GO:0031175 (neural projection development) to construct a circuit reorganization score, as described above. We then computed the basal expression of this circuit reorganization score as the median GO module score in the uninjured spinal cord for each level 4 neuron subtype. To quantify upregulation of the circuit reorganization score after injury, we subtracted the basal expression score from the GO module score at each time point postinjury to yield induced expression scores. We then calculated the Pearson correlation between basal and induced circuit reorganization scores. We carried out similar analyses for the GO terms GO:0061564 (axon development) and GO:0016358 (dendrite development).

Cell-type prioritization was performed by comparing neurons from each level 4 subtype at each time point postinjury to neurons from the uninjured spinal cord.

Neurons remain differentiated after CNS injury

Individual marker genes for each neuron subtype were manually curated from literature after cross-referencing with other atlases, as described above. DE analysis was performed by comparing neurons from each level 4 subtype at each time point postinjury to neurons from the uninjured spinal cord using edgeR as described above, with a 5% false discovery rate. We also constructed unbiased lists of the top n marker genes for each level 4 neuron subtype (for $n = 5, 10$ or 50) using the FindMarkers function in Seurat. We used the AddModuleScore function to summarize the average expression of the top n marker genes in each individual neuron, then used a linear mixed model to test for differences across experimental conditions as described above for GO enrichment analyses.

Facilitating and inhibiting molecule expression in the injured spinal cord

We visualized the expression of key facilitating and inhibiting molecules across the cell types and subtypes of the spinal cord using clustering trees, with the scaled mean expression for each cell type or subtype calculated as in the Seurat function DotPlot. To identify genes coordinately up- or downregulated across level 4 neuron subtypes in response to ChABC treatment, we used edgeR to perform DE analysis as described above and performed a one-sample t-test on log-fold change estimates from edgeR. We then used linear mixed models to perform GO enrichment analysis of ChABC treatment for each level 4 neuron subtype, as described above, and performed a one-sample t-test on coefficients estimated by the mixed models.

Cellular divergence between animal models of SCI

Cell-type proportions were compared using propeller, as described above, both for coarse cell types and for the most fine-grained subtypes of immune cells. Cell-type prioritization was performed by comparing neurons from each level 4 subtype between each pair of animal models (crush, contusion or hemisection). Separately, we tested for differences in the AUCs of dorsal and ventral level 4 neuron subtypes by comparing neurons from mild, moderate, severe or complete injuries to neurons from the uninjured spinal cord.

Immunomodulation does not confer neuroprotection after SCI

Cell-type prioritization was performed by comparing cell types at each resolution of the clustering tree from drug-treated and untreated but injured spinal cords. The proportions of coarse cell types were compared using propeller as described above.

To dissect more subtle transcriptional effects of neuroprotective agents on surviving neurons, we developed a machine-learning approach to identify neurons showing an uninjured transcriptional phenotype. For each experimental condition involving injured and untreated mice (that is, excluding the uninjured and drug-treated conditions), we trained a random forest model on scaled and log-normalized gene expression data to distinguish cells from that condition ('injured' cells) to cells from the uninjured spinal cord ('uninjured' cells). Separate models were trained for each level 4 neuron subtype. We validated the accuracy of these models in tenfold cross-validation, finding that for any given injury condition and neuron subtype, they achieved a median accuracy of 96% and a median AUC of 0.99 (Supplementary Fig. 13g). Moreover, we investigated the top-ranked genes according to feature importance, as quantified by the mean decrease in accuracy, and found that these tended to be differentially expressed across several neuron subtypes and a range of experimental comparisons (Supplementary Fig. 13h). We then applied each of these models in turn to neurons from the methylprednisolone and minocycline conditions, to predict whether they showed an injured or uninjured phenotype. The modal prediction across all models was then assigned to each neuron. To further characterize the transcriptional programs induced by neuroprotective agents, we then used linear mixed models to perform GO enrichment analysis of methylprednisolone or minocycline treatment for each level 4 neuron subtype, as described above, and performed a one-sample t-test on coefficients estimated by the mixed models.

Sexually dimorphic responses to SCI are subtle

Cell-type prioritization was performed by comparing cell types at each resolution of the clustering tree from male and female spinal cords. The range of AUC values assigned by Augur in cross-validation was then compared to that observed in other comparisons involving the injured spinal cord at 7 days postinjury. Cell-type proportions were compared using propeller, as described above, both for coarse cell types and for the most fine-grained subtypes of immune cells.

Failure of tripartite barrier formation in old mice

Cell-type prioritization was performed by comparing cell types at each resolution of the clustering tree from young and old mice, and the range of AUC values assigned by Augur in cross-validation was again compared to that observed in other comparisons involving the injured spinal cord at 7 days postinjury. The proportion of Id3-expressing astrocytes was compared between young and old mice using a χ^2 test. Gene modules associated with BBB endothelial cell identity and peripheral endothelial cell identity were obtained from the literature[22], and their expression in individual vascular cells was calculated using the Seurat function AddModuleScore.

DE analysis was performed as described above by comparing cells from young and old mice after SCI, for cell subtypes at level 4 of the

clustering tree (resolution 0.5) and with a false discovery rate of 5%. To quantify the heterogeneity of gene expression across cell types, we calculated two summary statistics. First, we defined the direction consistency as the proportion of cell types in which the sign of the log-fold change was the same as the modal sign. For example, if a gene was upregulated in eight of ten cell types and downregulated in the other two, the direction consistency would be 80%. Second, we defined the response heterogeneity as the standard deviation of the log-fold change across cell types.

snATAC-seq preprocessing and quality control

Preprocessing and quality control of the ATAC modality within our multiome dataset was carried out using CellRanger-ARC and ArchR[49]. Reads were mapped to the reference genome with CellRanger-ARC, and arrow files were created from the resulting fragment files. Nuclei were first filtered on the basis of the RNA modality as described above, and subsequently additional quality control was performed in ArchR. We initially ran ArchR with very lenient filtering to determine optimal quality control parameters (minimum transcription start site enrichment score 0, minimum fragments per cell 100), and selected optimal parameters on the basis of the joint distribution of these parameters. Arrow files were subsequently regenerated after filtering nuclei to those with a minimum transcription start site enrichment score of 4 and a minimum of 4,000 fragments per cell. Doublet detection and filtering was performed using the ArchR functions addDoubletScores and filterDoublets, both with default parameters. These steps afforded matrices of 40,526 nuclei that passed quality control in both the RNA and ATAC modalities.

To link cell types in the multiome dataset to the cellular taxonomy derived from our snRNA-seq atlas, we devised a hierarchical label transfer strategy using Symphony[50]. In brief, we first used Symphony to perform automated cell-type assignment in the multiome dataset at the highest level of the clustering tree (level 1, resolution 0.01). We then used Symphony to perform automated cell-type assignment at the second level of the clustering tree (resolution 0.05), considering only subtypes of the assigned coarse cell types as potential matches for each nucleus. This process was repeated iteratively for each level of the clustering tree. We validated the accuracy of this strategy using a leave-library-out cross-validation approach within the snRNA-seq atlas, in which entire libraries were withheld from the atlas and automated cell-type assignment was compared to the manual cell-type assignment derived from the entire dataset. We found that the hierarchical approach improved the accuracy of automated cell-type assignment relative to a non-hierarchical version of the same approach, in which all cell subtypes at any given level were considered as potential matches, particularly at more granular levels of the clustering tree. For cell-type assignment in the multiome dataset, we ran Symphony using the hierarchical approach with 100 soft cluster centroids, 100 principal components and 20 nearest neighbours, then made further manual adjustments to cell-type annotations for a handful of cell subtypes that showed discordant marker gene expression.

To further corroborate the accuracy of Symphony in cross-validation, we investigated the similarity in gene expression profiles of neuronal subpopulations between the snRNA-seq and multiome atlases. Pseudobulk gene expression profiles were constructed by summing gene-level counts across all neurons of a given level 4 subtype in either atlas, and then normalized using the variance-stabilizing transformation implemented in DESeq2 (ref. 106). Only neuron subtypes identified in both atlases were included, and genes that were quantified in only one of the two atlases were discarded. We then calculated the Euclidean distance between each pair of pseudobulk gene expression profiles in the snRNA-seq and multiome atlas, and scaled Euclidean distances per multiome subtype to zero mean and unit variance for visualization. This analysis showed that the closest neuronal subpopulation for each neuron subtype in the multiome atlas in gene expression space was its cognate subpopulation in the snRNA-seq atlas, validating the automated cell-type annotation approach.

Peak calling in the snATAC-seq dataset was then carried out using the default ArchR workflow, including peak calling with MACS2 (ref. 107) on pseudobulk replicates from each cell type, followed by peak merging across cell types using an iterative overlap removal procedure. We repeated this process for cell-type definitions at each level of the clustering tree and found that peak calling at more granular resolutions allowed us to preferentially detect distal regulatory elements. Unless otherwise noted, downstream analyses were carried out on the peak matrix called with coarse cell-type definitions (level 1, resolution 0.01).

Transcription factor activities

Transcription factor deviations were estimated by chromVAR[51], using motif sets from the chromVAR package (ENCODE, HOMER and CisBP) as well as the 2020 version of JASPAR[108]. Transcription factor motifs associated with cell-type identity were identified using a Wilcoxon rank-sum test, as in the Seurat function FindMarkers. Linear mixed models were used to identify transcription factor motifs differentially active in cells from injured spinal cords, using the 'lmerTest' R package to optimize the restricted maximum likelihood, and obtain *P* values from the Satterthwaite approximation for degrees of freedom and a false discovery rate of 10%.

To identify transcription factors that were up- or downregulated across all level 4 neuron subtypes at 7 days postinjury, we performed a one-sample *t*-test on coefficients estimated by the mixed models. To identify transcription factors with discordant patterns of up- or downregulation at 2 months postinjury, we devised a permutation-based statistical approach. Neuron subtype assignments at level 4 of the clustering tree were randomized within each experimental condition, and differential activity testing was performed using linear mixed models in the permuted data. This process was repeated 100 times, and the standard deviation of model coefficients was calculated for the observed and permuted datasets. The resulting *z* statistics were then converted to *P* values using a standard normal distribution and significantly divergent motifs were identified using a 10% false discovery rate.

To identify transcription factors associated with dysfunction of the tripartite barrier after SCI, BBB dysfunction module scores[22] were first estimated from the RNA modality of the multiome data, as in the snRNA-seq atlas. chromVAR deviations in the ATAC modality were then correlated to the resulting module scores, using the Pearson correlation and restricting this analysis to vascular cells. Linear mixed models were then used to identify motifs that were differentially accessible at 7 days in level 4 subtypes associated with the tripartite barrier, including vascular leptomeningeal cells, capillary endothelial cells, pericytes, arachnoid barrier cells, reactive astrocytes and OPCs.

Analyses of differentially active transcription factors in neurons or blood–spinal cord barrier cell types were carried out using chromVAR deviation matrices derived from peak matrices at the relevant resolution of the clustering tree, as described above.

Differential accessibility

To identify differentially accessible peaks, we extended the workflow for pseudobulk DE analysis in Libra to peak count matrices derived by ArchR. Cells of each type were aggregated within replicates to form pseudobulks, and then testing for differential accessibility was performed using the likelihood ratio test implemented in DESeq2 (ref. 106). The evolutionary conservation of each peak was quantified as the mean phyloP conservation score from the 60-way vertebrate dataset[54] of all bases within the peak. This score is inversely related to the *P* value of a statistical phylogenetic test under a null hypothesis of neutral evolution; thus, at any given position, a high phyloP score reflects evolutionary conservation, whereas a low phyloP score indicates a fast-evolving position. The evolutionary conservation of all peaks open within a given

cell was further summarized by taking the mean phyloP score across all accessible peaks in that cell.

Evolutionary divergence in circuit reorganization

The expression of cellular stress response programs in the snRNA-seq atlas was estimated by using the Seurat function AddModuleScore to summarize the mean expression of genes associated with the GO term GO:0033554 ('cellular response to stress'). The resulting score was then correlated with the circuit reorganization score described above across all neurons.

Spatial transcriptomics preprocessing and quality control

Following read alignment and count matrix generation with SpaceRanger as described above, Seurat[77] was used to calculate quality control metrics for each spatial barcode, including the number of genes detected, number of UMIs and proportion of reads aligned to mitochondrial genes. Low-quality barcodes were filtered by removing those with fewer than 3,000 or more than 45,000 UMIs; barcodes were not filtered on the basis of the proportion of mitochondrial counts. Low-quality sections were identified as those with distributions of number of UMIs, number of genes expressed or proportion of mitochondrial counts that differed markedly from the remainder of the sections in the dataset, and were removed. In the 2D spatial dataset, these steps afforded a UMI count matrix comprising 33,941 spatial barcodes from nine biological replicates (three from each experimental condition). In the 3D spatial dataset, these steps afforded a UMI count matrix comprising 37,558 spatial barcodes from three biological replicates (one from each experimental condition).

Registration to a common coordinate framework

We aligned all spatial transcriptomics sections into a common coordinate system using a custom image analysis pipeline that includes preprocessing, registration and combination of histological images from different sections, aspects of which have been previously described[8]. In brief, we implemented image preprocessing in Fiji, and registration procedures in R, using the image analysis package 'imager'. Segmentation of the histological sections and associated spatial barcodes from background was achieved using a custom macro in Fiji. Segmented sections were then aligned using imager. Image registration was performed manually using the tissue structure to guide registration, as captured by (1) histological images, (2) quality control statistics (for example, the percentage of mitochondrial counts), (3) marker genes for coarse cell types and dorsoventral or rostrocaudal transcription factors (for example, *Ebf1*, *Esrrg* and *Hox* genes) and (4) unsupervised clustering of the spatial barcodes, as implemented within Seurat.

Visualization

Quality control metrics and marker gene expression were smoothed before visualization on the 2D spinal cord using locally weighted regression, as implemented in the RCTD package[109]. Visualization of the 3D spinal cord was achieved with Imaris (Bitplane, v.9.0.0). In brief, the 3D spatial transcriptomics data was binned along the *z* dimension into slices of 10 μm. Within each slice, quantitative values (quality control metrics, gene expression, gene module scores and chromVAR deviations) were smoothed using 3D locally weighted regression. When several quantitative values were assigned to a single spatial coordinate (for example, when performing spatial prioritization on snRNA-seq barcodes embedded by means of Tangram), the mean value at each coordinate was assigned, with the exception of the expression of individual genes for which the maximum value at each coordinate was assigned instead. Each barcode was then assigned a size of 3 pixels, and the resulting slices were exported as 16 bit greyscale TIFF files using imager for import into Imaris. Separate reconstructions of the 3D spinal cord volume were performed for each experimental condition in the spatiotemporal atlas (that is, uninjured, 7 days and 2 months).

DE

To identify genes differentially expressed between regions in the injured spinal cord within the 2D spatial dataset, we extended the workflow for pseudobulk DE analysis in Libra to spatial count matrices derived by SpaceRanger. Cells from each region were aggregated within replicates to form pseudobulks, and then testing for DE was performed using the likelihood ratio test implemented in edgeR[105]. DE analysis was performed separately for spinal cord regions at 7 days and 2 months postinjury. DE gene expression was visualized on the 2D spinal cord using 2D locally weighted regression, as implemented in the RCTD package[109].

Cell-type deconvolution

To integrate our snRNA-seq atlas with the 2- and 3D spatial atlases, we used RCTD[109] to deconvolve spatial barcodes into a mixture of one or more cell types, while accounting for technical differences between single-nucleus and spatial transcriptomes. RCTD was run with doublet mode disabled, allowing each barcode to potentially contain more than two cell types, separately for cell-type definitions at level 1 and 2 of the clustering tree. We recovered smoothed patterns of cell-type abundance by 2D locally weighted regression of deconvolution weights, as described by the authors of RCTD[109]. Separately, a single cell type was assigned to each spatial barcode by taking the maximum deconvolution weight assigned by RCTD for that barcode. For cell-type definitions at level 2 of the clustering tree, only subtypes of the assigned level 1 cell types were considered as potential matches for each spatial barcode.

Spatial prioritization with Magellan

To characterize the spatial response to SCI in an unbiased manner, we used a machine-learning method spatial prioritization that we recently developed, named Magellan[8]. Magellan builds on the concept of transcriptional separability that provides a basis for cell-type prioritization in Augur, as described above. However, in spatial transcriptomics data, the analytical level of interest is not necessarily a cell type, but rather a coordinate within a 2- or 3D tissue. To approach the data at this level, we sought to evaluate the transcriptional separability between barcodes from two experimental conditions at each point within a common coordinate system. We reasoned that we could achieve this by evaluating the separability of barcodes from each condition within small, overlapping tiles, layered across the spatial coordinate system. Briefly, for each barcode in a spatial transcriptomics dataset, Magellan selects the *k* nearest neighbours from each experimental condition within common coordinate space, where *k* is set to 20 by default. Then, Magellan withholds the experimental condition labels for a proportion of these neighbours, and trains a random forest classifier to predict the experimental condition given the remaining barcodes as input. The accuracy of these predictions is evaluated in the withheld barcodes, and the process is repeated in threefold cross-validation. As in Augur, the accuracy is quantified using the AUC. The cross-validation is repeated several times (by default, 50 times) in order to converge at a robust estimate of the AUC. The entire procedure is repeated for each barcode in the dataset, providing a spatial map of the AUC over the coordinate system of the spatial transcriptomes.

Magellan was used to perform spatial prioritization in the 2D spatial dataset by comparing registered spatial transcriptomes from each pair of experimental conditions (uninjured, 7 days, 2 months). To visualize the intensity of the perturbation response, the spatial AUC was smoothed by 2D locally weighted regression, as described by the authors of RCTD[109]. In addition, we performed a one-dimensional locally weighted regression to visualize the intensity of the perturbation response along the rostrocaudal axis of the spinal cord.

To more carefully dissect the transcriptional basis of the perturbation response detected by Magellan, we tested for correlation between gene expression and the AUC of spatial prioritization. In brief, we filtered

the UMI count matrix within each comparison to include only genes detected in at least 100 spatial barcodes, and then computed Pearson correlations between scaled and log-normalized gene expression vectors and the AUCs returned for each barcode by Magellan. We further identified genes that were differentially correlated with the AUCs at 7 days and 2 months by testing for differential correlations using the Fisher *z* transformation, adapting code from the DGCA R package[110]. We extended this concept by computing module scores for GO terms for each spatial barcode with the Seurat function AddModuleScore, as described above, and testing for significant correlations between GO module scores and the AUCs returned by Magellan. As in the DE analysis, the expression of genes or GO modules correlated or anticorrelated with the AUC of spatial prioritization was visualized on the 2D spinal cord using 2D locally weighted regression, as implemented in the RCTD package[109].

Integration of the *Tabulae Paralytica*

To integrate all four *Tabulae* into a single framework, we leveraged Tangram[111] to to embed single-nucleus transcriptomes and epigenomes onto the common coordinate system established by our 4D atlas of the mouse spinal cord. Alignment of snRNA-seq barcodes into the spatiotemporal atlas was performed separately for each experimental condition in the snRNA-seq and multiome atlases, using the most similar condition in the spatiotemporal atlas as a reference (for example, aligning cells from 14 days to the spatiotemporal atlas at 7 days and cells from 1 month to the spatiotemporal atlas at 2 months). Tangram was run with the top 500 highly variable genes for each cell type and using cell-type definitions at level 4 of the clustering tree.

This procedure assigned *x*, *y* and *z* coordinates to each nuclei in the snRNA-seq and multiome atlases. We then used Magellan to perform 3D spatial prioritization on the spatialized single-nucleus data, using the coordinates assigned by Tangram for each barcode. Spatialized cells from each injury severity were compared to those from uninjured mice. Separately, spatialized cells from old mice were compared to those from injured young mice at the same time point. Moreover, we again tested for correlation between gene expression in spatialized cells and the AUC of 3D spatial prioritization.

Gene modules associated with BBB endothelial cell identity and peripheral endothelial cell identity were obtained from the literature[22], and their expression in spatial barcodes was calculated using the Seurat function AddModuleScore. Similarly, we used the average expression of genes associated with the GO term GO:0031175 (neural projection development) to construct a circuit reorganization score, as described above for the snRNA-seq atlas, and visualized the expression of this score in spatialized neurons from the snRNA-seq atlas. Last, to summarize the expression of the conserved early response module in neurons, we selected the top 25 genes that were upregulated in the greatest number of level 4 neuron subtypes and with the greatest mean log-fold change at 1 day postinjury, and used the Seurat function AddModuleScore to summarize the expression of this gene module.

Transcription factor accessibility at 7 days was visualized on the 4D atlas by first embedding individual nuclei from multiome atlas onto the 3D coordinate system of the spinal cord, and then visualizing chromVAR deviations from linked epigenomes for each nucleus.

Statistics, power calculations, group sizes, reproducibility and visualization

Statistical evaluations of repeated measures were conducted by one-way analysis of variance with post hoc independent pairwise analysis as per Tukey's honestly significant difference test. For all photomicrographs of histological tissue, staining experiments were repeated independently with tissue from at least four, and in most cases six, different animals with similar results. Throughout the paper, the box plots show the median (horizontal line), interquartile range (hinges) and smallest and largest values no more than 1.5 times the interquartile range (whiskers).

Reporting summary

Further information on research design is available in the Nature Portfolio Reporting Summary linked to this article.

Data availability

Sequencing data have been deposited to the Gene Expression Omnibus (GSE234774, snRNA-seq and spatial transcriptomics, and GSE230765, multiome). Source data are provided with this paper.

Code availability

Augur, Libra and Magellan are available from GitHub (https://github.com/neurorestore/Augur, https://github.com/neurorestore/Libra and https://github.com/neurorestore/Magellan).

60. Wells, J. E. A., Hurlbert, R. J., Fehlings, M. G. & Yong, V. W. Neuroprotection by minocycline facilitates significant recovery from spinal cord injury in mice. *Brain* **126**, 1628–1637 (2003).
61. Stirling, D. P. et al. Minocycline treatment reduces delayed oligodendrocyte death, attenuates axonal dieback, and improves functional outcome after spinal cord injury. *J. Neurosci.* **24**, 2182–2190 (2004).
62. Festoff, B. W. et al. Minocycline neuroprotects, reduces microgliosis, and inhibits caspase protease expression early after spinal cord injury. *J. Neurochem.* **97**, 1314–1326 (2006).
63. Rabchevsky, A. G., Fugaccia, I., Sullivan, P. G., Blades, D. A. & Scheff, S. W. Efficacy of methylprednisolone therapy for the injured rat spinal cord. *J. Neurosci. Res.* **68**, 7–18 (2002).
64. James, N. D. et al. Chondroitinase gene therapy improves upper limb function following cervical contusion injury. *Exp. Neurol.* **271**, 131–135 (2015).
65. Muir, E. M. et al. Modification of N-glycosylation sites allows secretion of bacterial chondroitinase ABC from mammalian cells. *J. Biotechnol.* **145**, 103–110 (2010).
66. Bartus, K. et al. Large-scale chondroitin sulfate proteoglycan digestion with chondroitinase gene therapy leads to reduced pathology and modulates macrophage phenotype following spinal cord contusion injury. *J. Neurosci.* **34**, 4822–4836 (2014).
67. Esposito, M. S., Capelli, P. & Arber, S. Brainstem nucleus MdV mediates skilled forelimb motor tasks. *Nature* **508**, 351–356 (2014).
68. Kathe, C. et al. Wireless closed-loop optogenetics across the entire spinal cord in ecological environments. *Nat. Biotechnol.* **40**, 198–208 (2022).
69. Takeoka, A., Vollenweider, I., Courtine, G. & Arber, S. Muscle spindle feedback directs locomotor recovery and circuit reorganization after spinal cord injury. *Cell* **159**, 1626–1639 (2014).
70. Mathis, A. et al. DeepLabCut: markerless pose estimation of user-defined body parts with deep learning. *Nat. Neurosci.* **21**, 1281–1289 (2018).
71. Chung, K. et al. Structural and molecular interrogation of intact biological systems. *Nature* **497**, 332–337 (2013).
72. Tomer, R., Ye, L., Hsueh, B. & Deisseroth, K. Advanced CLARITY for rapid and high-resolution imaging of intact tissues. *Nat. Protoc.* **9**, 1682–1697 (2014).
73. Voigt, F. F. et al. The mesoSPIM initiative: open-source light-sheet microscopes for imaging cleared tissue. *Nat. Methods* **16**, 1105–1108 (2019).
74. Zheng, G. X. Y. et al. Massively parallel digital transcriptional profiling of single cells. *Nat. Commun.* **8**, 14049 (2017).
75. Caglayan, E., Liu, Y. & Konopka, G. Neuronal ambient RNA contamination causes misinterpreted and masked cell types in brain single-nuclei datasets. *Neuron* **110**, 4043–4056.e5 (2022).
76. Fleming, S. J. et al. Unsupervised removal of systematic background noise from droplet-based single-cell experiments using CellBender. *Nat. Methods* **20**, 1323–1335 (2023).
77. Stuart, T. et al. Comprehensive integration of single-cell data. *Cell* **177**, 1888–1902.e21 (2019).
78. McGinnis, C. S., Murrow, L. M. & Gartner, Z. J. DoubletFinder: doublet detection in single-cell RNA sequencing data using artificial nearest neighbors. *Cell Syst* **8**, 329–337. e4 (2019).
79. Germain, P.-L., Lun, A., Meixide, C. G., Macnair, W. & Robinson, M. D. Doublet identification in single-cell sequencing data using scDblFinder. *F1000Res.* **10**, 979 (2021).
80. Bais, A. S. & Kostka, D. scds: computational annotation of doublets in single-cell RNA sequencing data. *Bioinformatics* **36**, 1150–1158 (2019).
81. Xi, N. M. & Li, J. J. Benchmarking computational doublet-detection methods for single-cell RNA sequencing data. *Cell Syst.* **12**, 176–194.e6 (2021).
82. Korsunsky, I. et al. Fast, sensitive and accurate integration of single-cell data with Harmony. *Nat. Methods* **16**, 1289–1296 (2019).
83. Osseward, P. J. et al. Conserved genetic signatures parcellate cardinal spinal neuron classes into local and projection subsets. *Science* **372**, 385–393 (2021).
84. Häring, M. et al. Neuronal atlas of the dorsal horn defines its architecture and links sensory input to transcriptional cell types. *Nat. Neurosci.* **21**, 869–880 (2018).
85. Alkaslasi, M. R. et al. Single nucleus RNA-sequencing defines unexpected diversity of cholinergic neuron types in the adult mouse spinal cord. *Nat. Commun.* **12**, 2471 (2021).
86. Blum, J. A. et al. Single-cell transcriptomic analysis of the adult mouse spinal cord reveals molecular diversity of autonomic and skeletal motor neurons. *Nat. Neurosci.* **24**, 572–583 (2021).
87. Delile, J. et al. Single cell transcriptomics reveals spatial and temporal dynamics of gene expression in the developing mouse spinal cord. *Development* **146**, dev173807 (2019).

88. Hamel, R. et al. Time-resolved single-cell RNAseq profiling identifies a novel Fabp5-expressing subpopulation of inflammatory myeloid cells in chronic spinal cord injury. Preprint at *bioRxiv* https://doi.org/10.1101/2020.10.21.346635 (2020).
89. Hayashi, M. et al. Graded arrays of spinal and supraspinal v2a interneuron subtypes underlie forelimb and hindlimb motor control. *Neuron* **97**, 869–884.e5 (2018).
90. Rosenberg, A. B. et al. Single-cell profiling of the developing mouse brain and spinal cord with split-pool barcoding. *Science* **360**, 176–182 (2018).
91. Sathyamurthy, A. et al. Massively parallel single nucleus transcriptional profiling defines spinal cord neurons and their activity during behavior. *Cell Rep.* **22**, 2216–2225 (2018).
92. Wahane, S. et al. Diversified transcriptional responses of myeloid and glial cells in spinal cord injury shaped by HDAC3 activity. *Sci. Adv.* **7**, eabd8811 (2021).
93. Baek, M., Menon, V., Jessell, T. M., Hantman, A. W. & Dasen, J. S. Molecular logic of spinocerebellar tract neuron diversity and connectivity. *Cell Rep.* **27**, 2620–2635.e4 (2019).
94. Vanlandewijck, M. et al. A molecular atlas of cell types and zonation in the brain vasculature. *Nature* **554**, 475–480 (2018).
95. Marques, S. et al. Oligodendrocyte heterogeneity in the mouse juvenile and adult central nervous system. *Science* **352**, 1326–1329 (2016).
96. O'Shea, T. M. et al. Border-forming wound repair astrocytes. Preprint at *bioRxiv*, https://doi.org/10.1101/2023.08.25.554857 (2023).
97. Liddelow, S. A. et al. Neurotoxic reactive astrocytes are induced by activated microglia. *Nature* **541**, 481–487 (2017).
98. Tirosh, I. et al. Dissecting the multicellular ecosystem of metastatic melanoma by single-cell RNA-seq. *Science* **352**, 189–196 (2016).
99. Hou, W. & Ji, Z. Palo: spatially aware color palette optimization for single-cell and spatial data. *Bioinformatics* **38**, 3654–3656 (2022).
100. Koopmans, F. et al. SynGO: an evidence-based, expert-curated knowledge base for the synapse. *Neuron* **103**, 217–234.e4 (2019).
101. Büttner, M., Ostner, J., Müller, C. L., Theis, F. J. & Schubert, B. scCODA is a Bayesian model for compositional single-cell data analysis. *Nat. Commun.* **12**, 6876 (2021).
102. Phipson, B. et al. propeller: testing for differences in cell type proportions in single cell data. *Bioinformatics* **38**, 4720–4726 (2022).
103. Simmons, S. Cell type composition analysis: comparison of statistical methods. Preprint at *bioRxiv* https://doi.org/10.1101/2022.02.04.479123 (2022).
104. Zimmerman, K. D., Espeland, M. A. & Langefeld, C. D. A practical solution to pseudoreplication bias in single-cell studies. *Nat. Commun.* **12**, 738 (2021).
105. Robinson, M. D., McCarthy, D. J. & Smyth, G. K. edgeR: a Bioconductor package for differential expression analysis of digital gene expression data. *Bioinformatics* **26**, 139–140 (2010).
106. Love, M. I., Huber, W. & Anders, S. Moderated estimation of fold change and dispersion for RNA-seq data with DESeq2. *Genome Biol.* **15**, 550 (2014).
107. Zhang, Y. et al. Model-based analysis of ChIP-seq (MACS). *Genome Biol.* **9**, R137 (2008).
108. Fornes, O. et al. JASPAR 2020: update of the open-access database of transcription factor binding profiles. *Nucleic Acids Res.* **48**, D87–D92 (2020).
109. Cable, D. M. et al. Robust decomposition of cell type mixtures in spatial transcriptomics. *Nat. Biotechnol.* https://doi.org/10.1038/s41587-021-00830-w (2021).
110. McKenzie, A. T., Katsyv, I., Song, W.-M., Wang, M. & Zhang, B. DGCA: a comprehensive R package for differential gene correlation analysis. *BMC Syst. Biol.* **10**, 106 (2016).
111. Biancalani, T. et al. Deep learning and alignment of spatially resolved single-cell transcriptomes with Tangram. *Nat. Methods* **18**, 1352–1362 (2021).

Acknowledgements This work was supported by the Swiss National Science Foundation (grant nos. 310030_192558 to G.C., PZ00P3_185728 to M.A.A. and PZ00P3_208988 to J.W.S.); the ALARME Foundation (to M.A.A. and G.C.); the Dr Miriam and Sheldon G. Adelson Medical Foundation (to M.V.S.); Wings for Life (to M.V.S. and M.A.S.); the Wyss Center for Bio and Neuroengineering (to M.A.A. and G.C.); and a Human Frontiers in Science Program long-term fellowship (grant no. LT001278/2017-L to C.K.). We are grateful to J. Ravier and F. Merlos for the illustrations; the Advanced Lightsheet Imaging Center (ALICe) at the Wyss Center for Bio and Neuroengineering, Geneva and E. Bradbury for providing ChABC vectors. This work was supported in part using the resources and services of the Gene Expression Core Facility and the Bertarelli Platform for Gene Therapy at the School of Life Sciences of the EPFL. We acknowledge the foundational work by the many investigators whose work we could not cite due to space limits.

Author contributions J.W.S., J.B., M.V.S., M.A.A., M.A.S. and G.C. conceived and designed experiments. J.W.S., M.A.A., C.K., M.G., T.H.H., A.L., A.d.C., N.R., V.A. and N.D.J. conducted experiments. J.W.S., M.A.S., M.G., Q.B. and A.Y.Y.T. analysed the data. B.S. contributed essential resources. J.W.S., M.A.S., M.A.A. and G.C. wrote the manuscript. All authors contributed to the editing of the manuscript.

Competing interests The authors declare no competing interests.

Additional information

Supplementary information The online version contains supplementary material available at https://doi.org/10.1038/s41586-024-07504-y.

Correspondence and requests for materials should be addressed to Mark A. Anderson, Jordan W. Squair or Grégoire Courtine.

Peer review information *Nature* thanks Binhai Zheng and the other, anonymous, reviewer(s) for their contribution to the peer review of this work.

Reprints and permissions information is available at http://www.nature.com/reprints.

Extended Data Fig. 1 | Clustering tree of 180 cell types and subtypes in the snRNA-seq atlas. a, Clustering tree of the mouse spinal cord, revealing the hierarchical relationships between spinal cord cell types across levels 1 to 3 in the taxonomy, with cell types at level 3 highlighted. Text at the top of the tree shows the clades of the clustering tree corresponding to the major cell types of the mouse spinal cord (i.e., level 1 in the taxonomy). **b**, As in **a**, but showing level 4 in the taxonomy. **c**, As in **a**, but showing level 5 in the taxonomy.

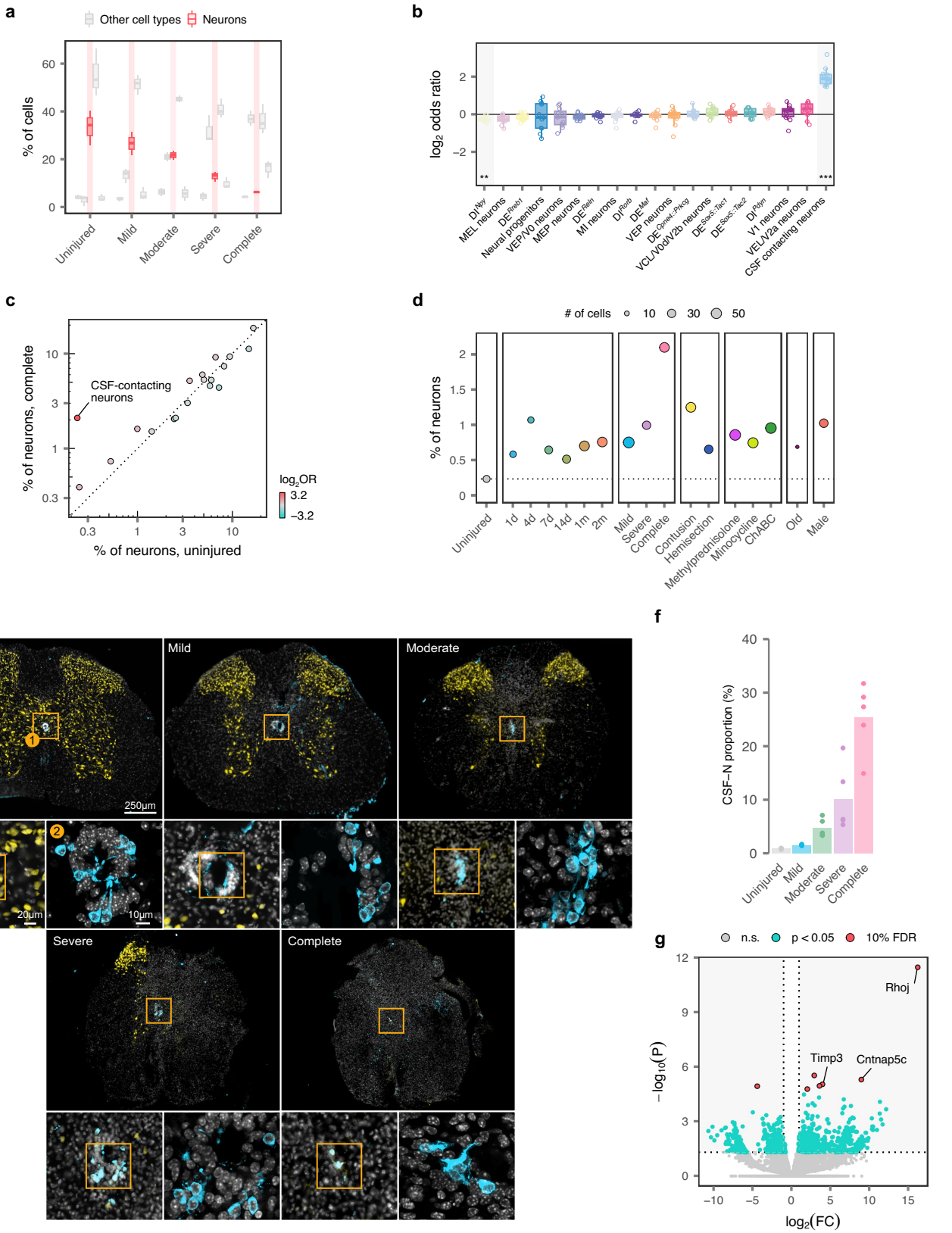

Extended Data Fig. 2 | See next page for caption.

Extended Data Fig. 2 | Neuronal susceptibility and resilience to SCI. **a**, Boxplot highlighting the proportion of neurons within individual libraries from the severity experiment, as compared to other major cell types. **b**, Boxplot showing the log_2-odds ratio comparing the proportions of neurons from each level 4 subtype between the uninjured spinal cord, for all comparisons involving the injured spinal cord at 7 days post-injury. Cerebrospinal fluid-contacting neurons are the lone subpopulation to exhibit statistically significant resilience following SCI. **, $p < 0.01$; ***, $p < 0.001$. **c**, Scatterplot highlighting an individual comparison from **b**, showing the proportions of neurons from each level 4 subtype in the uninjured spinal cord, x-axis, and 7 days after a complete injury, y-axis. Color shows the log_2-odds ratio. Cerebrospinal fluid-contacting neurons are highlighted. **d**, Proportion, y-axis, and absolute number, point size, of cerebrospinal fluid-contacting neurons recovered from each experimental condition. Dotted line shows the proportion of cerebrospinal fluid-contacting neurons in the uninjured spinal cord. **e**, Representative histological photomicrographs show injured spinal cords across injury severities after staining for NeuN and PKD1L2, a marker of cerebrospinal fluid-contacting neurons. **f**, Quantification of histological data demonstrating increasing proportions of cerebrospinal fluid-contacting neurons across injury severities. **g**, Volcano plot showing differentially expressed genes in cerebrospinal fluid-contacting neurons following spinal cord injury, as compared to other neuron subtypes.

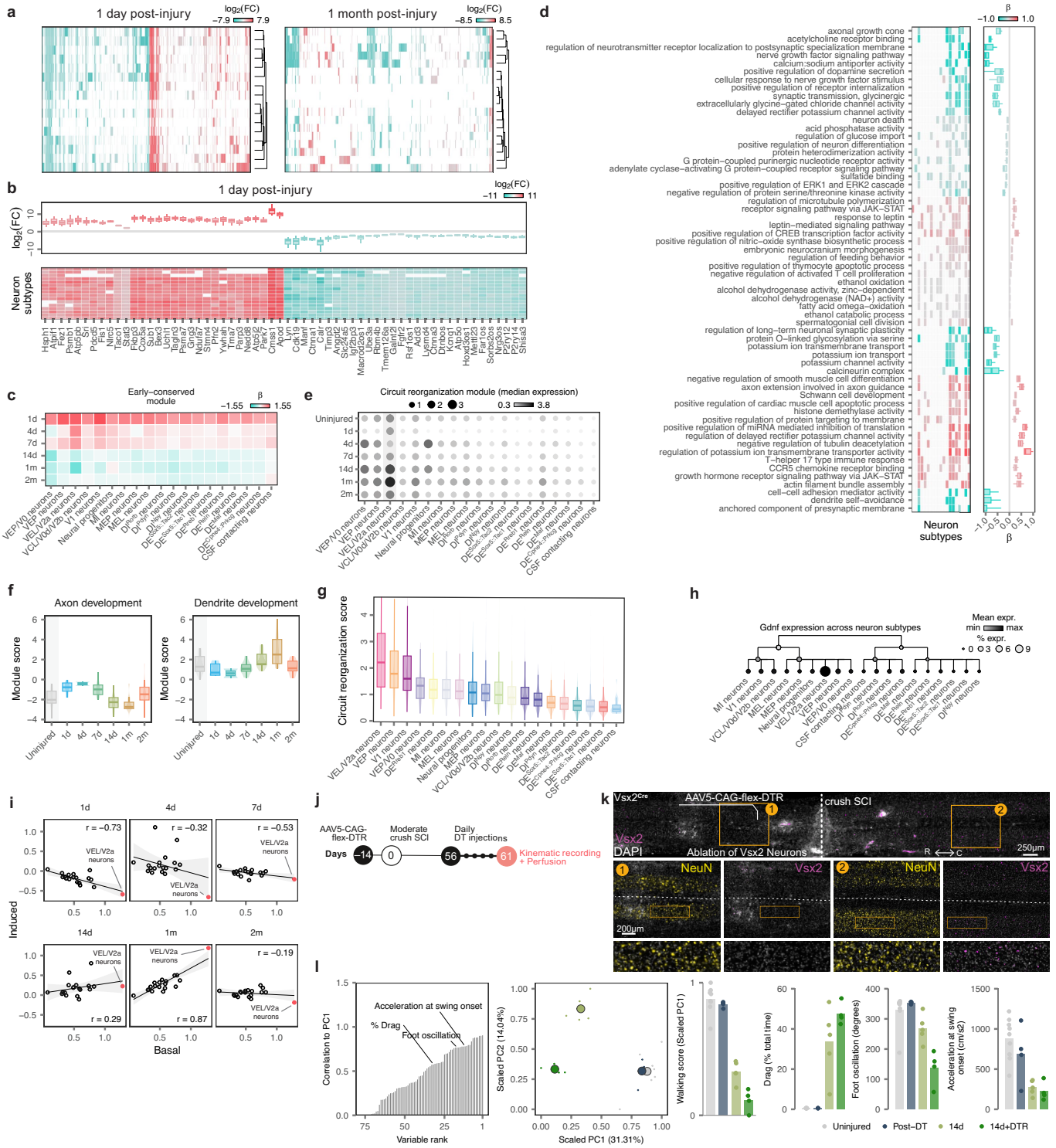

Extended Data Fig. 3 | See next page for caption.

Extended Data Fig. 3 | Conserved and divergent neuronal responses to SCI. **a**, Heatmap showing fold changes for all genes differentially expressed after SCI in at least one level 4 neuron subtype at 1 day, top, and 1 month, bottom, after injury. Patterns of differential expression are broadly conserved at 1 day, but more subtype-specific at 1 month. **b**, Heatmap showing fold changes for selected genes with broadly conserved patterns of differential expression across level 4 neuron subtypes at 1 day post-injury. **c**, Heatmap showing coefficients estimated by linear mixed models within each neuron subtype for up- or downregulation of the early-conserved neuronal module over the injury timecourse. **d**, Heatmap showing coefficients estimated by linear mixed models within each neuron subtype for selected GO term modules with broadly conserved patterns of up- or downregulation across level 4 neuron subtypes at 1 day post-injury. **e**, Dot plot showing median expression of the circuit reorganization module in each level 4 neuron subtype across timepoints. Point color and size both show median expression of the circuit reorganization module. **f**, Boxplots showing expression of the axon development, left, and dendrite development, right modules in Vsx2-expressing neurons across timepoints. **g**, Boxplot showing expression of the circuit reorganization module in each level 4 neuron subtype within the uninjured spinal cord. Vsx2-expressing neurons display the highest expression of the circuit reorganization module in the uninjured spinal cord. **h**, Dendrogram showing expression of the growth factor *Gdnf* across levels 1 to 4 of the neuron taxonomy. Point color shows mean expression in each neuron subtype, while point size reflects the proportion of neurons of that subtype with detectable expression. **i**, Scatterplots comparing basal expression of the circuit reorganization module in the uninjured spinal cord, x-axis, with the SCI-induced upregulation of this module at each timepoint after injury, y-axis, for each level 4 neuron subtype. Inset text shows the Pearson correlation. Basal and induced expression of the circuit reorganization module is maximally correlated at 1 month post-injury, coinciding with the temporal window of opportunity for natural recovery after SCI. **j**, Timeline of $Vsx2^{ON}$ neuron diphtheria toxin ablation experiments. Two weeks before complete crush SCI, animals received an injection of AAVs expressing DTR. At eight weeks, animals received daily injections of diphtheria toxin for 7 days. Kinematics were then recorded and tissue was collected for evaluation. **k**, Histological verification of $Vsx2^{ON}$ neuron ablation in the lower thoracic region. Images show loss of $Vsx2^{ON}$ neurons in the thoracic spinal cord, above and below the level of the crush SCI. Bar graph shows the number of $Vsx2^{ON}$ neurons found in each animal ($n = 4$ mice per group, independent samples two-tailed t-test, $t = 11.7$, $p = 2.4 \times 10{-}5$). **l**, Locomotor performance in the $Vsx2^{ON}$ ablation experiment, as quantified in Supplementary Fig. 3 ($n > 10$ gait cycles per mouse, $n = 4$ mice per group).

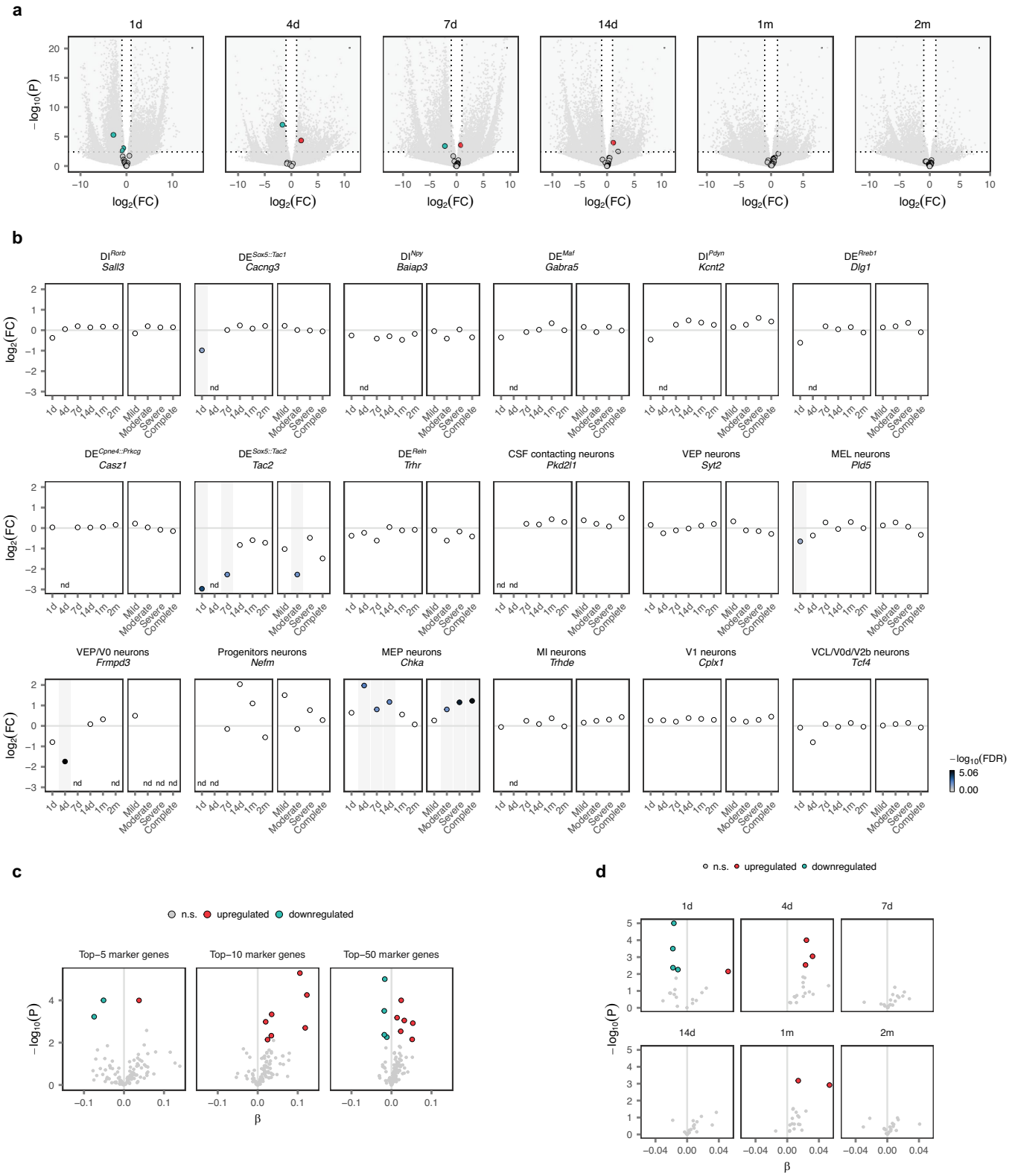

Extended Data Fig. 4 | See next page for caption.

Extended Data Fig. 4 | Neurons remain differentiated after SCI. a, Volcano plots showing differential expression for all level 4 neuron subtypes simultaneously across timepoints. Enlarged points represent the key marker genes for each neuron subtype shown in Supplementary Fig. 11a. Marker genes shown in grey show no evidence of differential expression after SCI in their respective neuron subtype. **b**, Differential expression of key marker genes for level 4 neuron subtypes across timepoints and injury severities (log_2-fold change, y-axis, and false discovery rate, point color). Timepoints or severities for which key marker genes show evidence of statistically significant differential expression, compared to uninjured neurons, are plotted with light grey backgrounds. Genes without statistical evidence of differential expression (i.e., FDR greater than 5%) are shown as white points. n.d., genes that were not detectably expressed and could not be subjected to DE analysis. **c**, Volcano plot showing differential expression for averaged gene expression modules comprising the top 5, top 10, or top 50 marker genes identified for each level 4 neuron subtype by unbiased comparisons with all other neurons, simultaneously across all timepoints. The vast majority of marker gene modules show no evidence of downregulation after SCI in their respective neuron subtype. **d**, As in **c**, but showing differential expression for averaged gene expression modules comprising the top 50 marker genes for each level 4 neuron subtype, shown separately for each condition in the timecourse experiment.

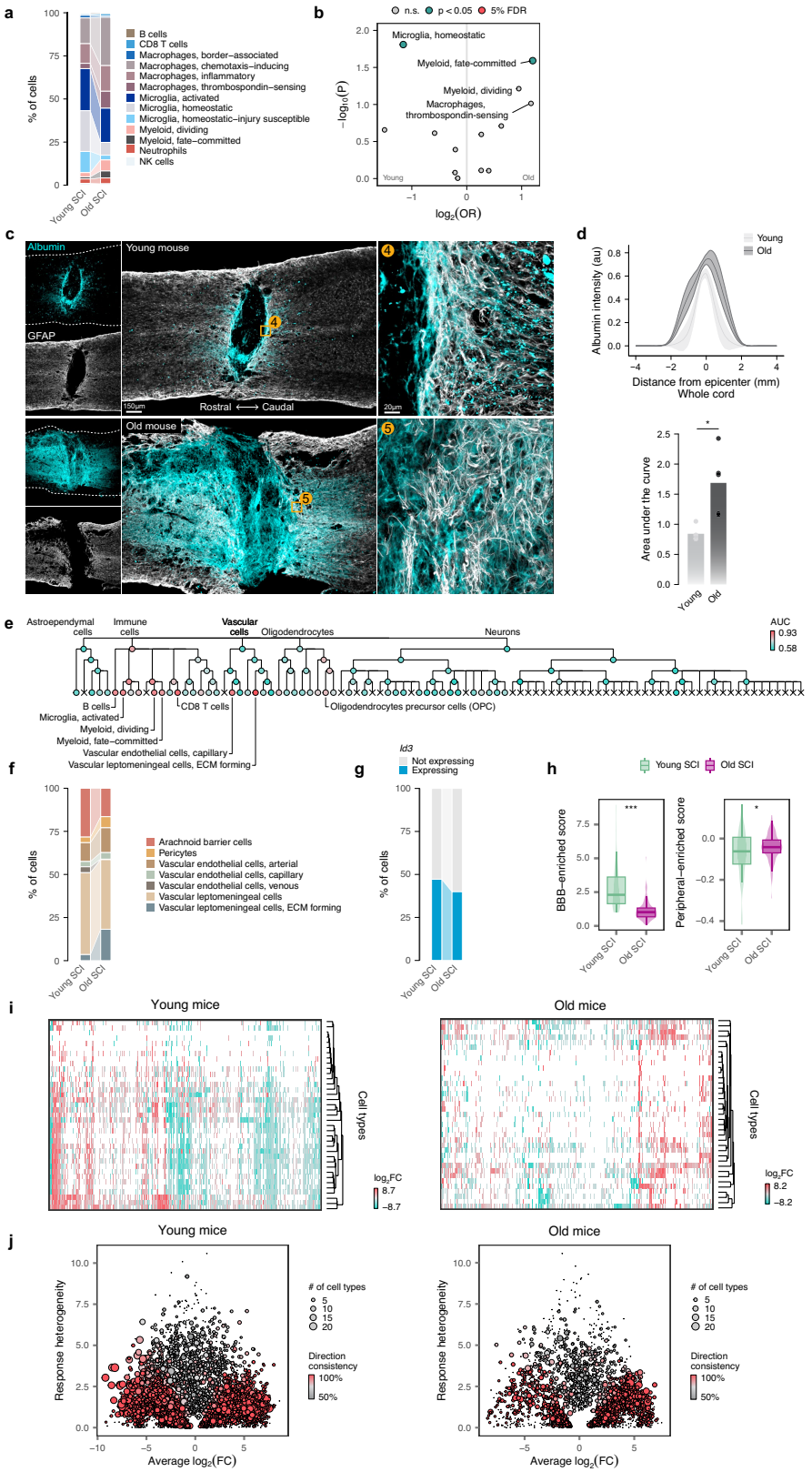

Extended Data Fig. 5 | See next page for caption.

Extended Data Fig. 5 | Failure of tripartite barrier formation in old mice. **a**, Sankey diagram showing the proportions of immune cell subtypes in young and old mice at seven days post-injury. **b**, Volcano plot showing the statistical significance of changes in immune cell subtype proportions between young and old mice. **c**, Composite tiled scans and confocal insets of albumin and GFAP in horizontal sections from representative old and young mice at two weeks after SCI. **d**, Line graph demonstrates albumin intensity at specific distances rostral and caudal to lesion centers. Bottom right, bar graph indicates the area under the curve (independent samples two-tailed t-test, $n = 5$ per group, $t = -3.47$, $p = 0.022$). **e**, Dendrogram showing cell type prioritizations assigned by Augur across the cellular taxonomy of the spinal cord in comparisons of young and old mice at seven days post-injury. The eight level 5 cell types with the highest AUCs are annotated. **f**, Sankey diagram showing the proportions of vascular cell subtypes in young and old mice at seven days post-injury. **g**, Sankey diagram showing the proportions of astroependymal cells expressing *Id3* in young and old mice at seven days post-injury ($p = 1.9 \times 10^{-3}$, χ^2 test). **h**, Average expression of the BBB identity module, left, and the peripheral vascular identity module, right, in capillary endothelial cells from young and old mice at seven days post-injury. **i**, Heatmap showing log-fold changes for all genes differentially expressed in at least one level 4 cell type in comparisons of injured versus uninjured mice, top, and old versus young mice, bottom. **j**, Heterogeneity of differential expression in comparisons of injured versus uninjured mice, top, and old versus young mice, bottom. Each point shows a gene differentially expressed in at least one level 4 cell type. The x-axis shows the average $\log_2$-fold change across all cell types; the y-axis shows the standard deviation of the $\log_2$-fold change across cell types ("response heterogeneity"); point size reflects the total number of cell types in which the gene is differentially expressed; and point color reflects the proportion of cell types in which the sign of the $\log_2$-fold change was the same as the modal sign ("direction consistency").

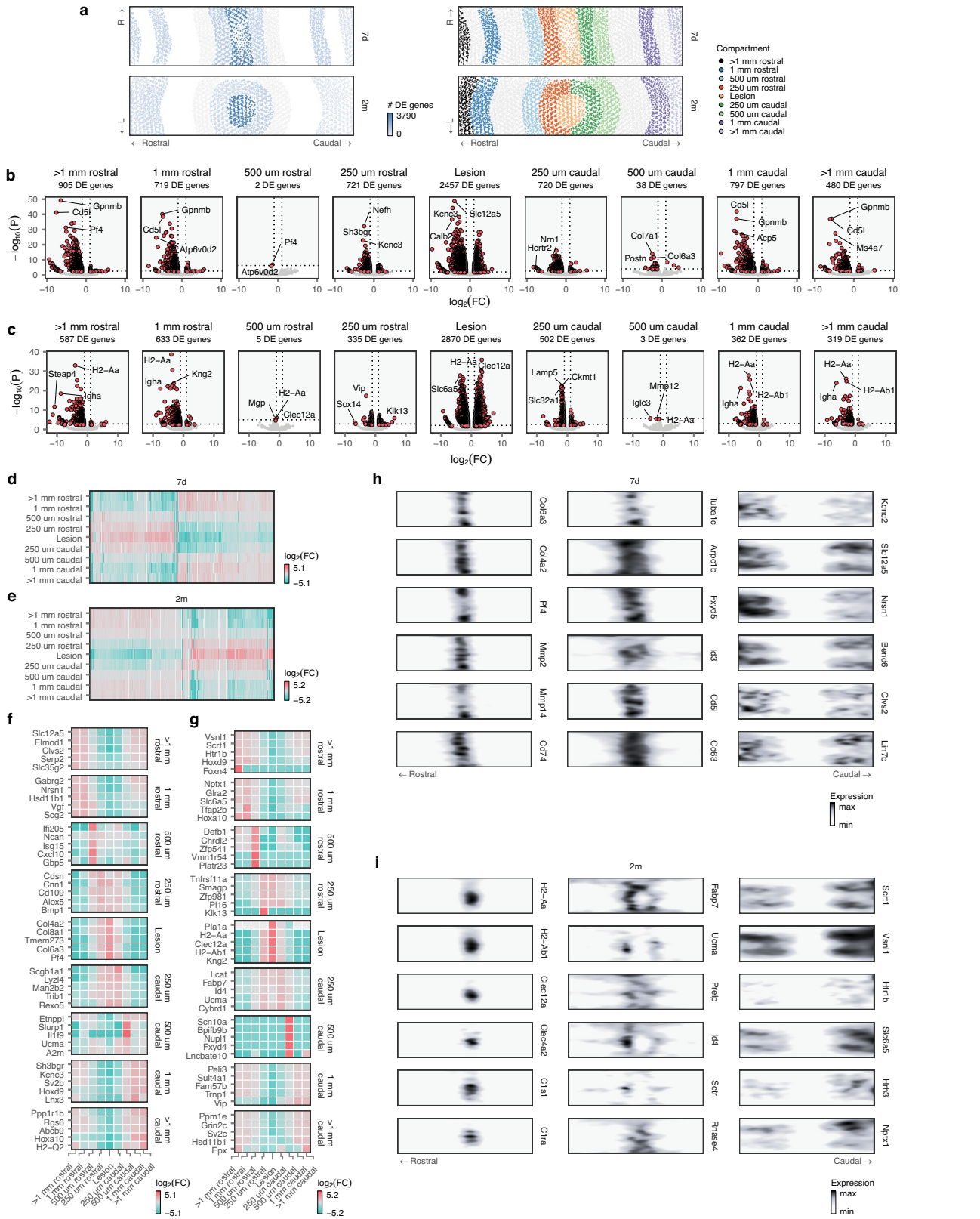

Extended Data Fig. 6 | Shared and distinct programs of gene expression across lesion compartments. a, Left, total number of differentially expressed genes detected within each lesion compartment at 7 days and 2 months after SCI. Right, legend showing the position of each lesion compartment, as in Fig. 6c. **b-c**, Volcano plots showing differentially expressed genes for all lesion compartments at 7 days, **b**, and 2 months, **c**. The top three genes per lesion compartment, as ranked by the product of the $\log_2$-fold change and the $-\log_{10}$ p-value, are annotated. **d-e**, Heatmap showing $\log_2$-fold changes for all genes differentially expressed in at least one lesion compartment at 7 days, **d**, and 2 months, **e**. **f-g**, Heatmap showing $\log_2$-fold changes for the top five genes differentially expressed in each lesion compartment at 7 days, **f**, and 2 months, **g**. **h-i**, Visualization of selected differentially expressed genes specific to individual lesion compartments at 7 days, **h**, and 2 months, **i**, on the two- dimensional coordinate system of the injured spinal cord.

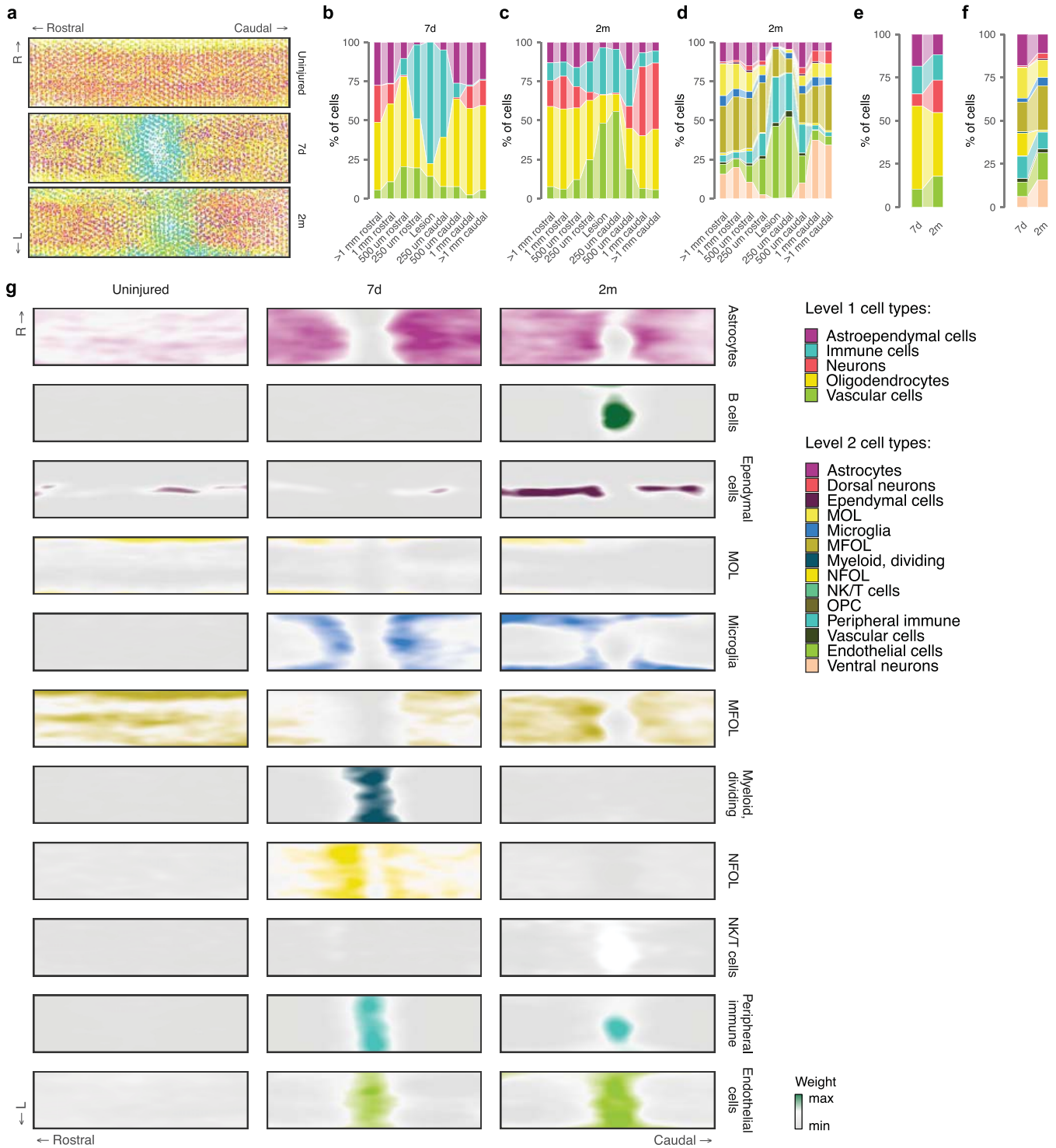

Extended Data Fig. 7 | Cell type deconvolution of the 2D spatial atlas. **a**, Major cell types assigned to each spatial barcode, visualized for each experimental condition on the two-dimensional coordinate system of the injured spinal cord. **b**, Sankey diagram showing the cellular composition of each lesion compartment at 7 days, for major (level 1) cell types. **c**, Sankey diagram showing the cellular composition of each lesion compartment at 2 months, for level 1 cell types. **d**, Sankey diagram showing the cellular composition of each lesion compartment at 2 months, for level 2 cell types. **e**, Sankey diagram showing the evolution of the cellular composition of the entire injured spinal cord between 7 days and 2 months, for level 1 cell types. **f**, Sankey diagram showing the evolution of the cellular composition of the entire injured spinal cord between 7 days and 2 months, for level 2 cell types. **g**, Visualization of the deconvolution weights assigned by RCTD for selected level 2 cell types at each timepoint, on the two-dimensional coordinate system of the injured spinal cord.

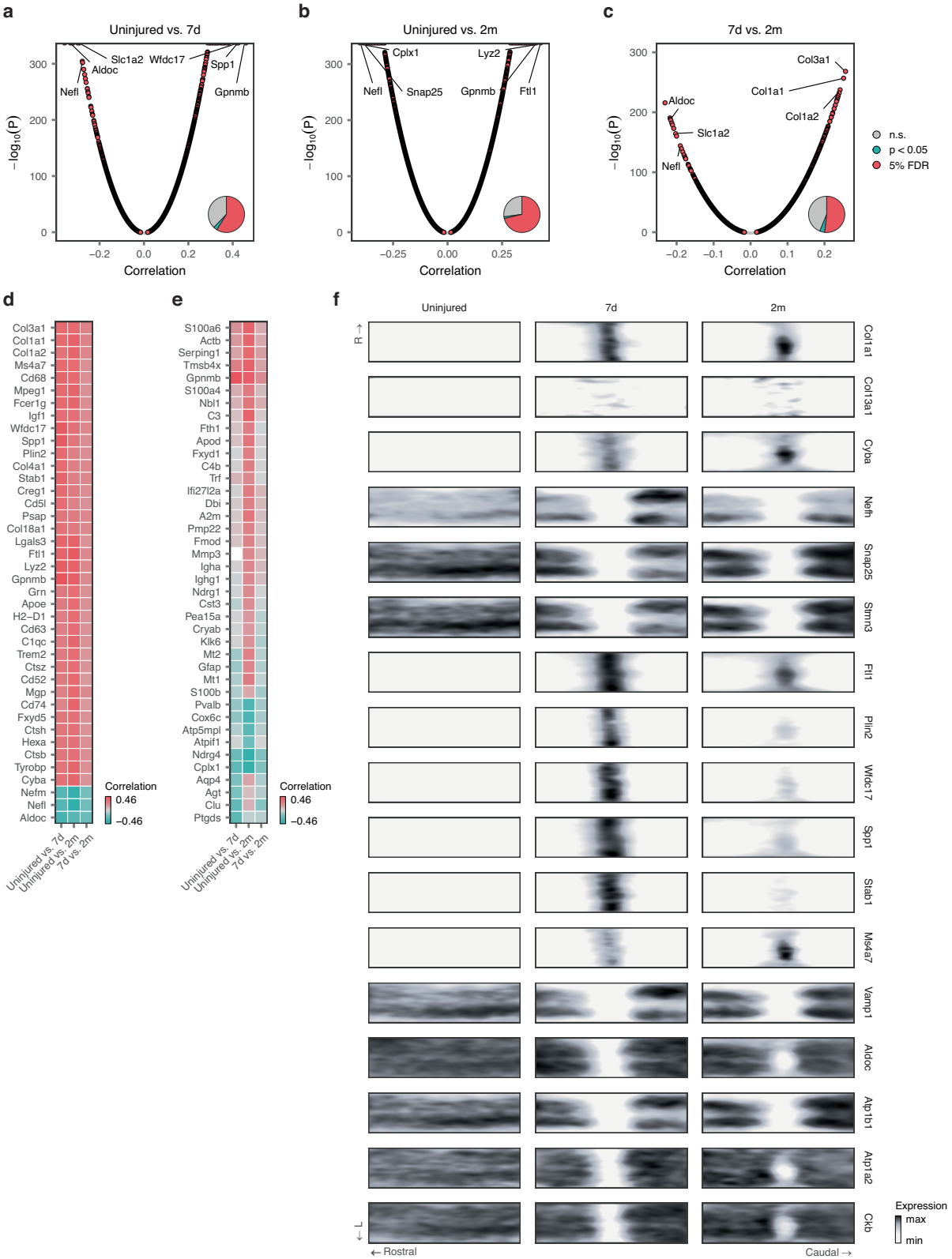

Extended Data Fig. 8 | Molecular basis of spatial prioritization at the gene level. a-c, Volcano plots showing correlations between the AUCs assigned by Magellan at each spatial barcode and transcriptome-wide gene expression across the same spatial barcodes (**a**, 7 days versus uninjured; **b**, 2 months versus uninjured; **c**, 7 days versus 2 months). Inset pie charts show the proportions of all tested genes that are significantly correlated with the spatial prioritizations. **d**, Heatmap showing Pearson correlations between spatial prioritizations and gene expression for each pairwise comparison of experimental conditions, for the top 40 most recurrently correlated genes across all comparisons. **e**, Heatmap showing Pearson correlations between spatial prioritizations and gene expression for each pairwise comparison of experimental conditions, for the top 40 most variably correlated genes across all comparisons. **f**, Visualization of selected genes prioritized by their correlation to spatial prioritizations on the two-dimensional coordinate system of the injured spinal cord.

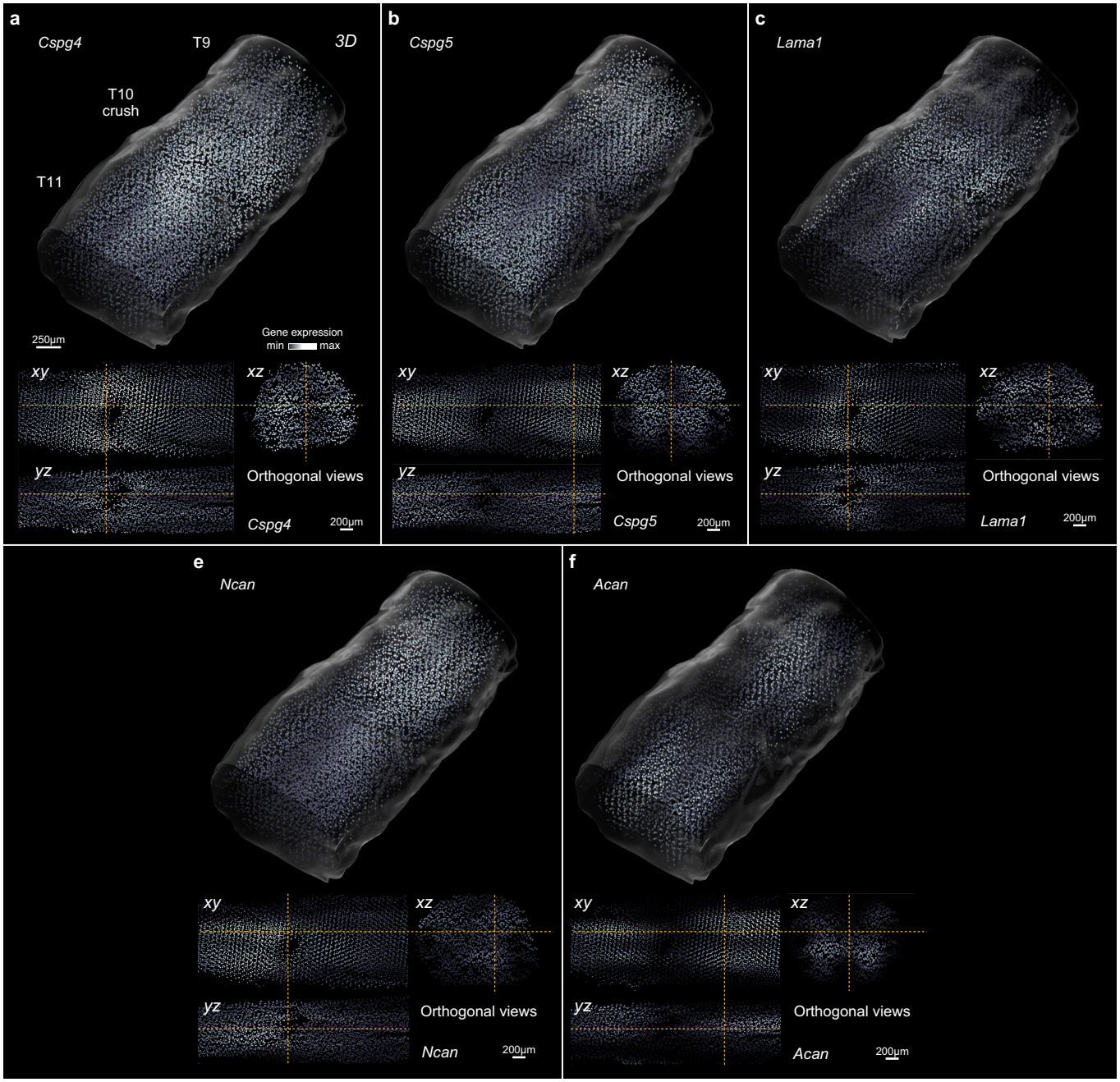

Extended Data Fig. 9 | Inhibitory and facilitating molecules in the 3D spatial atlas. Expression of selected inhibitory and facilitating molecules across the 3D spatial transcriptomic atlas at 7 days. **a**, Cspg4; **b**, Cspg5; **c**, Ncan; **d**, Acan; **e**, Lama1.

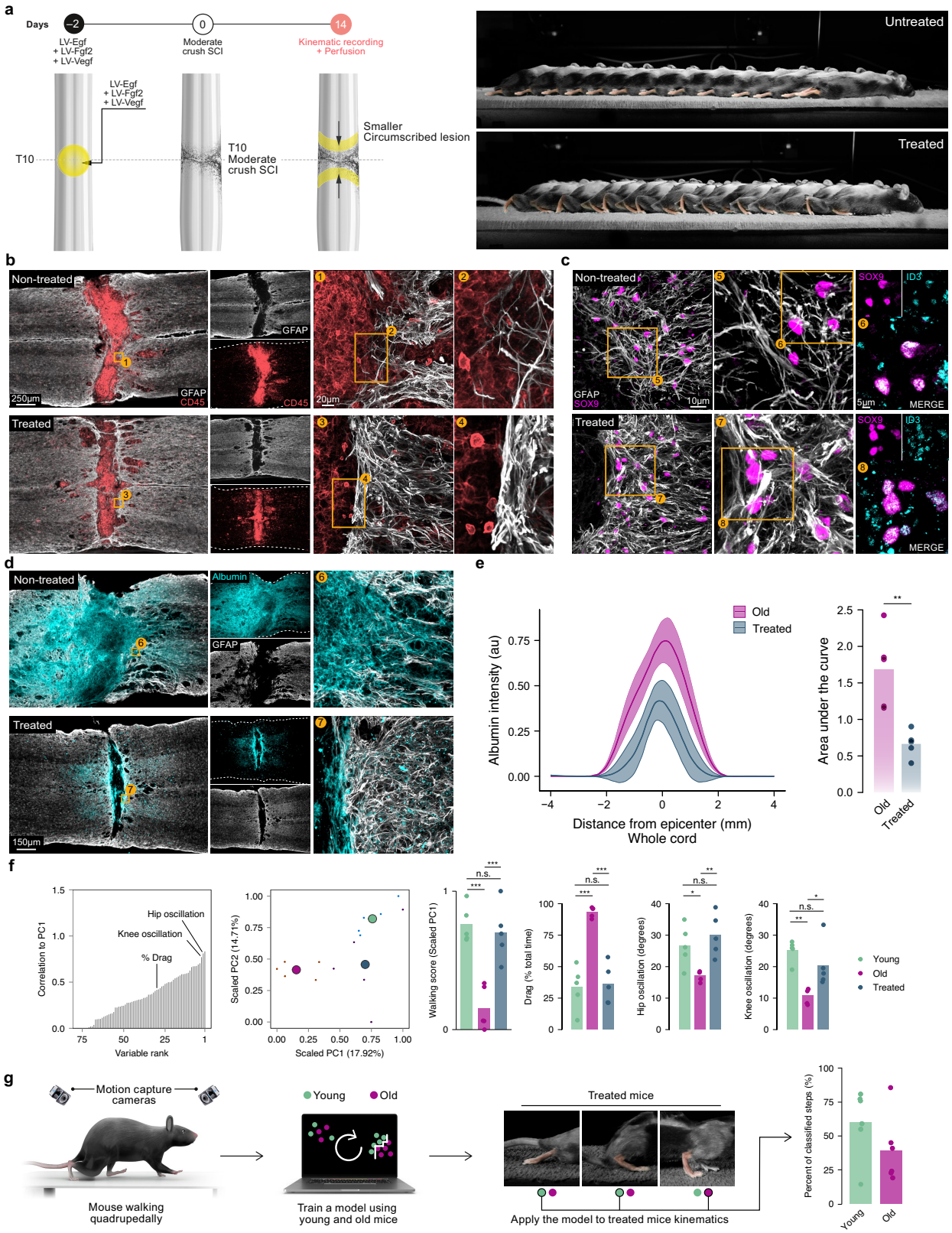

Extended Data Fig. 10 | See next page for caption.

Extended Data Fig. 10 | A rejuvenative gene therapy reestablishes the tripartite barrier to restore walking. a, Left, experimental design of a gene therapy intervention to promote the formation of the tripartite barrier, reproduced from Fig. 8a. Right, a second chronophotography series showing walking in old mice without (top) and with (bottom) a gene therapy intervention to promote the formation of the tripartite barrier. **b**, Composite tiled scans of GFAP and CD45 in horizontal sections from representative old and treated mice. **c**, Horizontal sections from representative old and treated mice identifying a restoration of $Sox9^{ON}Id3^{ON}$ cells in the astrocyte border region in treated mice. **d**, Composite tiled scans and confocal insets of albumin and GFAP in horizontal sections from representative old and treated mice after SCI. **e**, Line graph demonstrates albumin intensity at specific distances rostral and caudal to lesion centers. Bottom right, bar graph indicates the area under the curve (independent samples two-tailed t-test, $n = 5$ per group, $t = 4.07$, $p = 0.0099$). **f**, Locomotor performance in the gene therapy experiment, as quantified in Supplementary Fig. 3 ($n > 10$ gait cycles per mouse, ($n = 5$ mice per group; Tukey's honestly significant difference test). *, $p < 0.05$; **, $p < 0.01$; ***, $p < 0.001$. **g**, Left, schematic overview of the classification pipeline using high-resolution kinematics data from young and old mice. Right, experimental conditions assigned to individual steps in old mice that received gene therapy by a machine-learning model trained on kinematics data from untreated animals.

nature portfolio

Corresponding author(s): Gregoire Courtine, Jordan W Squair, Mark A Anderson

Last updated by author(s): Jan 29, 2024

Reporting Summary

Nature Portfolio wishes to improve the reproducibility of the work that we publish. This form provides structure for consistency and transparency in reporting. For further information on Nature Portfolio policies, see our Editorial Policies and the Editorial Policy Checklist.

Statistics

For all statistical analyses, confirm that the following items are present in the figure legend, table legend, main text, or Methods section.

n/a	Confirmed	
☐	☒	The exact sample size (*n*) for each experimental group/condition, given as a discrete number and unit of measurement
☐	☒	A statement on whether measurements were taken from distinct samples or whether the same sample was measured repeatedly
☐	☒	The statistical test(s) used AND whether they are one- or two-sided *Only common tests should be described solely by name; describe more complex techniques in the Methods section.*
☐	☒	A description of all covariates tested
☐	☒	A description of any assumptions or corrections, such as tests of normality and adjustment for multiple comparisons
☐	☒	A full description of the statistical parameters including central tendency (e.g. means) or other basic estimates (e.g. regression coefficient) AND variation (e.g. standard deviation) or associated estimates of uncertainty (e.g. confidence intervals)
☐	☒	For null hypothesis testing, the test statistic (e.g. *F*, *t*, *r*) with confidence intervals, effect sizes, degrees of freedom and *P* value noted *Give P values as exact values whenever suitable.*
☒	☐	For Bayesian analysis, information on the choice of priors and Markov chain Monte Carlo settings
☒	☐	For hierarchical and complex designs, identification of the appropriate level for tests and full reporting of outcomes
☐	☒	Estimates of effect sizes (e.g. Cohen's *d*, Pearson's *r*), indicating how they were calculated

Our web collection on statistics for biologists contains articles on many of the points above.

Software and code

Policy information about availability of computer code

Data collection	Data were collected using Vicon 5, Zen Black (Zeiss), Imaris (9.0.0, 64Bit, Bitplane).
Data analysis	Augur, Libra, and Magellan are available from GitHub (https://github.com/neurorestore/Augur, https://github.com/neurorestore/Libra, https://github.com/neurorestore/Magellan). Other software used for data analysis as follows: Imaris (version 9.0.0), DoubletFinder (version 2.0.3), scDblFinder (version 1.5.18), scds (version 0.99.4), and Scrublet (version 0.2.2), Seurat (version 4.0.3), clustree (version 0.4.4), Palo (version 1.1), tricycle (version 0.99.32), speckle (version 0.0.3), lmerTest (version 3.1-3), chromVAR (version 1.12.0), ArchR (version 1.0.2), imager (version 0.41.1), RCTD (version 2.0.0), DCGA (version 1.0-2).

For manuscripts utilizing custom algorithms or software that are central to the research but not yet described in published literature, software must be made available to editors and reviewers. We strongly encourage code deposition in a community repository (e.g. GitHub). See the Nature Portfolio guidelines for submitting code & software for further information.

Data

Policy information about availability of data

All manuscripts must include a data availability statement. This statement should provide the following information, where applicable:

- Accession codes, unique identifiers, or web links for publicly available datasets
- A description of any restrictions on data availability
- For clinical datasets or third party data, please ensure that the statement adheres to our policy

Source data are provided with this paper. Sequencing data have been deposited to the Gene Expression Omnibus (GSE234774, snRNA-seq and spatial transcriptomics, and GSE230765, multiome).

Research involving human participants, their data, or biological material

Policy information about studies with human participants or human data. See also policy information about sex, gender (identity/presentation), and sexual orientation and race, ethnicity and racism.

Reporting on sex and gender	N/A
Reporting on race, ethnicity, or other socially relevant groupings	N/A
Population characteristics	N/A
Recruitment	N/A
Ethics oversight	N/A

Note that full information on the approval of the study protocol must also be provided in the manuscript.

Field-specific reporting

Please select the one below that is the best fit for your research. If you are not sure, read the appropriate sections before making your selection.

☒ Life sciences ☐ Behavioural & social sciences ☐ Ecological, evolutionary & environmental sciences

For a reference copy of the document with all sections, see nature.com/documents/nr-reporting-summary-flat.pdf

Life sciences study design

All studies must disclose on these points even when the disclosure is negative.

Sample size	Sample sizes are estimated based on previous physiological studies using similar animal models (Anderson et al., 2016, 2018).
Data exclusions	In mice, expression of viral vectors were confirmed post-mortem. If there was a lack of expression, the animal was excluded from behavioural analysis. Single-cell RNA sequencing libraries that did not meet quality control criteria were excluded.
Replication	All tested conditions were repeated across multiple trials and the results averaged to obtain a single-subject mean performance.
Randomization	Animals were randomly assigned to experimental groups when more than one condition was present. For within-animal comparisons every effort was made to randomize the order of conditions.
Blinding	In some cases blinding is not possible during data collection as the animals either have a SCI or do not. Animals with SCI or SCI+experimental treatment were evaluated in a blinded fashion. All statistical analysis was completed with the investigator blind to the experimental codings.

Reporting for specific materials, systems and methods

We require information from authors about some types of materials, experimental systems and methods used in many studies. Here, indicate whether each material, system or method listed is relevant to your study. If you are not sure if a list item applies to your research, read the appropriate section before selecting a response.

Materials & experimental systems

n/a	Involved in the study
☐	☒ Antibodies
☒	☐ Eukaryotic cell lines
☒	☐ Palaeontology and archaeology
☐	☒ Animals and other organisms
☒	☐ Clinical data
☒	☐ Dual use research of concern
☒	☐ Plants

Methods

n/a	Involved in the study
☒	☐ ChIP-seq
☒	☐ Flow cytometry
☒	☐ MRI-based neuroimaging

Antibodies

Antibodies used

Primary antibodies were: rabbit anti-GFAP (1:1000; Dako); mouse anti-GFAP (1:1000; Cell Signalling Technology), rat anti-GFAP (1:1000; ThermoFisher Scientific); rabbit anti-albumin (1:250; abcam); rabbit anti-Chat (1:200; Millipore); guinea pig anti-NeuN (1:300; Millipore); chicken anti-RFP (1:500, Novus Biologicals); rabbit anti-Chx10 (also known as Vsx2) (1:500, Novus Biologicals); rat anti-CD45 (1:100, BD Biosciences); goat anti-Sox9 (1:200, Novus Biologicals); rabbit anti-Id3 (1:500; Cell Signalling Technology); rabbit anti-PKD1L2 (1:1000; Merck Millipore). Fluorescent secondary antibodies were conjugated to Alexa 488 (green), or Alexa 405 (blue), or Alexa 555 (red), or Alexa 647 (far red) (ThermoFisher Scientific, USA). The nuclear stain was 4',6'-diamidino-2-phenylindole dihydrochloride (DAPI; 2ng/mL; Molecular Probes).

Validation

All antibodies were validated by Western blot analysis performed by the commercial source.

Animals and other research organisms

Policy information about studies involving animals; ARRIVE guidelines recommended for reporting animal research, and Sex and Gender in Research

Laboratory animals

Adult male or female C57BL/6 mice (15-25 g body weight, 8-15 weeks of age) or transgenic mice were used for all experiments. Aged mice were purchased from JAX at 60 weeks of age (stock no. 000664). Vsx2Cre (MMMRRC 36672, also called Chx10Cre) transgenic mouse strain was bred and maintained on a mixed genetic background (C57BL/6).

Wild animals

No wild animals were used in the study

Reporting on sex

Both male and female mice were used in these experiments.

Field-collected samples

No field-collected samples were used in the study

Ethics oversight

All procedures and surgeries were approved by the Veterinary Office of the Canton of Geneva (Switzerland; authorization GE/145/20).

Note that full information on the approval of the study protocol must also be provided in the manuscript.